



January 2019

Thermomechanical Processing Of Mg-Li-Al Ultralight Alloys

Rezawana Islam

Follow this and additional works at: <https://commons.und.edu/theses>

Recommended Citation

Islam, Rezawana, "Thermomechanical Processing Of Mg-Li-Al Ultralight Alloys" (2019). *Theses and Dissertations*. 2462.
<https://commons.und.edu/theses/2462>

This Thesis is brought to you for free and open access by the Theses, Dissertations, and Senior Projects at UND Scholarly Commons. It has been accepted for inclusion in Theses and Dissertations by an authorized administrator of UND Scholarly Commons. For more information, please contact zeineb.yousif@library.und.edu.

**THERMOMECHANICAL PROCESSING OF Mg-Li-Al ULTRALIGHT
ALLOYS**

by

Rezawana Islam

Bachelor of Science, Military Institute of Science and Technology

A Thesis
Submitted to the Graduate Facility

of the

University of North Dakota

in partial fulfillment of the requirements

for the degree of

Master of Science

Grand Forks, North Dakota

May 2019

Copyright 2019 Rezawana Islam

This thesis, submitted by Rezawana Islam in partial fulfillment of the requirements for the Degree of Master of Mechanical Engineering from the University of North Dakota, has been read by the Faculty Advisory Committee under whom the work has been done and is hereby approved.

M. Haghshenas
Dr. Meysam Haghshenas

Anjali Sandip
Dr. Anjali Sandip

Ali N. Alshami
Dr. Ali Alshami

This thesis (or dissertation) is being submitted by the appointed advisory committee as having met all of the requirements of the School of Graduate Studies at the University of North Dakota and is hereby approved.



Dr. Chris Nelson, Associate Dean

Dean of the School of Graduate Studies

4/26/19

Date:

PERMISSION

Title Thermomechanical processing of Mg-Li-Al ultralight alloys.

Department Mechanical Engineering

Degree Master of Science

In presenting this thesis in partial fulfillment of the requirements for a graduate degree from the University of North Dakota, I agree that the library of this University shall make it freely available for inspection. I further agree that permission for extensive copying for scholarly purposes may be granted by the professor who supervised my thesis work or, in her (or his) absence, by the Chairperson of the department or the Dean of the School of Graduate Studies. It is understood that any copying or publication or other use of this thesis or part thereof for financial gain shall not be allowed without my written permission. It is also understood that due recognition shall be given to me and to the University of North Dakota in any scholarly use which may be made of any material in my thesis.

Rezawana Islam

4/25/2019

TABLE OF CONTENTS

ABSTRACT	xiii
CHAPTER I.....	1
1. INTRODUCTION.....	1
1.1. Background Information and Motivation.....	1
1.2. Problem Statement and Scope of Thesis	2
1.3. Thesis Organization	3
CHAPTER II.....	5
2. LITERATURE REVIEW.....	5
2.1. Thermomechanical Processing.....	5
2.1.1. Cold working	8
2.1.2. Dynamic Recovery	9
2.1.3. Dynamic Recrystallization (RDX).....	10
2.1.4. Grain Growth.....	12
2.2. Mg-Li-Al	13
2.2.1. Mg	13
2.2.2. Cast magnesium alloys	16
2.2.3 Wrought magnesium alloys	19
2.2.4 Mg-Li	20
2.2.5 Effect of Li on Mg.....	21
2.2.6 Microstructure & crystal Structure	24
2.3 Nanoindentation	27
2.4 Thermomechanical processing (TMP) of Mg-Li alloys	31
2.4.1 Effect of temperature	34
2.4.2 Effect of strain rate.....	35
2.5 Microstructure (effect of TMP on microstructure).....	36
2.5.1 Dynamic recovery (DRV)	36

2.5.2 Dynamic recrystallization (DRX)	37
2.5.3 Grain growth.....	38
2.6 Application.....	39
2.6.1 Applications of Mg and its alloys	39
2.7 Objective.....	47
CHAPTER III	50
3. EXPERIMENTAL TECHNIQUES	50
3.1. Sample preparation	50
3.2. Thermomechanical Processing.....	51
3.3. Nanoindentation	54
3.4. Microstructural Assessment.....	58
3.4.1. Optical Microscope	58
3.4.2. Scanning Electron Microscopy (SEM).....	59
3.4.3. XRD (X-ray Diffractometer)	60
CHAPTER IV	61
4. RESULTS AND DISCUSSION	61
4.1. Mg-3.5Li-1Al Alloy	61
4.1.1. Effect of temperature on flow graphs.....	61
4.1.2. Effect of strain rate on Flow Graphs.....	64
4.1.3. Microstructure	67
4.1.4. Indentation load/displacement.....	73
4.1.5. Constitutive equation of Mg-3.5Li-Al alloy from flow stress-strain behavior.....	80
4.1.6. Constitutive analyzing using the Zener-Hollomon model	84
4.2. Mg-14Li-1Al alloy	88
4.2.1. Effect of temperature on flow graphs.....	88
4.2.2. Effect of strain rate Flow Graphs	91
4.2.3. Microstructure	93

4.2.3.1. As received alloy	93
4.2.3.2. Effect of temperature on microstructure.....	97
4.2.3.4. Effect of strain rate on microstructure.....	99
4.2.3.5. SEM.....	101
4.2.4. XRD.....	105
4.2.5. Nanoindentation	106
4.2.6. Constitutive equation of the Mg-14Li-Al alloy	111
4.2.7. Constitutive analyzing using the Zener-Hollomon model.....	113
4.3. Comparison between Mg-3.5Li-Al & Mg-14Li-Al alloy	117
4.3.1. Mechanical Properties.....	117
4.3.2. TMP results comparison.....	118
4.3.3. Microstructures.....	120
4.3.4. Nanoindentation results	121
CHAPTER V	126
5. Conclusion and Future Work.....	126
5.1. Conclusions.....	127
5.1.1. Mg-3.5Li-Al alloy	127
5.1.2. Mg-14Li-Al alloy	127
5.1.3. Comparison of Mg-3.5Li-Al and Mg-14Li-Al alloy	128
5.2. Future Work	128
References	130

LIST OF FIGURES

Figure 2-1. The TMP cycle.	6
Figure 2-2. Bulk Material Processing.....	7
Figure 2-3. Stress-Strain Graph.	8
Figure 2-4. Change in the flow curved induced by cold working.	9
Figure 2-5. Dynamic Recovery [7].	10
Figure 2-6. Dynamic Recrystallization [7].	11
Figure 2-7. Schematic diagram of the main annealing processes; (a) deformed state, (b) Recovered, (c) Partially recrystallized, (d) fully recrystallized, (e) Grain growth and (f) abnormal grain growth [5].....	12
Figure 2-8. Comparison of Mg properties with other structural materials.	14
Figure 2-9. Cold chamber die casting method.	17
Figure 2-10. Phase Diagram of Mg-Li alloys [19].	21
Figure 2-11. Effect of Li on Mg. a) Lattice Parameters; b) axial ratio [20].....	23
Figure 2-12. Common metallic crystal structure a) BCC structure, b) HCP structure.....	24
Figure 2-13. Typical microstructure of Mg-Li-Al alloy [23].....	25
Figure 2-14. Illustration of the major differences between deformation and damage features and microstructures in AZ31 alloy [23].....	26
Figure 2-15. a) Nanoindentation b) Load-depth graph [24].	28
Figure 2-16. Load-displacement curve recorded during instrumented indentation [25].....	28
Figure 2-17. Schematics of Berkovich indenter [28].....	30
Figure 2-18. Indentation mark over the sample surface [25].	30
Figure 2-19. Stress-strain graph [30].....	32
Figure 2-20. Illustration of material property and grain size variation during cold working (left) and subsequent annealing (right) of a metallic material [31].....	33
Figure 2-21. Effect of temperature [32].....	34
Figure 2-22. Effect of strain rate [33].....	35
Figure 2-23. a) Dynamic recovery by annealing, b) annealing by edge dislocation [35].....	37
Figure 2-24. Effect of temperature on metal forming process [8].	38

Figure 2-25. Highlights one successful application of magnesium in producing center console cover in Porsche Carrera GT [16].....	40
Figure 2-26. Magnesium sheet panels formed recently by General Motors. (a) Door inner panel; (b) decklid inner panel; (c) hood [16].	42
Figure 2-27. Transportation Application [16].	44
Figure 2-28. Applications for magnesium alloys in the aircraft industry [40]	46
Figure 3-1. Samples a) before and b) after mounting.	51
Figure 3-2. Experimental set up for TMP.	52
Figure 3-3. a) Nanoindentation machine b) Indentation platform.	55
Figure 4-1. Flow curves showing dynamic recovery and recrystallization at a) 250°C, b) 350°C, c) 450°C.....	64
Figure 4-2. True stress-strain curves for Mg-3.5Li-Al alloy during compression at a) 0.001 s-1, b) 0.01 s-1, c) 0.1s-1, d) 1 s-1.....	67
Figure 4-3. Initial microstructure of the Mg-3.5Li-1Al alloy.....	68
Figure 4-4. Microstructures of the thermomechanically processed Mg-3.5wt%Li-Al alloy at different temperatures 250°C, 350°C, and 450°C and strain rates of 1, 0.1, 0.01, and 0.001 /s.....	69
Figure 4-5. a) 250 °C 0.001/s evidence of twins at this deformation stage, b) 350 °C 0.1/s chains of recrystallized grains, necklace like structure, c) 450 °C 0.01/s recrystallized structure, d) 450 °C 1/s recrystallized structure.	73
Figure 4-6. Nanoindentation results for as received alloy.	74
Figure 4-7. Nanoindentation results for samples deformed at the constant strain rate of 1/s.	76
Figure 4-8. Schematic of dynamic strain aging (DSA) causing PLC effect [12].	77
Figure 4-9. SEM microstructure of Mg-3.5Li-Al alloy (deformation temperature 350 °C and strain rate of 0.1/s) the precipitates.	78
Figure 4-10. Peak stress for different strain rates.	81
Figure 4-11. $\ln\dot{\epsilon}$ - σ relation curve, symbols show the experimental data and solid lines represent best linear fit.....	83
Figure 4-12. $\ln\dot{\epsilon}$ - $\ln\sigma$ relation curve, symbols show the experimental data and solid lines represent best linear fit.....	83
Figure 4-13. $\ln\dot{\epsilon}$ - $\ln[\sinh(\alpha\sigma)]$ relation curve, symbols show the experimental data and solid lines represent best linear fit.	85

Figure 4-14. $\ln\epsilon' - \ln[\sinh(\alpha\sigma)]$ relation curve symbols show the experimental data and solid lines represent best linear fit.....	86
Figure 4-15. Comparison between the measured and the calculated stress-strain graph for 450 °C and 1/s.....	87
Figure 4-16. Comparison between the measured peak stress and the calculated peak stresses based on hyperbolic sine function.....	88
Figure 4-17. Flow curves of the Mg-14Li-1Al alloy at a) 250°C, b) 350 °C, c) 450°C.....	90
Figure 4-18. Flow graphs at different strain rates a) 1/s, b) 0.1/s, c) 0.01/s, and d) 0.001/s.....	93
Figure 4-19. Image of microstructure for as-received alloy.....	94
Figure 4-20. Microstructures of the thermomechanically processed Mg-14wt%Li-Al alloy at different temperatures 250°C, 350°C, and 450°C and strain rates of 1, 0.1, 0.01, and 0.001 /s.....	96
Figure 4-21. Microstructure at 0.01/s a) 250 °C, b) 350 °C, c) 450 °C.....	98
Figure 4-22. Microstructures at 450 °C and different strain rates a) 0.001/s b) 0.01/s c) 0.1/s c) 1/s.....	101
Figure 4-23. SEM images for deformed samples at 0.01/s strain rate and deformation temperature of a) 250 °C, b) 350 °C, c) 450 °C.....	103
Figure 4-24. Micro-area chemical composition graph from SEM-EDS.....	104
Figure 4-25. SEM-EDS for alloy composition at surface point.....	105
Figure 4-26. XRD pattern of Mg-Li-Al alloy a) 250 °C, 1/s b) 450 °C, 0.001/s.....	106
Figure 4-27. Nanoindentation results of the as-received alloy.....	107
Figure 4-28. Nanoindentation results of the TMPed alloy.....	108
Figure 4-29. Peak stress curves of the studied Mg-14Li-Al alloy.....	111
Figure 4-30. Flow graph comparison.....	119
Figure 4-31. Microstructural changes upon TMP.....	120
Figure 4-32. Nanoindentation results comparison a) the Mg-3.5Li-Al alloy, b) the Mg-14Li-Al alloy.....	123

LIST OF TABLES

Table 2-1. Comparison of density of Mg with other structural materials.....	13
Table 2-2 Physical properties of pure magnesium [9].	14
Table 2-3. The effect of alloying elements on Magnesium [10, 11].	15
Table 2-4. Design parameters and manufacturing characteristics for magnesium die casting[13].	18
Table 2-5. Potential automotive application of wrought magnesium alloys.....	41
Table 2-6. Aerospace application of Mg alloys [12].....	45
Table 3-1. Initial dimensions for Mg-3.5Li-Al.	53
Table 3-2. Initial dimensions for Mg-14Li-Al.	53
Table 3-3. Dimensions after TMP for Mg-14Li-Al.	54
Table 4-1. Hardness and elastic modulus of Mg-3.5Li-Al alloy (for 1/s strain rate).....	75
Table 4-2. Micro-area chemical composition analysis result of alloy from Fig. 4-24.....	104
Table 4-3. Hardness and elastic modulus result.....	110
Table 4-4. Characteristics differences of the alloys.....	118
Table 4-5. Hardness & elastic modulus properties comparison.....	121

ACKNOWLEDGEMENT

I wish to express my sincere gratitude to:

Dr. Meysam Haghshenas, my Advisor, for his enormous support, continual encouragement and valuable advice throughout my master's research work.

The members of my advisory committee, Dr. Anjali Sandip and Dr. Ali Alshami for their valuable time, and support towards accomplishing this thesis at the University of North Dakota.

ND EPSCoR and the Department of Mechanical Engineering at UND for providing me financial support during my entire degree period.

Besides, I thank all the members of the Lab for helping me in every way possible. I also thank the Advanced Material Characterization Laboratory for all experimental research works.

Finally, I thank all of my family members and friends for their endless love, faith and support for me. All my achievements become possible because of them.

ABSTRACT

Globally, magnesium (Mg), as the lightest metallic material, imparts a significant long term impact on the stipulation of lightweight structures in aerospace and automotive industries. However, the deformation behavior of magnesium at ambient (room) temperature is not acceptable for most of the structural applications because of its hexagonal closed pack (hcp) structure and limited active slip systems which result in an unacceptable level of brittleness (literally no formability at ambient temperature). Having said this, alloying Mg with an element with more active slip system in its crystalline structure (i.e. lithium with body center cubic crystalline structure) might be a solution to improve strength and ductility of the Mg. Addition of the lithium (Li) as the lightest element (density 0.54 g/cm³) in Mg (density ~1.74 g/cm³) results in enhanced plasticity producing ultra-light metallic alloys of Mg-Li with density of 1.35-1.65 g/cm³. The Mg-Li alloys are considered as the lightest metallic alloys which make them unique for many weight-saving applications.

Aluminum reinforcement in Mg-Li matrix develops the strength and corrosion resistance without introducing any second phase in the alloy. Because of its high solubility in Mg, aluminum can improve the strength without deterioration of density of Mg-Li alloy by means of grain size refining, solid solution hardening, and compound reinforcements. Although the alloy (Mg-Li-Al) possesses acceptable elastic modulus to density ratio, specific strength, damping capabilities, and electromagnetic shielding capability, extensive applications of Mg-Li alloys are still limited due to relatively low strength, poor corrosion resistance, and limited thermal stability.

In the present project a single phase Mg-3.5Li-Al (wt%) and a dual phase Mg-14Li-Al (wt%) are first thermomechanically processed through hot compression tests. Then microstructure, post thermomechanical properties, and hot compression stress-strain curves are studied. The main objective is to correlate the microstructure with the small scale properties and processing parameters (i.e. thermomechanical parameters like temperature and strain rate). The thermomechanical cycle consists of uniaxial compression at temperatures of 250°C, 350°C, and 450°C and strain rates of 1, 0.1, 0.01, and 0.001 /s using a Gleebel® 3500 thermal-mechanical simulation testing system. True stress-true

strain curves plotted from the thermomechanical tests were used to assess the working behavior of the materials, to analyze and to understand the microstructure evolution which reflect intrinsic mechanical properties. Microstructural changes, hot compression stress-strain curves, and nanoindentation load/displacement response, to study post processing mechanical properties, for both alloys were discussed in detail in the present research.

CHAPTER I

1. INTRODUCTION

1.1. Background Information and Motivation

Due to the crucial fact associated with increasing amount of greenhouse gas emissions, minimize the carbon dioxide emissions and reducing fuel consumption rate in the automotive and aerospace industries are turning into considerably essential subjects of discussion for numerous countries. Several enterprises, including the automotive and aerospace, are evaluating approaches to lessen the general weight of their vehicles. There has been a change from ferrous materials and high strength steels to lower density materials like magnesium. Given low density, and magnificent mechanical strength of magnesium alloys, these materials give excellent reactions to supplant steel in both aerospace and automotive vehicles to diminish the general weight. This decrease in weight prompts lower fuel utilization and thus bringing down the effect of the carbon dioxide discharges on the environment.

As magnesium is spreading out into more crucial automotive structural applications, there is a huge demand for developing magnesium alloy products to provide better mechanical and physical properties, corrosion resistance and crash performance. Most crucial fact is the improvement of the plasticity of wrought magnesium, which turns into drastically decreased at room temperature. Because of the limitations that pure

magnesium possess makes this vulnerable to bring this light weight material in applications.

The challenges with the application of magnesium especially at room temperature are: its hexagonal close-packed (hcp) structure, a limited amount of slip systems and limited ductility [1]. Due to the poor ductility and formability of magnesium at room temperature Mg alloy applications have been considerably hampered. Recent alloy development activities in Mg have commenced due to the interest in using lightweight magnesium in automotive and aerospace applications. Mg-Li-Al are one of the most widely used alloys for sheet and plate products [1]. Alloys with very low density and good formability have been developed by adding lithium to magnesium. This alloy responds excellently to high formability, and can potentially be formed at room temperature [1]. However, there are a number of unanswered questions on the ambient and non-ambient plastic deformation of ultralight Mg-Li-Al alloys and this thesis tries to shed some light on the thermomechanical processing (TMP) of the alloy.

1.2. Problem Statement and Scope of Thesis

Final performance occurs at ambient temperatures, the plasticity of magnesium at these temperatures remains paramount to their performance in structural applications. Most critical is the improvement of the plasticity of magnesium alloy, which becomes dramatically developed as lithium has been added in the Mg body in Mg-Li alloy. Afterwards, various manufacturing processes like the TMP can be used to change the

properties of the Mg-Li alloy. To assess post-TMP properties, a non-destructive depth sensing nanoindentation testing method has been employed. Precise understanding of the properties and configurations will help improve the application of the alloy in different fields of the vehicle components, aviation, electronic, and sport industries.

This project focuses on the TMP of two specific Mg-Li alloys, wrought magnesium alloy Mg-3.4Li-Al and Mg-14Li-Al. The main purpose is to compare the hot workability and the microstructure of these two alloys and their post TMP mechanical properties optical and scanning electron microscope images, X-ray diffraction and results from nanoindentation tests.

1.3. Thesis Organization

The thesis has been divided into five chapters which are as follows: The first chapter delivers a brief overview to the issue and states the motivation and objectives of the work. Chapter two familiarizes thermomechanical processing, magnesium, magnesium lithium alloys and their physical and mechanical properties. It further deliberates the conventional concepts and studies regarding the effect of TMP processing parameters (e.g., temperature and strain rate) on the microstructural mechanical properties. Chapter two also, describes the background of Nanoindentation testing which was used in understanding post TMP mechanical properties for the alloys. Chapter three yields the numerous experimental procedures used in this study. Chapter four explains the experimentally observed results and correlation established between the processing

parameters and mechanical properties through the characterization of wrought Mg-3.5Li-Al and Mg-14Li-Al alloy. The experimental results were determined via hot compression and nanoindentation testing. The relationship between microstructures and mechanical properties for each alloy observed are described. Finally, Chapter five delivers assumptions of the research results and recommendations to further utilize the findings from this work.

CHAPTER II

2. LITERATURE REVIEW

2.1. Thermomechanical Processing

Most commercial metal products in the industry, their properties and external shape are the result of hot- deformation, such as forging, rolling methods. Whereas the required mechanical properties achieved from the alloy configuration and by hot deformation. Development or change in mechanical properties as direct consequences of the alloying elements are often perceived as a result of heat treatment.

In Thermo-mechanical processing (TMP), all shaping, and heating activities connected to the beginning material prompts semi-or last items described by new, better properties (as for the underlying material). Microstructure and texture evolutions are key of significance for anticipated changes [2].

The 'mechanical' part of thermo-mechanical processing (TMP) essentially implies the mechanics of plastic deformation, whereas 'thermo-' to the impact of the heat treatment.

Fig. 2-1 shows that through the process the material undergoes as result of thermomechanical properties reflects on the microstructure as change of properties. Therefore, microstructure is the result of process, properties and materials amid heat treatment.

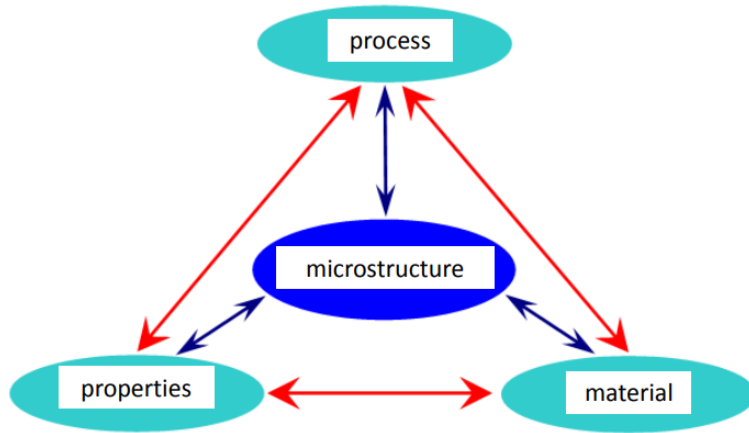


Figure 2-1. The TMP cycle.

Basically, TMP is a metallurgical procedure that consolidates mechanical or plastic deformation process like compression or forging, rolling etc. Moving and so on with thermal procedures like heat-treatment, water quenching, heating and cooling at different rates into a solitary procedure.

The capacity of a metal to plastically deform relies upon the capacity of dislocation to move. Limiting or blocking dislocation motion renders a material harder and stronger. Moderately high stress required to start plastic deformation at room temperature, ability to work harden amid plastic straining which offers ascend to their steadiness or limit to oppose failure. Most importantly, whenever heated, plastic flow turns out to be moderately simple, therefore the material can be formed into segments or semi-completed items including vast strains. Fig. 2-2 highlights some techniques for bulk manufacturing at elevated temperature. Some common type of bulk metal forming processes is Rolling, Forging, Extrusion and Drawing.

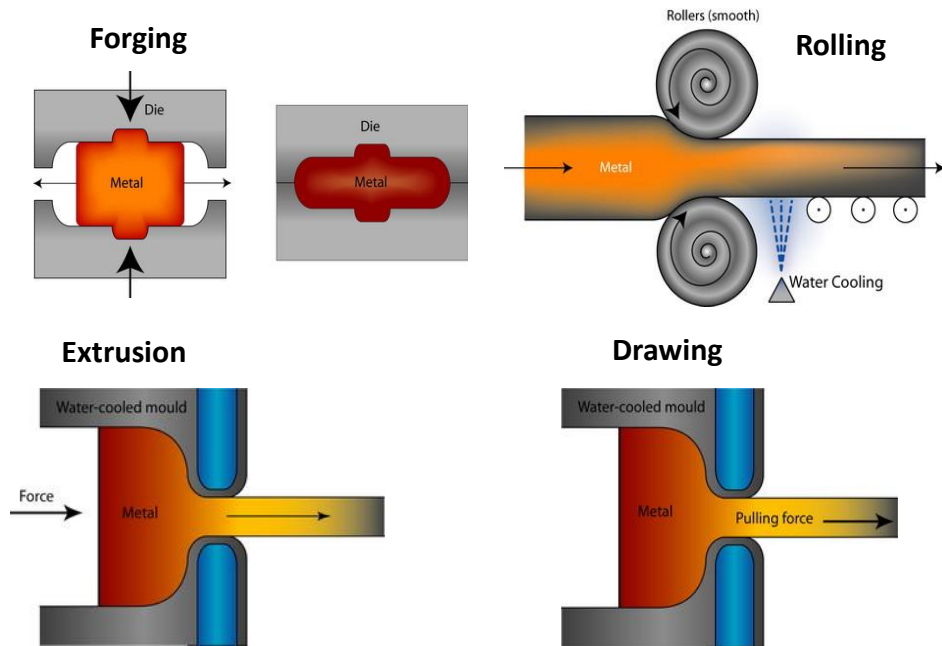


Figure 2-2. Bulk Material Processing.

Hot deformation turns out to be a significant part of heat treatment and consequential metallurgical differences from the initial material occurred by hot deformation yields newer effects on the properties of the material following cooling or final heat treatment [3].

Numerous superior metallic alloys rely upon thermo-mechanical preparing to display the level of properties that make them appealing. As it is a process to improve the mechanical properties of the desired material by determining the behavior of hot deformation process, whilst often fabricating new and better characteristics material.

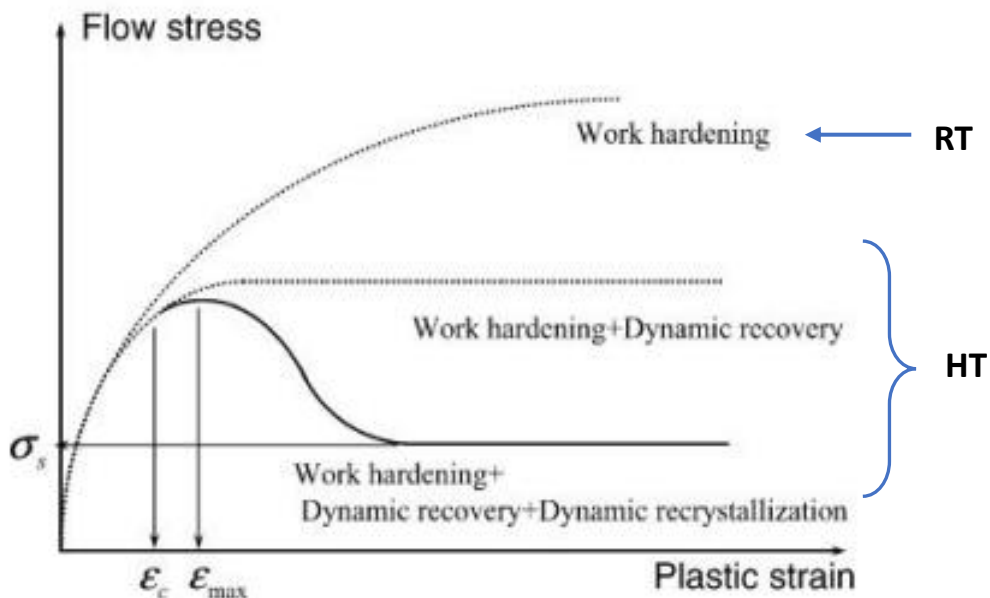


Figure 2-3. Stress-Strain Graph.

Microstructural changes after TMP results from two different processes which happened at elevated temperatures and these are Dynamic recover and Dynamic Recrystallization, which may be followed by grain growth [4]. This includes no Work Hardening (Fig. 2-3).

2.1.1. Cold working

Cold working means the process of strengthening a metal by changing its shape without the use of heat. Figure. 2-4 illustrates very clearly that when percentage of cold work gets increased hardness increases but ductility decreases.

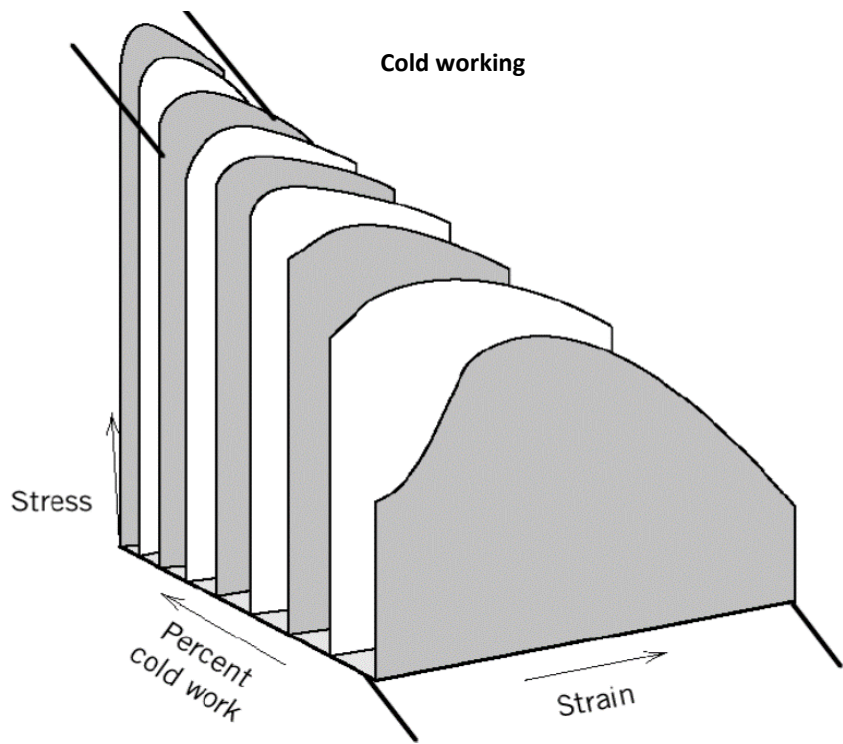


Figure 2-4. Change in the flow curved induced by cold working.

2.1.2. Dynamic Recovery

Recovery is a procedure by which deformed grains can decrease their stored energy by the evacuation or modification of defects in their crystal structure. These imperfections, principally dislocations, are presented by plastic deformation of the material and act to expand the yield strength of a material. Since recovery decreases the dislocation density the procedure is ordinarily accompanied by a decrease in a materials strength and a concurrent increment in the ductility. Thus, recovery might be viewed as gainful or negative contingent upon the conditions [5]. Recovery occurs first (at ~0.1TM) [6]. Thermal energy allows some dislocation motion.

The microstructural changes (Fig. 2-5) amid recovery are generally homogeneous and do not for the most part influence the boundaries between the deformed grains; these progressions in microstructure. Comparable recovery procedures may likewise happen amid deformation. Especially, at high temperatures, and this dynamic recovery acts an important role in the creep and hot working of materials.

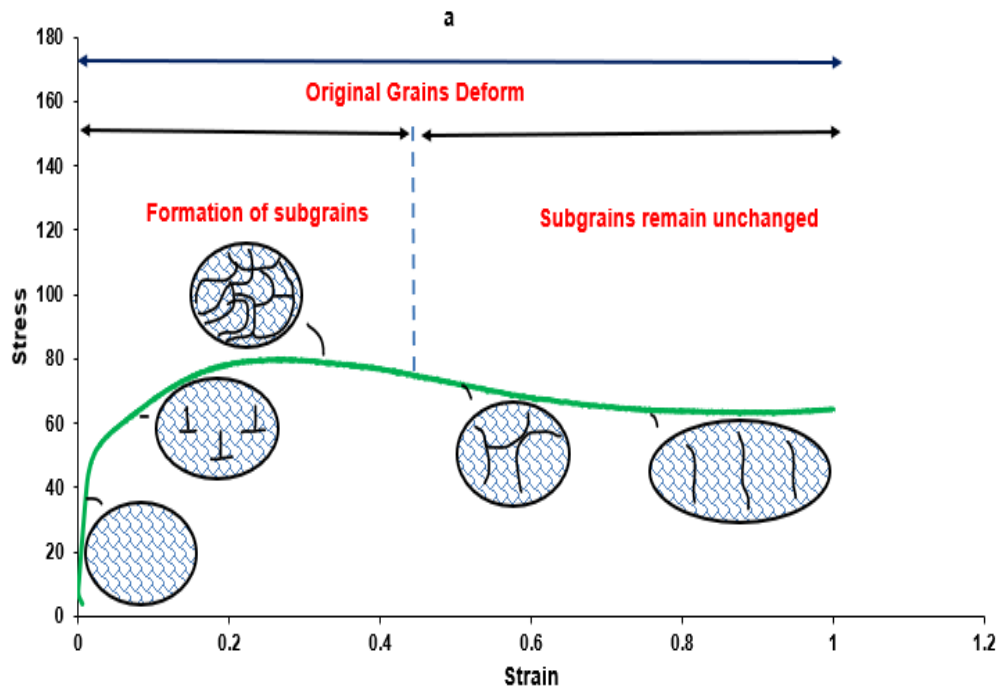


Figure 2-5. Dynamic Recovery [7].

2.1.3. Dynamic Recrystallization (RDX)

Fig. 2-6 shows the RDX step by step. At elevated temperature, new strain free grains nucleate and develop inside the old distorted grains and at the grain boundaries. New grains develop to supplant the deformed grains. RDX relies on temperature, additionally the measure of time at that temperature. The more noteworthy the strain

hardening, the more nuclei for the new grains, and the subsequent grain size will be smaller.

Major changes come from recrystallization that occurs at higher temperatures (at ~0.3–0.5TM). New grains nucleate and grow at the expense the highly-strained.

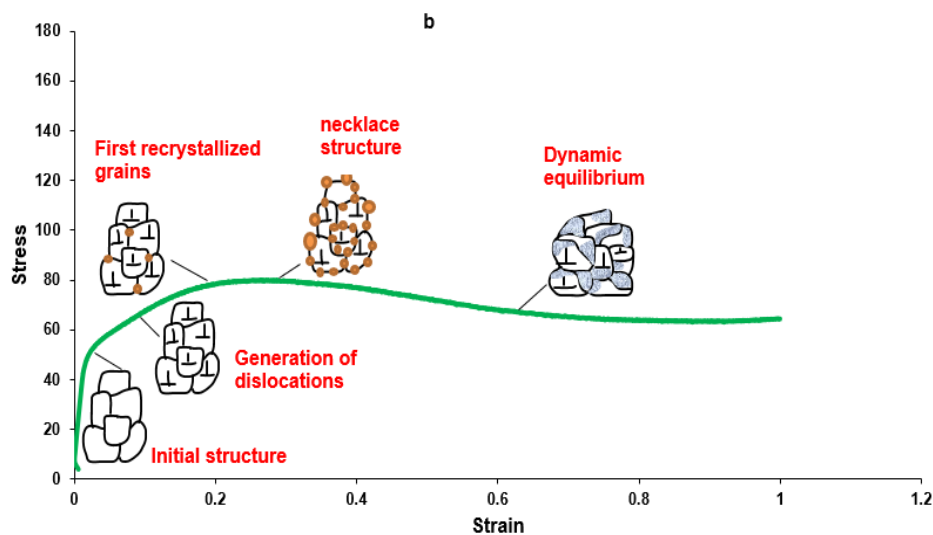


Figure 2-6. Dynamic Recrystallization [7].

Although recrystallization expels the dislocations, the material still contains grain boundaries, which are thermodynamically unstable. Further annealing may result in grain growth, in which the smaller grains are dispensed with, the larger grains grow, and the grain boundaries assume a lower energy configuration. In certain conditions this normal grain growth may offer path to the development of a few large grains, a procedure known as abnormal grain growth or secondary recrystallization [8].

2.1.4. Grain Growth

If the specimen is left at the high temperature beyond the time needed for complete recrystallization, the grain starts to develop in size. This happens since diffusion happens over the grain boundary and longer grains have less grain boundary surface area per unit of volume. Therefore, larger grains lose less atoms and develop at the expense of smaller grains (Fig. 2-7).

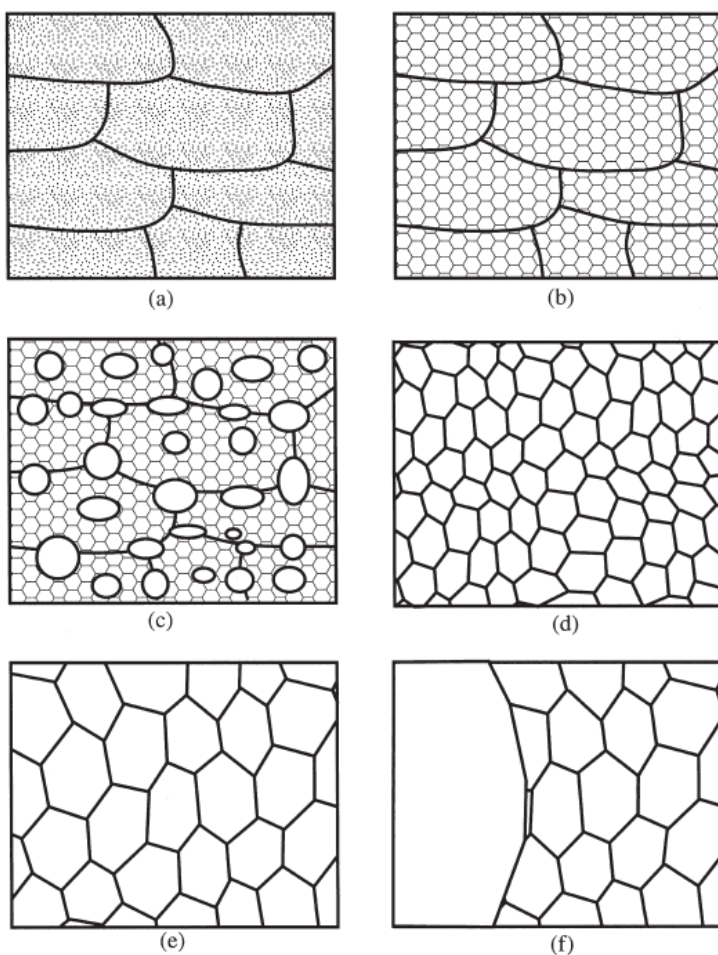


Figure 2-7. Schematic diagram of the main annealing processes; (a) deformed state, (b) Recovered, (c) Partially recrystallized, (d) fully recrystallized, (e) Grain growth and (f) abnormal grain growth [5].

2.2. Mg-Li-Al Alloy

2.2.1. Mg

Magnesium is the lightest metallic material. Magnesium has a strikingly low density of 1.75 g/cm³; in comparison to the density (Table 2-1) of other structural materials Al with 2.5 g/ cm³, Ti with 4.4 cm³ and stainless steel with 7.6 cm³. Currently, Mg is the third most widely used structural metal. But Mg-materials can be very promising replacements for Al, Ti and Steels. Around 70% and 30% weight can be saved if Mg alloy is used in place of steel and aluminum alloys [9]. The density of magnesium is almost like that of polymers. Magnesium and magnesium alloys, which are among the lightest structural metals, are ending up progressively important in the automotive and aerospace businesses [10].

Table 2-1. Comparison of density of Mg with other structural materials

Property	Mg alloys	Al Alloys	Ti alloys	Stainless steel
Density (g/cm ³)	1.75-1.87	2.5-2.9 (33%)	4.4-4.8 (61%)	7.6-8.1 (77%)

From Fig. 2-8 we can observe that it is very reasonable to prefer Mg over other structural materials because, first being light in weight, having low melting point, at the same time for being stiff and strong.

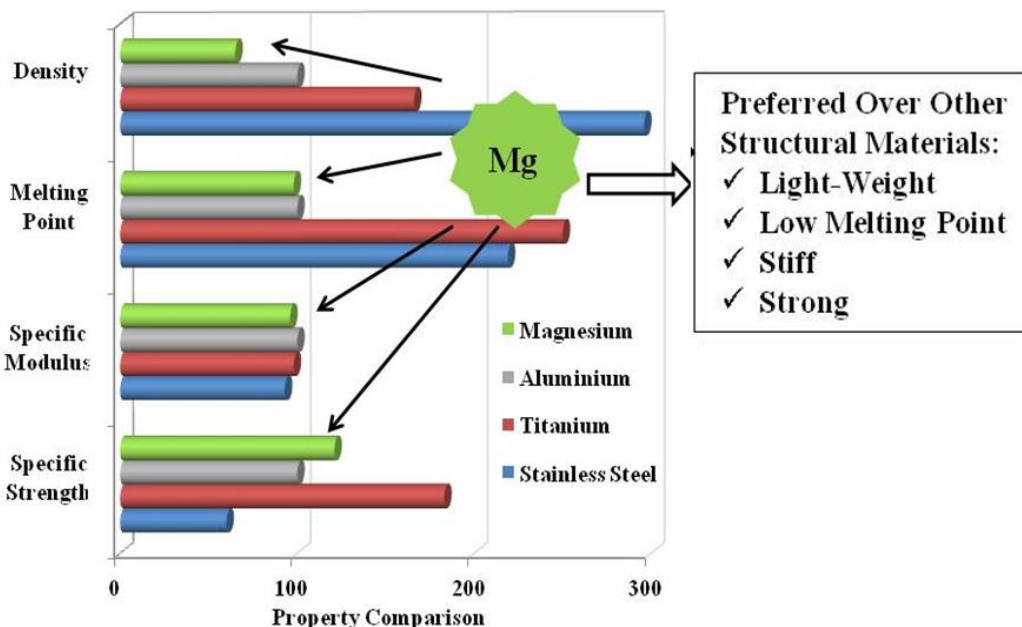


Figure 2-8. Comparison of Mg properties with other structural materials.

Table 2-2 Physical properties of pure magnesium [9]

Physical Property	Density (g/cm³)	Melting Point (°C)	Specific Heat (Cal/g°C)	Electrical conductivity (%IACS)	Thermal Conductivity (W/mK)	Crystal Structure	Young's Modulus (GPa)
Pure Mg	1.74	650	0.24	39	155	HCP	45

Magnesium and its alloys possess numerous remarkable properties (Table. 2-2) in respect to other engineering material, for example, high strength, low density, good elastic shielding effect, great damping capacity, non-magnetic satisfactory heat conduction and excellent fluidity for casting, negative electrochemical potential, low-heat capacity, recyclable and nontoxic. These properties make magnesium and its alloys increasingly appealing to numerous industries particularly in automotive and aerospace industries, where the strength to weight ratio is a basic issue. Magnesium

offers noteworthy open doors for lightweight applications in automotive, aerospace, medical and power-tools industries [9].

A liberal effort was begun once again the earlier decade to create high-quality magnesium compounds utilizing an assortment of methodologies, including solid solution strengthening and precipitation strengthening. Commercial magnesium alloys that can be alternative for few aluminum alloys include AZ315 and ZK60 [10]. Table 2-3. Manifests the effect of alloying elements on the mechanical properties.

Table 2-3. The effect of alloying elements on the magnesium [10, 11]

Alloying Element	Effect on the Mechanical Properties
Aluminum (Al)	Increases tensile strength and hardness Forms precipitation of intermetallic phase (Mg ₁₇ Al ₁₂) Improves castability Increases corrosion resistance
Zinc (Zn)	Increases tensile strength and hardness Refines grain structure Improves castability Increases corrosion resistance
Manganese (Mn)	Increases yield strength Increase corrosion resistance while reducing the effect of iron
Silicon (Si)	Improves creep resistance Forms Mg ₂ Si particles Increases molten metal viscosity Reduces castability Reduces corrosion resistance
Rare Earth Metals	Reduces the freezing range Increase tensile strength and hardness

2.2.2. Cast magnesium alloys

The improvement of magnesium casting started in 1921 when Dow began to produce pistons made of magnesium. Casting of magnesium developed in prevalence and turned out to be developed through out World War II with the fabrication of parts for defense, aerospace and automotive application. This improvement was in gravity sand, permanent mold, and high-pressure die casting (HPDC). The most recent innovation has created amazing castability [11] on new generation magnesium alloys and the emphasis has been on thin-walled die casting for applications in the automotive industry. Magnesium casting has kept on extending in the automotive industry, electronics, aerospace, and defense and power tools. Currently casting is the prevailing fabrication process for magnesium segments and represents approximately 98% of all structural applications of magnesium [12]

There are numerous unique characteristics that magnesium possesses, including hardening which provide it favorable position over other cast metals including aluminum and copper. These incorporate magnificent ease and a low susceptibility to hydrogen porosity [12].

The most well-known casting method for magnesium alloys is high-pressure die casting (HPDC) [13, 12]. For this method to be done liquid metal is inserted at high speed and high pressure into a metal mold. Figure. 2-9 depicts this process.

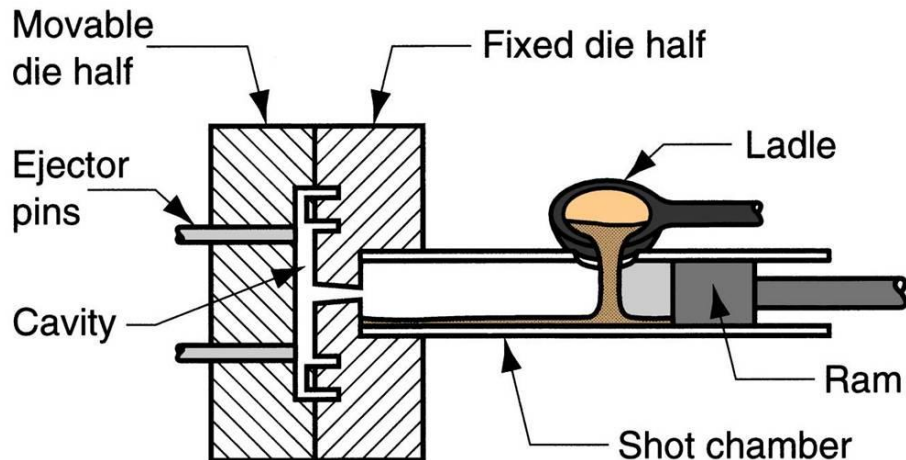


Figure 2-9. Cold chamber die casting method.

The molten magnesium alloys can be held in the molds made of ferrous materials. This is because the melted magnesium does not assault iron as molten aluminum does. Due to this reason, it is common for the magnesium alloy to be dissolved and transported in steel crucibles, tools and devices.

For manufacturing light metal components, high pressure die casting is the most preferable method. It renders magnificent flexibility in the process of design and is enormously economical to fabricate components though this process. Because magnesium alloys are excellent for die filling, the components manufactured from high pressure die casting can be long in length, thin walled, and complexed. This allows for the substitute of steel parts, which have been made of numerous parts welded or joined together, with the solid magnesium parts. A great benefit of magnesium die casting is that it tends to be structured with both thin and thick walls, slenderer walls where the strength is not vital and thicker walls where strength is required. Also, it is conceivable

to cast magnesium alloys with slender walls than aluminum alloys. As well, magnesium has a casting cycle time which is shorter than aluminum [12]. Table 2-4. below shows the design parameters and manufacturing characteristics for magnesium die casting.

There are two different types of high pressure die casting, one is hot chamber die casting and another is cold chamber die casting. In most of the magnesium die casting components are fabricated by cold chamber die casting process [12]. One of the issues with casting magnesium alloys is the emergence of defects (porosity and inclusions) that can occur amid the casting process. These defects can turn into stress concentrations which can create crack initiation points. Thereby, this can initiate the fatigue crack which unfavorably can reduce the component life and turn into a reduced cyclic strength [14].

Table 2-4. Design parameters and manufacturing characteristics for magnesium die casting [13]

Design Parameter	Limit
Dimensional Tolerance (mm/min)	±0.001
Draft angle (°)	0–1.5
Minimum wall thickness (mm)	1–1.5
Casting/molding cycle time (unit)	1.0–1.4
Typical die life (×1000 shots)	250–300
Trimming cycle time (unit)	1
Machinability	Excellent
Welding/joining	Fair
Surface finishing	Excellent
Recyclability	Good

2.2.3 Wrought magnesium alloys

Wrought magnesium is a cast metal, which has been worked upon, in cold condition; without heating. The distinctive metallurgical characteristics of castings are acquired during solidification, whereas with wrought materials, they are acquired during mechanical deformation.

The principal metallurgical difference between castings and wrought materials is that castings lack homogeneity.

1. They do not have the benefit of hot work to accelerate the diffusion of the chemical elements to achieve homogenization.
2. Cast alloys require significantly longer soaking times to achieve homogenization.
3. Solidification castings contain high residual stresses from solid shrinkage, unless they are removed by a stress relief annealing process [15].

Mg wrought applications have been significantly hampered by the relatively poor ductility and formability of magnesium at room temperature. Until the late 1990s, the work on wrought magnesium has focused to a great extent on extrusions and forgings. Extrusion alloys AZ61 (Mg-6Al-1Zn), ZK60 (Mg-6Zn-0.6Zr), and forging alloys AZ80 (Mg-8Al-0.5Zn), ZK60 (Mg-6Zn-0.6Zr) have been improved and utilized for ambient temperature applications. Sheet alloys developed were the commercial AZ31 (Mg-3Al-1Zn), AZ61 (Mg-6Al-1Zn), ZK60 (Mg-6Zn-0.3Zr), ZK31 (Mg-3Zn-0.6Zr), and

experimental alloys containing Li, Zr and/or Mn. Recent alloy development activities in wrought Mg have begun due to the interest in using lightweight magnesium as automotive sheet and extrusions for vehicle body applications [16].

The requirements for weakened or randomized textures for improved formability in wrought Mg alloys, combined with the need for adequate strength, are the driving forces for investigating new Mg-Li alloy development strategies.

2.2.4 Mg-Li

Addition of Li (body center cubic crystalline structure) in Mg creates more active slip system in its crystalline structure, therefore helps to improve strength and ductility of the Mg. Also, lithium (Li) aids to enhance plasticity of Mg developing ultra-light metallic alloy with density of 1.35-1.65 g/cm³ [17].

The phase diagram illustrated in Fig. 2-10 shows that for less than 5wt% of Li in the Mg matrix, the Mg-Li alloy possesses single α -Mg phase with HCP structured solid solution, up to this range Li is soluble in Mg [17]. For Li concentration between 5wt%-10wt% [2] the value of Mg crystal lattice is reduced, and the alloy exhibits dual phased structure [HCP+BCC], but for Li amount more than 10wt% the structure turns into BCC only with β -Li phase [17]. Because of the presence of β phase in the structure, the ductility of the alloy increases remarkably but strength reduces, as a result for the application where the strength of the material is the highest priority, HCP structured α -

Mg phase is preferred, as this type of structure ensures good strength materials for practical application [18].

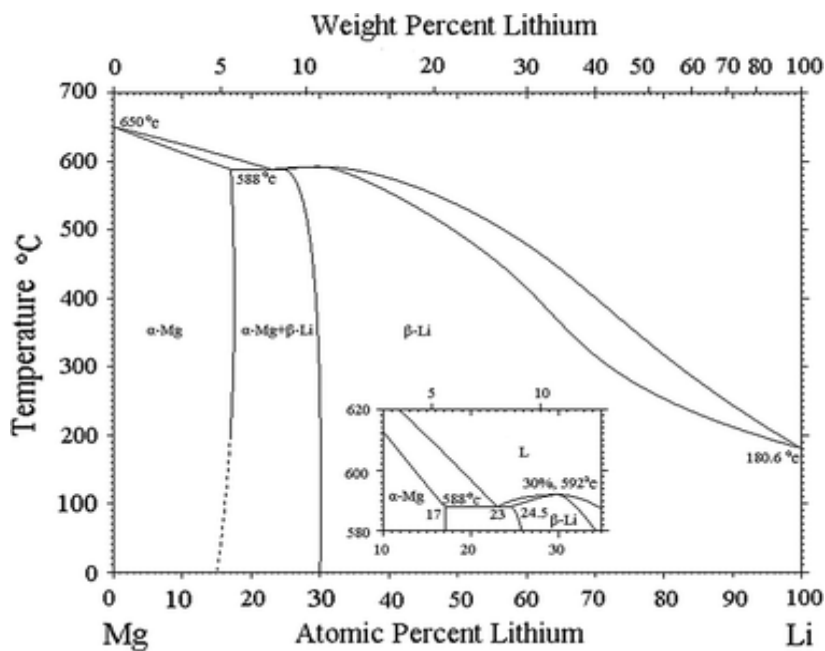


Figure 2-10. Phase Diagram of Mg-Li alloys [19].

2.2.5 Effect of Li on Mg

Conventional Mg-Li alloys normally relied upon large Li additions that change the hcp structure of Mg to BCC. In the Mg-Li binary system, when the Li content is greater than 5 wt%, β phase (Li solid solution) appeared in the alloys. Little amount of lithium alloying inclusion also helped to improve the room temperature formability of magnesium, which is correlated with activation of non-basal slip due to the decrement in the axial ratio (c/a) of magnesium as a function of lithium. As lithium is added to magnesium, the c value of the hcp crystal decreases quicker than a value, which leads to a decrement in the c/a ratio, and results in stress for basal slip enlarging relative to that

for prismatic slip, and hence proliferates activation of non-basal prismatic planes. TEM studies manifests that lithium additions also increment the glide of dislocations on pyramidal planes. It is already proved that dislocations disperse into partial dislocations, and lithium may reduce the energy of the stacking fault, and thereby raise the stability of the dislocation. Lithium can transform the crystallographic texture by remodeling the balance of deformation mechanisms, which in turn influences the texture [20].

The impact of small amounts of Li on the c/a ratio and grain size of Mg was examined by researchers in Mg-Zn-Li and Mg-Zn-In-Li solid solution alloys. The mono-valent Li diminished the axial ratio (c/a) of magnesium from 1.624 to 1.6068 inside the 0–16at%Li territory (Fig. 2-11). This was ascribed to the decrement in c/a, which prompts a decrease of the c-spacing and in c/a as well. An imperative impact of c/a was found in the twinning behavior of the alloys [20].

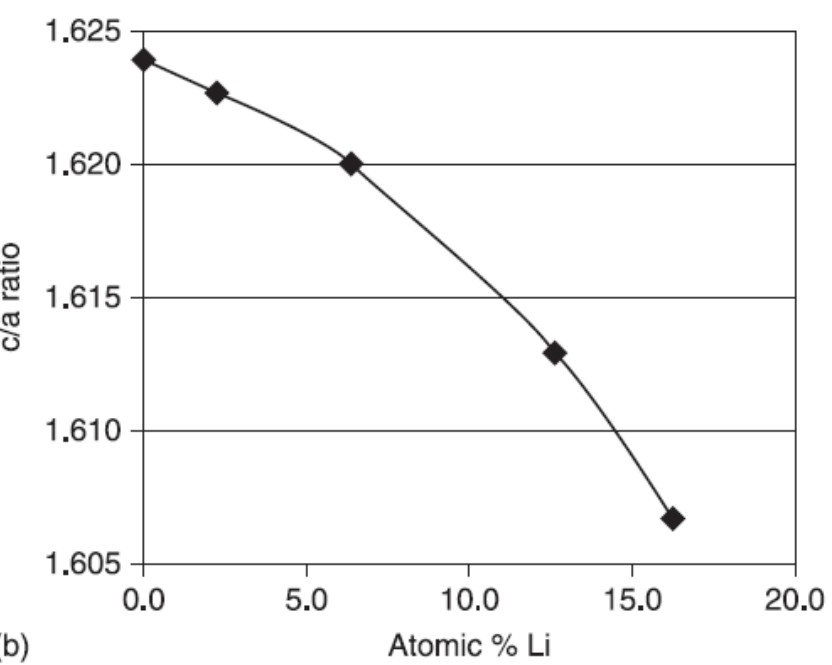
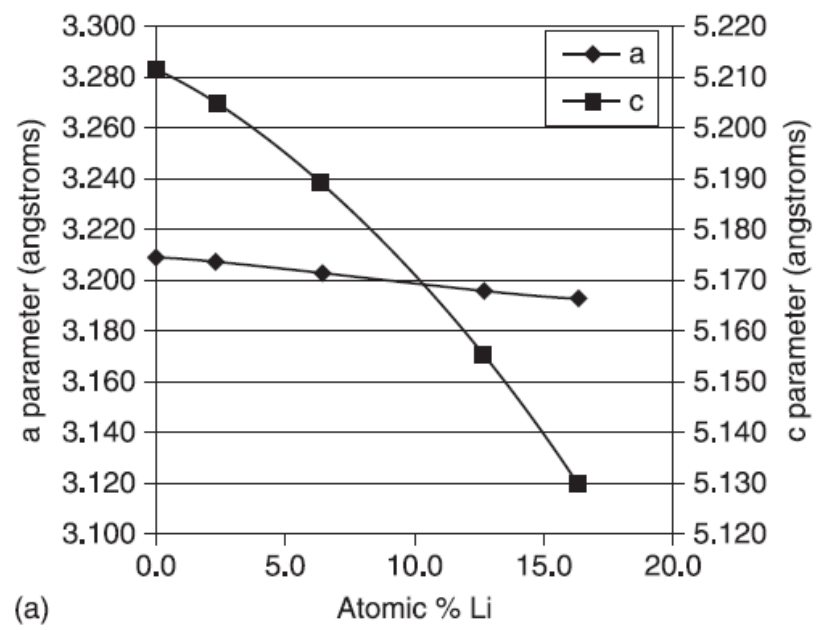


Figure 2-11. Effect of Li on Mg. a) Lattice Parameters; b) axial ratio [20].

2.2.6 Microstructure & crystal Structure

According to the Mg-Li phase diagram, the alloys exhibit two phase structures of α (hexagonal close packed (hcp) (Fig. 2-12a)) Mg-rich and β (body-centered cubic (bcc) (Fig. 2-12b)) Li-rich phases at room temperature when 5-11% Li is added to magnesium. Further additions of Li (more than 11%) can transform the hcp α -Mg solid solution into highly workable, body-centered cubic alloys [21]. And for less than 5% addition of Li the structure has only α -Mg phase.

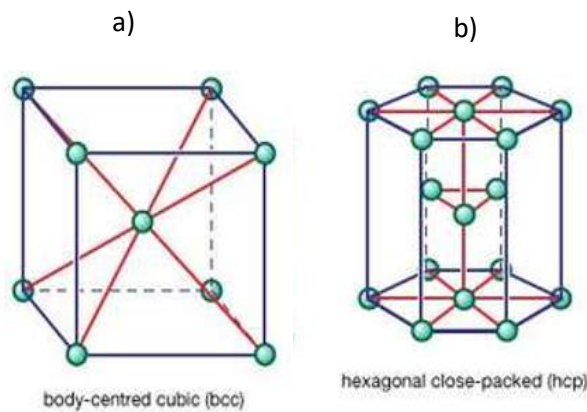


Figure 2-12. Common metallic crystal structure a) BCC structure, b) HCP structure.

The microstructure and composition of a material decides a considerable lot of its physical, and the majority of its mechanical, properties. The microstructure is controlled by the composition and processing conditions. The evolvement of the microstructure during processing (for example, thermomechanical processing) may constrain the processing operations that can be done. Also, microstructures which result in poor properties of the completed part may shape in the work piece.

Microstructures of polycrystalline metals and alloys have massive effect on materials properties. Practically all mechanical properties, for example, quality, strength or creep resistance, rely upon the grain size of the material, where the grain boundaries that can act as two-dimensional defects play a fundamental role in processing. Therefore, having proper knowledge on grain microstructures and their transformation due to recrystallization and grain growth is considerably important since a modification in microstructure yields the materials with new properties, which might make the material unusable in applications [22]. Fig.2-13 shows a typical microstructure of Mg-Li alloy with α -Mg phase, precipitates and twins.

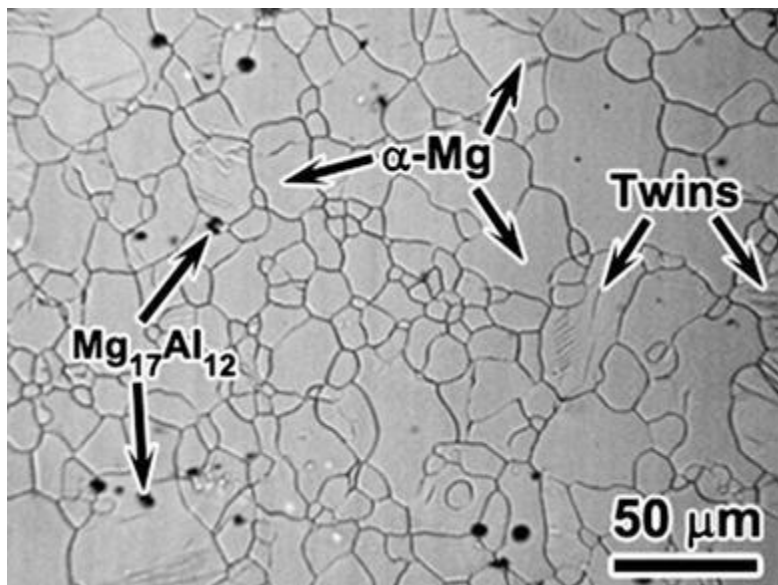


Figure 2-13. Typical microstructure of Mg-Li-Al alloy [23].

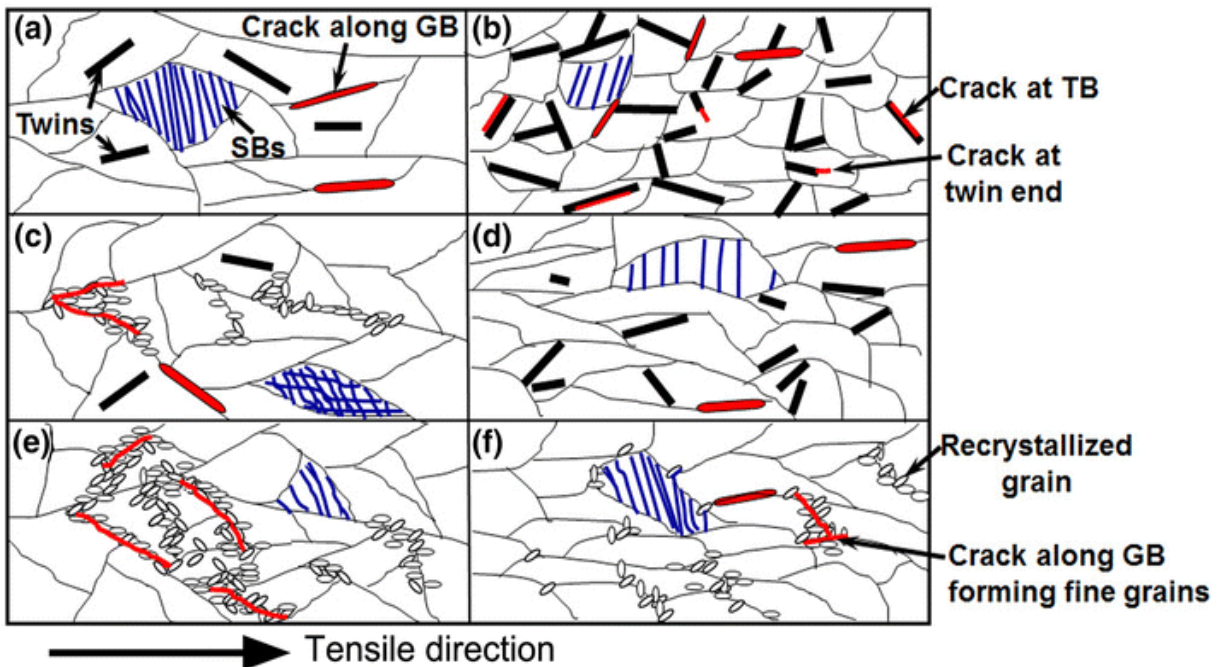


Figure 2-14. Illustration of the major differences between deformation and damage features and microstructures in AZ31 alloy [23].

Through microstructure investigation, almost certainly, the deformation and damage features can be comprehended. In Fig. 2-14 Yan *et al.* [23] indicates clearly the significant differences in the deformation and damage features and microstructures on of AZ31 Mg alloy was tested through tensile stress at a low and a high strain rate respectively, at elevated temperatures. The elongated grains along with a greater amount of (slip bands) SBs and a fewer number of twins and the cracks beside (Grain Boundaries) GBs are generated (Fig. 2-12a). Hence, at a high strain rate, a high density of twins, lots of cracks forming along GBs and at TBs or the end of twins, and sparser SBs are identified (2-12b). Similar situations are also presented at room temperature. Also, at higher temperature, few recrystallized grains integrated with the cracks are affecting nearby

GBs at low strain rate, and the SB density is still higher, but only very few twins are formed (Figs. 2-12c). At high strain rate, the twin density seems quite high, and the cracks besides the GBs can be identified only (Figs. 2-12d). At high temperature, more number of recrystallized grains together with large-sized cracks forms alongside the GBs at a low strain rate (Figs. 2-12e), on the other hand, at a high strain rate, the recrystallization rate gets slower (Figs. 2-12f) [23].

2.3 Nanoindentation

Indentation is one of the essential techniques for looking at mechanical properties of engineering materials. Nano indentation strategy is ultra-local and less invasive, in contrast to the tension/compression tests, in which the indenter is inserted into the surface of the sample. Recognized by the indentation load L and the penetration h , micro indentation tests are portrayed by $200 \text{ mN} < L < 2 \text{ N}$ and $h > 0.2 \mu\text{m}$, whereas in nanoindentation L ranges between a few μN and about 200 mN , while h fluctuates from a couple of nm to around a couple μm . Subsequently, the indented zone in nanoindentation is for the most part on the nm or a couple μm scale [24].

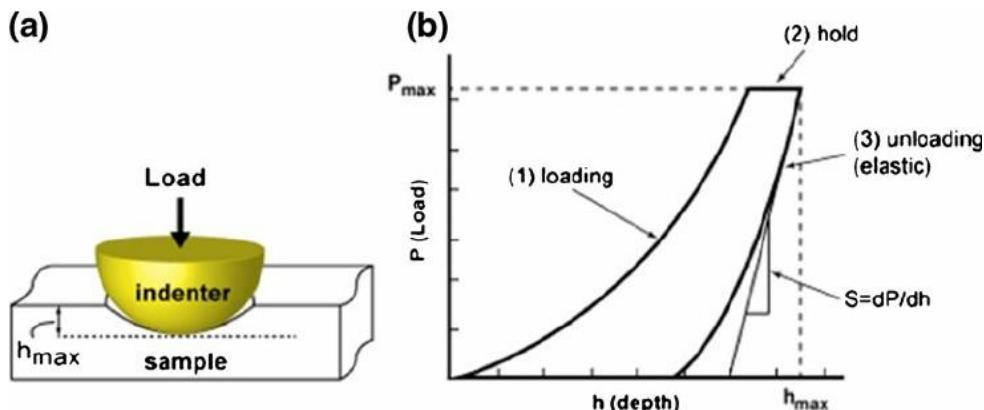


Figure 2-15. a) Nanoindentation b) Load-depth graph [24].

A Nano indentation test usually conducted in three steps, a) the loading step (Fig. 2-15a) b) an intermediate step where the peak load is hold for a definite time, and c) the unloading step (Fig. 2-15b). If determination of creep is not necessary in that case the intermediate step is done for a short span of time, generally 2-4 seconds (Fig. 2-16).

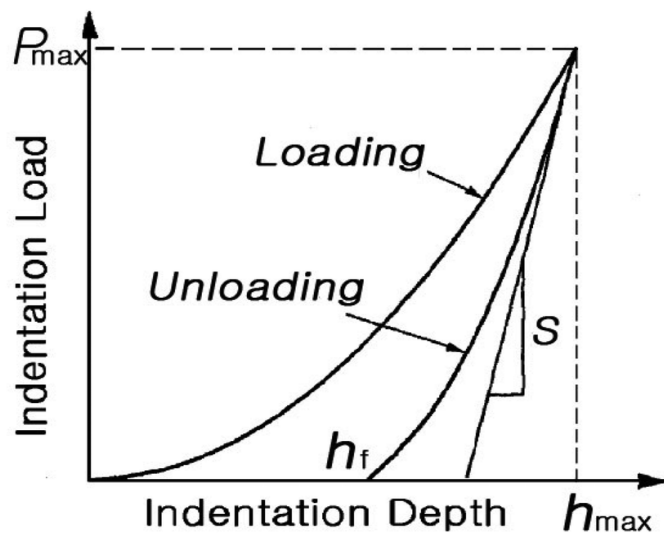


Figure 2-16. Load-displacement curve recorded during instrumented indentation [25].

It is a well-established, accurate, non-destructive and convenient method to measure mechanical properties of materials at small scale. Due to its precise load controlling capacity it has been in use to measure hardness, elastic modulus, creep parameters and strain rate sensitivity increasingly. Hardness value for nanoindentation can easily be calculated using Oliver and Pharr equation [26], where, a load, P , is applied on a flat sample and the resulting displacement, h , is recorded to determine the elastic modulus, E , and hardness, H , of the sample. Here the indentation hardness is defined as;

$$H = \frac{P}{A_c} \quad 2-1$$

From the following equation the reduced elastic modulus of the indented material is obtained [23]:

$$\frac{1}{E_r} = 1 - \frac{1 - v^2}{E} + \frac{1 - v_i^2}{E_i} \quad 2-2$$

Where, E_r is the reduced elastic modulus, E , v are the modulus and Poisson's ratio of the indented material. E_i , v_i are the modulus and Poisson's ratio of the indenter tip (diamond) [27].

2.3.1 Types of Nano indenter

The Berkovich indenter tip (Figs. 2-17, 2-18) is the most commonly employed indenter tip for the instrumented indentation testing (IIT) to quantify mechanical properties on the nanoscale. The Berkovich indenter tip is a three-sided pyramid that can be ground to a point and subsequently keeps up a self-comparative geometry to extremely little

scales. It prompts versatility at exceptionally little loads which delivers a significant proportion of hardness. The Berkovich indenter tip has a substantial included point of 142.3° which limits the impact of erosion.

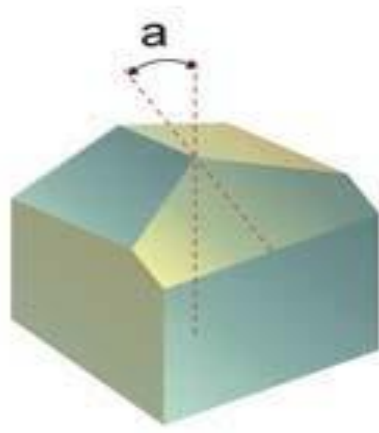


Figure 2-17. Schematics of Berkovich indenter [28].

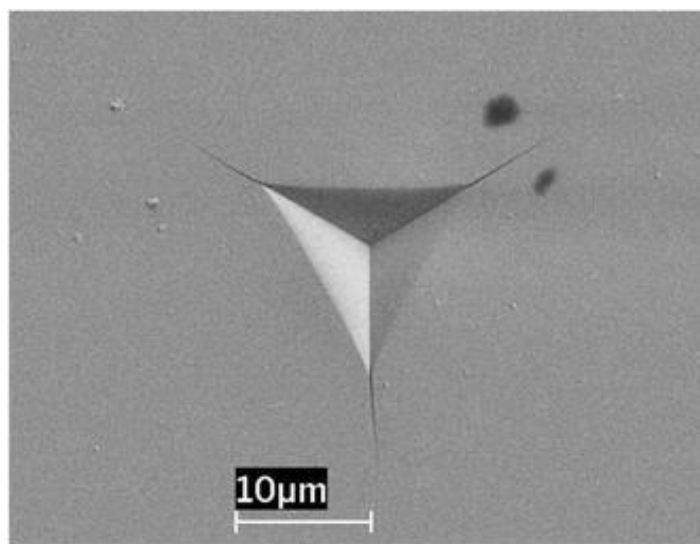


Figure 2-18. Indentation mark over the sample surface [25].

2.4 Thermomechanical processing (TMP) of Mg-Li alloys

From fundamentals of metalworking process at high temperature, we can say that, compression, tension, bending and shearing stresses are applied on to the work piece to give it a shape. It occurs due to plastic deformation which gives the product the required geometry. Fig. 2-19 talks about stress-strain relationship quiet well, when the TMP starts, once the metal has reached its yield point, it starts to flow under the influence of stress state. This is the plastic regime where stress is not directly proportional to strain. The manner of flow or deformation is dependent on the stress state.

Flow curve indicates whether metal is readily deformed at given conditions i.e., strain rate, temperature. Flow curve is strongly dependent on strain rate and temperature.

To determine the flow curve Hook's law is used $\sigma = K\varepsilon^n$. It determines the yield point, beyond which metal deforms plastically [29].

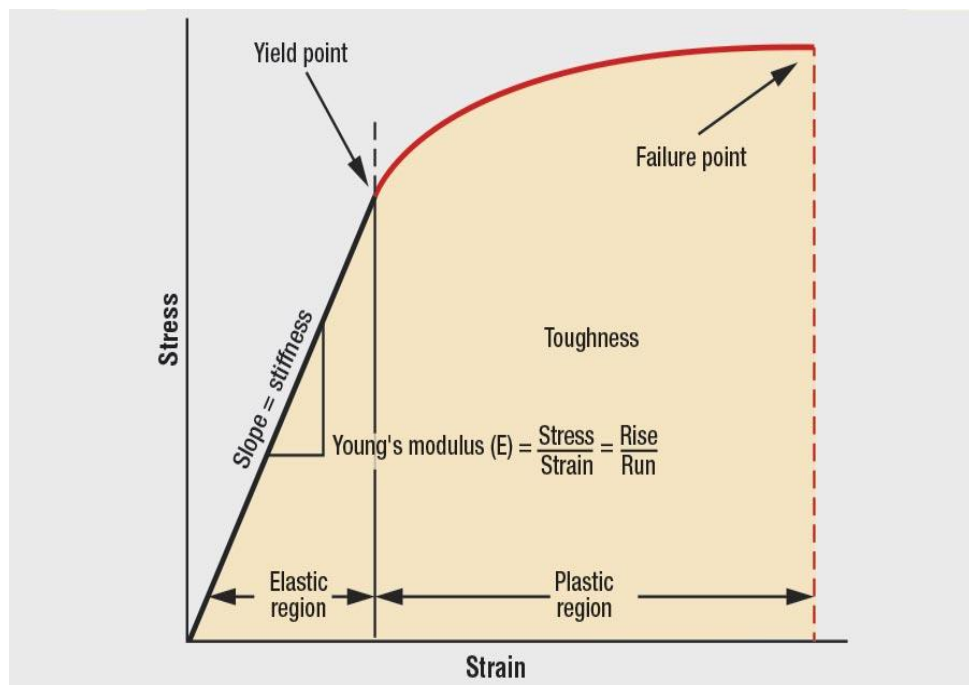


Figure 2-19. Stress-strain graph [30].

During cold working of metallic materials – for example by rolling – the material will be subject to significant plastic deformations that greatly increase the strength and hardness of the metal, but which also makes it more brittle and prone to damage and fracture in subsequent manufacturing steps. To restore ductility, a heat treatment is usually performed following cold working. During annealing, the material is kept at an elevated temperature for some duration of time. During annealing, the cold worked material will undergo a sequence of recovery, recrystallization and grain growth, which eventually reduces the hardness and improves ductility.

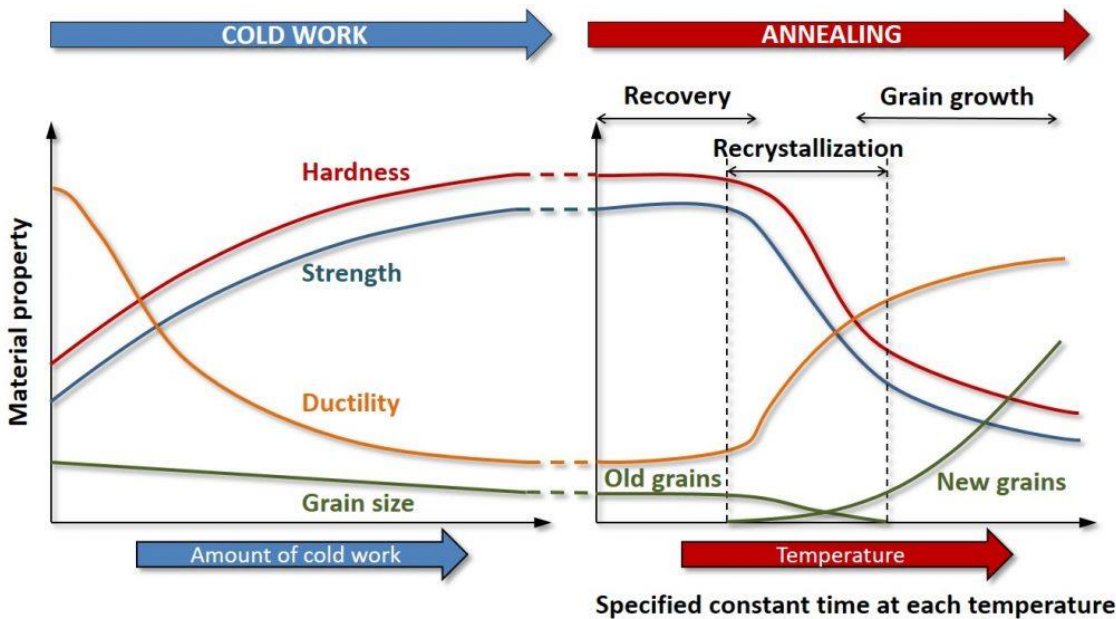


Figure 2-20. Illustration of material property and grain size variation during cold working (left) and subsequent annealing (right) of a metallic material [31].

It is common technique utilized to improve the mechanical properties of Mg alloys. Especially in case of Mg-Li alloys, the TMP possesses a huge impact to change and develop the mechanical properties. Hot deformation of metallic materials which includes work hardening, dynamic recovery and dynamic recrystallization, can prompt changes in the microstructure of the deformed material which are specifically reflected in the flow stress curves. Fig. 2-20 illustrates the effect of TMP in Mg-Li alloys. Cold working increases the hardness, strength but reduce the ductility along with grain size. Due to increase in temperature annealing starts and releases the internal stress resulting in dynamic recovery. Hot working involves deformation at temperatures where recrystallization can occur and flow stress goes down, improves ductility but reduces strength and hardness. At the end new grains form.

2.4.1 Effect of temperature

During the thermomechanical processing of metallic alloys, temperature might have effect on two different ways by annealing or hardening. Annealing reduces internal stress, obtain softer and ductile structure and get more stable state. Hardening increases strength, hardness, wear resistance and get metastable state. From stress-strain graph (Fig. 2-21) it has been observed that for Mg-Li type of alloys with increasing testing temperature flow stress goes down when yield strength and tensile strength decreases, also, the percentage elongation increases [32].

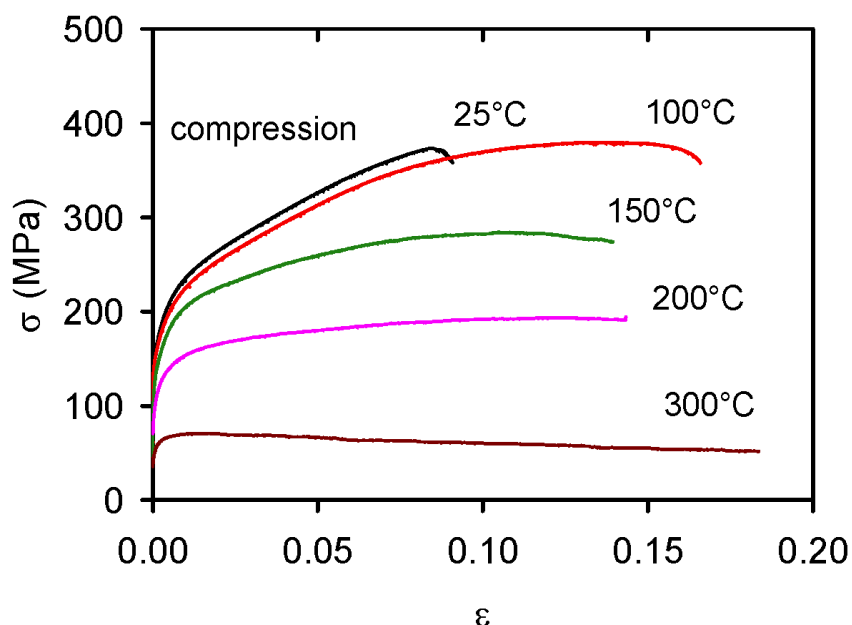


Figure 2-21. Effect of temperature [32].

2.4.2 Effect of strain rate

Flow stress: Flow stress is defined as the true stress required to continue plastic deformation at a strain [32]. The strain rate is strongly affected by the temperature.

$$Y_f = K \dot{\varepsilon}^m \quad 2-3$$

Here, Y_f = Flow stress, K = strength coefficient, $\dot{\varepsilon}$ = strain rate.

Fig. 2-22 depicts that with increase of strain rate flow stress goes up. For decrease of strain rate vice versa.

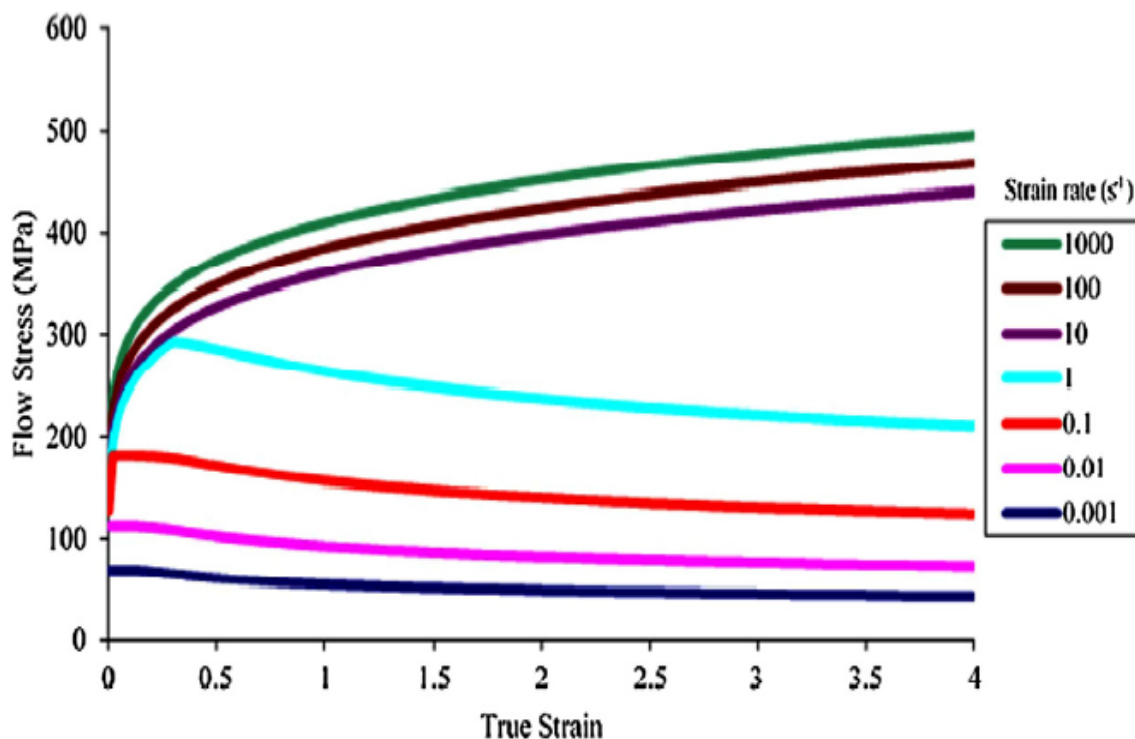


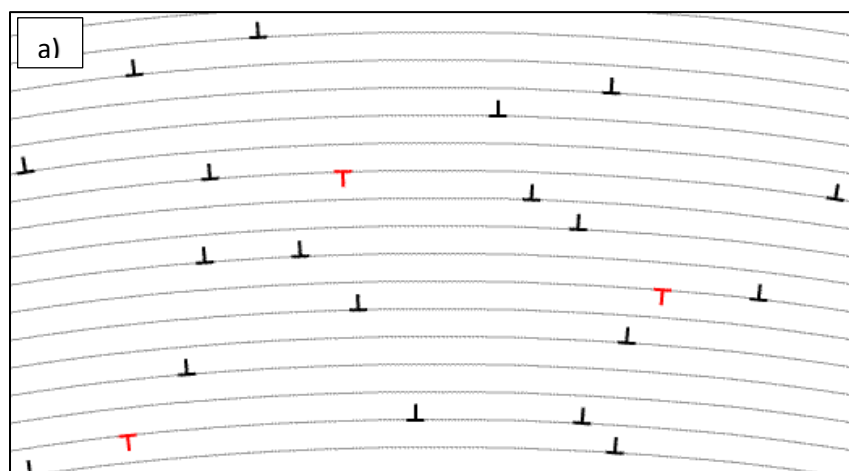
Figure 2-22. Effect of strain rate [33].

2.5 Microstructure (effect of TMP on microstructure)

2.5.1 Dynamic recovery (DRV)

In case of metallic alloys, after heating the samples at certain temperature, there is increased diffusion along the grain boundaries. Due to this enhanced dislocation motion, dislocation density reduces by annihilation (Fig. 2-23a). Thus, low energy dislocation configurations formed. Therefore, relieve of internal strain energy.

Toward the start of stressing, there is an expansion in the work hardening due to dislocation generation and accumulation. As the deformation proceeds with, some portion of the stored energy is discharged with the dislocation annihilation through dynamic recovery. As a result, the stress level increments and can locate a stationary state in materials with high level of stacking fault energy (SFE) [34]. Fig. 2-23b gives an example of annealing during edge dislocation.



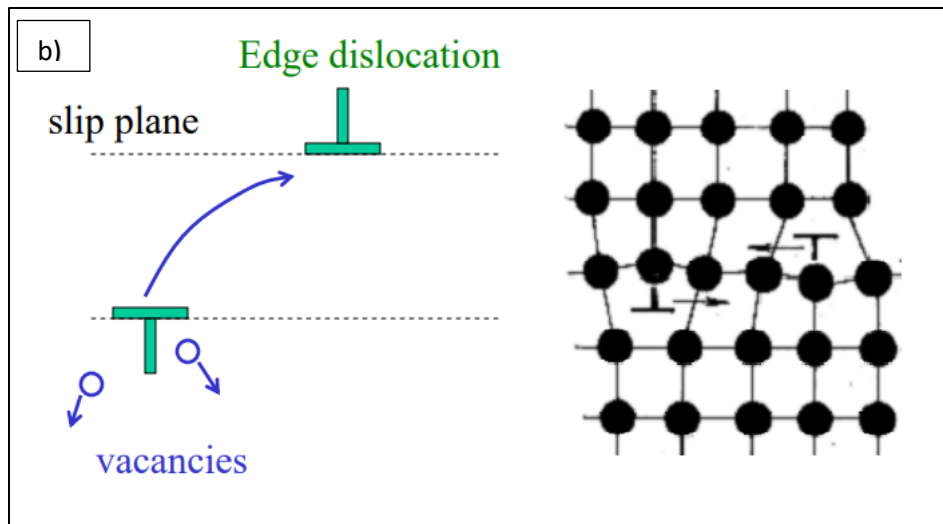


Figure 2-23. a) Dynamic recovery by annealing, b) annealing by edge dislocation [35].

2.5.2 Dynamic recrystallization (DRX)

Even after recovery the grains can be strained. These strained grains of cold-worked metal can be replaced, upon heating, by strain-free grains with low density of dislocations. This occurs (Fig. 2-24) through recrystallization – nucleation and growth of new grains. The driving force for recrystallization is the difference in internal energy between strained and unstrained material. Grain growth involves short-range diffusion and the length of recrystallization depends on both temperature and time. Recrystallization is slower in alloys as compared to pure metals.

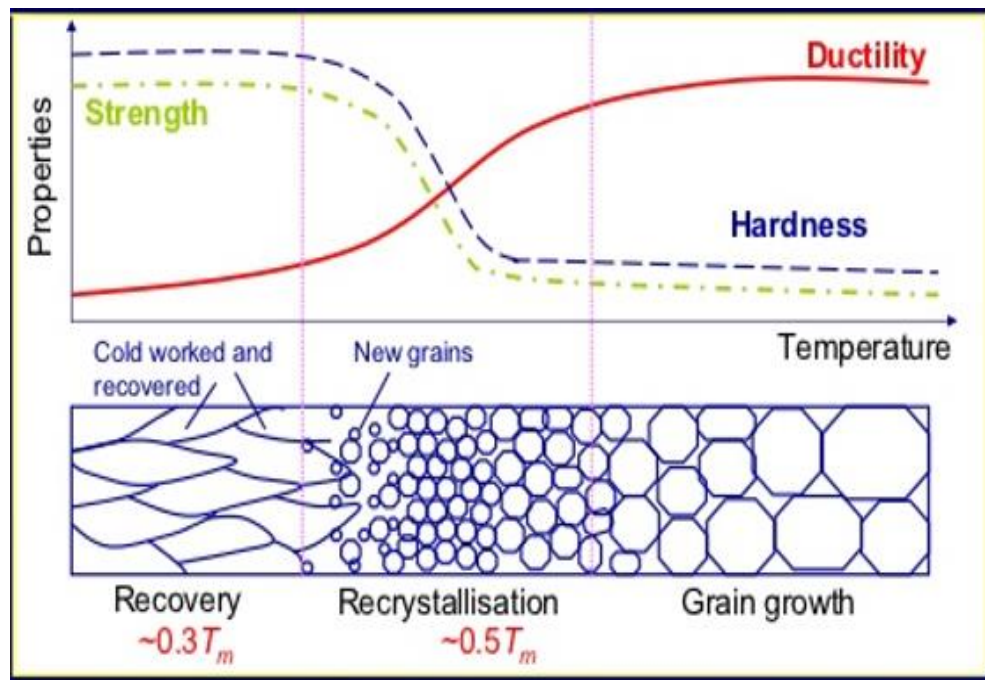


Figure 2-24. Effect of temperature on metal forming process [8].

2.5.3 Grain growth

If deformed polycrystalline material is maintained at annealing temperature following complete recrystallization, then further grain growth occurs. Driving force is reduction of the total grain boundary area and, hence, the energy of the system. Big grains grow at the expense of the small ones. Grain growth during annealing occurs in all polycrystalline materials (i.e. they do not have to be deformed or undergo recrystallization first). Boundary motion occurs by short range diffusion of atoms across the grain boundary → strong temperature dependence of the grain growth.

2.6 Application

2.6.1 Applications of Mg and its alloys

The present usage of the most accurate alloying combinations in magnesium alloy, the corrosion resistant of magnesium has considerably developed. The fast-growing market and legislative issues on automotive industry to manufacture lighter, better fuel efficient and high-performance vehicle resulted in the utilization of magnesium and its alloys.

- Automotive application**

The utilization of magnesium in car body applications is restricted however has extended as of late. GM has been utilizing a magnesium since the presentation of the C-5 Corvette in 1997. Magnesium is additionally utilized in the Cadillac XLR roadster's retractable hard-top convertible rooftop and the rooftop top casing. The Ford F-150 has covered magnesium castings for its radiator support. In Europe, Volkswagen and Mercedes have spearheaded the utilization of thin-wall magnesium die castings in body panel applications. The one-part cast entryway inward for the Mercedes S-Class Coupe is just 4.56 kg. The way to producing these flimsy divider castings (around 1.5 mm) relies on casting configuration utilizing appropriate radii and ribs for smooth pass on filling and to solidify the parts. This magnesium made thin wall, for example, door inners, can frequently counterbalance the material cost penalty of magnesium over steel

sheet metal development because of part fusion. Various prototypes have been made utilizing sheet magnesium while production application has restrictions. General Motors made model hoods for the Buick LeSabre in 1951, different body boards for the Chevrolet Corvette SS Race Car in 1957, and hoods for the Chevrolet Corvette in 1961. As of late, Volkswagen made a model hood for the Lupo a couple of years prior. GM has made various boards including a hood, entryway internal board.

Figure 2-25. Sheet magnesium center console cover in Porsche Carrera GT. Decklid inward, lift gate, and different fortifications, some of which are appeared in Fig. 2-26. Chrysler LLC has played out various examinations utilizing magnesium sheet, including the internal board and a magnesium-concentrated body structure.



Figure 2-25. Highlights one successful application of magnesium in producing center console cover in Porsche Carrera GT [16].

From the Table. 2-5, we can see numerous potential automotive applications of wrought magnesium alloys in different systems.

Table 2-5. Potential automotive application of wrought magnesium alloys

System	Component	Note
Interior	Instrumental panel	Extrusion/sheet
	Seat components	Extrusion/sheet
	Trim plate	Sheet
Body	Door inner	Sheet
	Tailgate/liftgate inner	Sheet
	Roof frame	Extrusion
	Sunroof panel	Sheet
	Bumper beam	Extrusion
	Radiator support	Extrusion
	Shotgun	Sheet/Extrusion
	A and B pillar	Sheet
	Decklid/hood inner	Sheet
	Hood outer/fender	Sheet
	Decklid/door outer	Sheet
	Dash panel	Sheet
Chassis	Frame rail	Extrusion
	Wheel	Forging
	Engine cradle	Extrusion
	Subframe	Extrusion
	Control arm	Forging

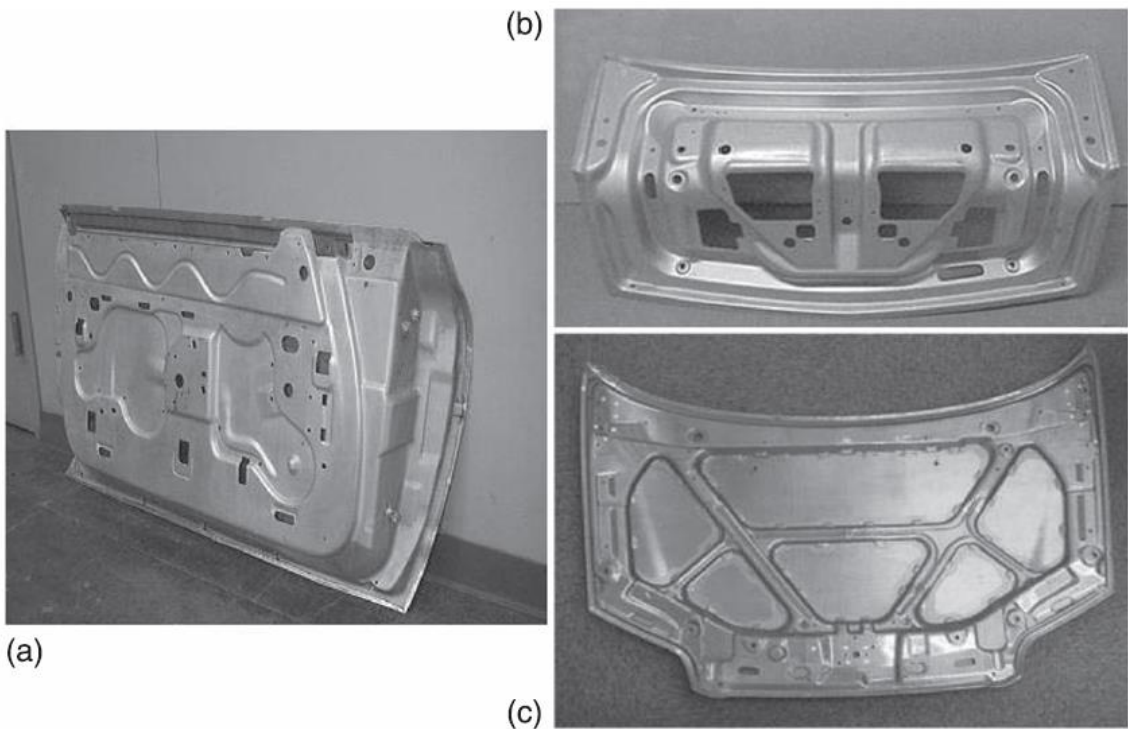
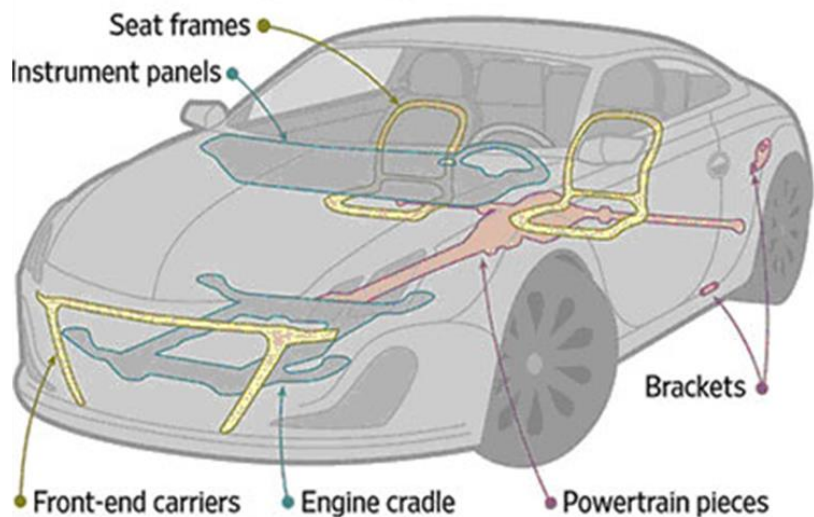


Figure 2-26. Magnesium sheet panels formed recently by General Motors. (a) Door inner panel; (b) decklid inner panel; (c) hood [16].

In body board applications where, bending stiffness has often design limitation, magnesium sheet metal can provide around 61% mass saving. Most of the applications regarding magnesium related to “inner” panels, which make the structure of the vehicle not noticeable outwardly of the vehicle. There are two facts behind this kind of limited application of magnesium. To begin with, the surface finishing of the recent accessible magnesium sheet requires noteworthy surface finishing in contrast to aluminum or steel, and then, the restricted formability at room temperature makes making the forming assembly for external use. This implies all things considered, the main business applications for magnesium sheet will be inward boards. However, raised temperature

framing of magnesium and protection from corrosion by applying coatings further force a cost burden for magnesium sheet applications. The improvement of new sheet composites for near to room temperature shaping is required, alongside low cost and vigorous coatings to help restricting corrosion. Like magnesium sheet, magnesium extruded sheets for car applications are still in the advancement stage, with numerous model parts, for example, frame rail for the Volkswagen 1-Liter Car and bumper beams. However, the utilization of magnesium in structural applications would require greater advancement to meet all basic and budget.

Leading automobile makers such as Audi, Daimler Chrysler (Mercedes-Benz), Toyota, Ford, BMW, Jaguar, Volkswagen, Fiat, Hyundai and Kia Motors Corporation have used magnesium-based materials [9]. Numerous applications of magnesium and its alloys (Fig. 2-27) have been observed during past few decades in aerospace, automobiles, Sports, Consumer electronics, implant material, Body compatibility and Body degradability because of superior and lightweight properties it possesses.



Source: Meridian Lightweight technologies, Wall Street Journal

Figure 2-27. Transportation Application [16].

Mg Car Components: Toyota Camry steering wheel core, Jaguar and Fiat seat support models, AZ91D rear transfer case, AZ91 alloy cam cover for Ford Zetec engine all these are some famous application of this material.

- **Aerospace application**

Magnesium started as a standout amongst the most utilized materials for aviation industry. World War I and World War II magnesium was utilized broadly for the German and US military air ships. The US B-36 has been accounted for to be manufactured with magnesium sheets of 12,200 lbs. whereas 660 lbs. of magnesium castings and 1200 lbs. of magnesium forgings [36]. The commercial aircraft, Boeing 727 components made of magnesium alloys [12]. However, most of the application for magnesium components has been restricted from aircrafts because of the fire hazard

situation that might arise due to the flammability and corrosion problems of magnesium [37].

Recently, the usage (Fig. 2-28) of magnesium alloys in aerospace industry is constrained to engine landing gear and transmission related castings. In major aircraft manufacturers, magnesium alloys are not recently utilized for structural application [38] but is being utilized in the helicopter industry. Below is Table 2-6 of current aerospace applications [12].

Table 2-6. Aerospace application of Mg alloys [12]

Application	Alloy
Sikorsky UH60 Family (Blackhawk) main transmission	ZE41 alloy
Sikorsky S92 main transmission	WE43A alloy
Thrust reverser cascade casting in found on Boeing 737, 747, 757 and 767	AZ92A alloy
Pratt & Whitney F119 auxiliary casing	WE43 alloy
Pratt & Whitney Canada PW305 turbofan	ZE41 alloy
Rolls Royce tray	ELEKTRON ZRE1 alloy

Recently, researchers specialized in the aerospace industry looking for developing new magnesium alloys and fabrication processing for aerospace applications and it is anticipated that magnesium alloys will start to increment being used as structural applications for the aerospace industry [12, 39].

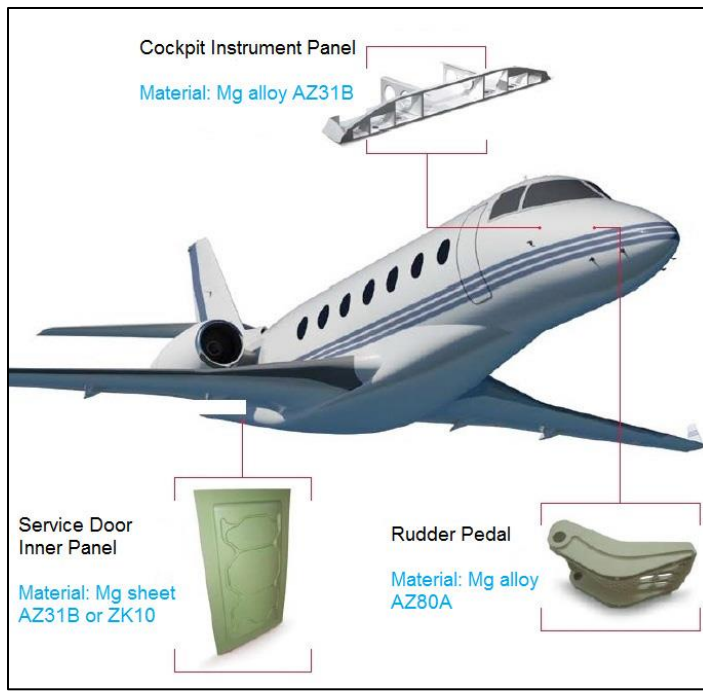


Figure 2-28. Applications for magnesium alloys in the aircraft industry [40].

- **Other Applications**

Besides having the advantage of lightweight and strength magnesium alloys also have very good heat dissipation capacity (100 times superior to plastics), preferred vibration dampening than any other metal, brilliant machinability, and easy to recycle and environmentally friendly [12, 41, 42, 43]. This gives it different advantages for different enterprises including electronic and control devices.

The electron industry has a requirement for light weight, strong, environmentally friendly materials and most importantly, manufacturers are utilizing magnesium alloys to accomplish all these prerequisites [41]. The fantastic castability of magnesium takes

into consideration the plan difficulties of these gadgets to effectively be met making items for customers that are lighter, slenderer and increasingly versatile [41].

Wrought magnesium parts are used in the structural areas because it provides more durable, light weight designs, making them reliable to use for manufacturing products with long life.

2.7 Objective

The main objective of this research is to assess hot workability of Mg-Li alloys at various temperatures and strain rates. The end goal is to establish the correlations between hot working parameters (temperature and strain rate), microstructure, and mechanical properties of the alloy. Both experimental and constitutive modeling have been employed to understand the effect of thermomechanical processing (TMP) parameters (strain rate, temperature) on microstructure and high-temperature flow behavior of the studied alloys. Two Mg-Li alloys, single phase Mg-3.5Li-1Al and dual phase Mg-14Li-1Al alloys, were employed to study the effect of Li percentage on the above-mentioned correlations. At first, true stress -true strain curves plotted from thermomechanical tests (i.e. hot compression) were used to understand the response of the materials, to analyze and understand the microstructure evolution which reflect intrinsic mechanical properties.

Moreover, to assess the mechanical properties of the alloys upon the thermomechanical cycles, an instrumented nanoindentation testing approach were employed. Also, thermomechanically processed ternary HCP α -phase and BCC β -phase alloys are analyzed essentially through microstructural evaluation using OM, SEM. From instrumented nanoindentation Portevin Le-Chatlier effect, hardness and elastic modulus have been observed as outcome of the scrutinize analysis of the mechanical properties. It is intriguing to note that, a microstructural phenomenon, known as Portevin Le Chatlier (PLC) effect, was observed for the Mg-3.5Li-Al, whereas there is no evidence of PLC effect in Mg-14Li-Al alloy discussed in detail in this thesis which needs further investigations. We applied Zener-Hollomon modeling to assess the effect of TMP parameters, i.e. temperature and strain rate, on the microstructural evolution as well.

The motivation for this work, there are very few works that have been done to observe PLC phenomena in Mg-Li alloy using nanoindentation method. Most of the literatures on the PLC phenomenon are based on the experimental result of conventional destructive testing methods (e.g., tensile testing). However, this thesis yields a deep insight in performing nanoindentation which is a non-destructive, reliable characterizing method to the PLC effect. The findings from this study will help improve the new Mg-Li-Al alloy development.

We believe the findings of this study will help improve the new Mg-Li-Al alloys for various applications when weight is the main consideration. This comprehensive study would provide a detailed understanding of the behaviors of two Mg-Li alloys at elevated temperatures which can be used to develop simulation models and constitutive equations of the alloys for various materials selection purposes.

CHAPTER III

3. EXPERIMENTAL TECHNIQUES

3.1. Sample preparation

The materials utilized in this analysis were Mg-Li-Al alloys with two different chemical compositions. Master samples were machined out of the as-extruded Mg-3.5Li-1Al and Mg-14Li-Al wrought alloys. Cylindrical sample with dimensions of Φ 10 mm \times 15 mm was machined out along the extrusion direction for the TMP. The uniaxial hot compression tests were performed at the University of Waterloo using a Gleeble 3500 system. Tests were performed at 250°C, 350°C and 450°C and strain rates of 0.001, 0.01, 0.1, 1 /s.

To assess the effects of the thermomechanical processing parameters for both of the alloys, the nanoindentation tests were performed. After that the microstructures of all these pretreated samples were examined by a metallurgical optical microscope (MODEL-MM500T), scanning electron microscopy (SEM) (MODEL-MM500T), X-ray diffractometer (MODEL-Smartlab 3KW) and, Nanoindentation tester (TI-700 Ubi-1). After TMP all the samples were cut into halves, then hot mounting (Fig. 3-1) was done to ease the polishing and testing process.



Figure 3-1. Samples a) before and b) after mounting.

3.2. Thermomechanical Processing

Using a Gleeble® 3500 thermal-mechanical simulation testing system (Fig. 3-2), the samples were isothermally compressed at temperatures of 250°C, 350°C and 450°C and different strain rates of 0.001 s⁻¹, 0.01 s⁻¹, 0.1 s⁻¹ and 1 s⁻¹ to a final true strain of 1.0. During each test, at first, temperature raises to the set test temperature and then kept for 5 min for the purpose of homogenization. After that, the sample was uniaxially compressed with the present strain rate at the strain of 50%. Upon completion of each test, the metal pieces were water quenched to preserve the deformed microstructure. During testing, stress-strain curves were recorded online using a computerized system attached to the compression system. The thermodynamically compressed samples were then cut into two pieces along the compression axis by an oil-lubricated diamond saw for microstructural assessment and post-TMP mechanical testing. Same technique was followed for all the samples of both compositions.

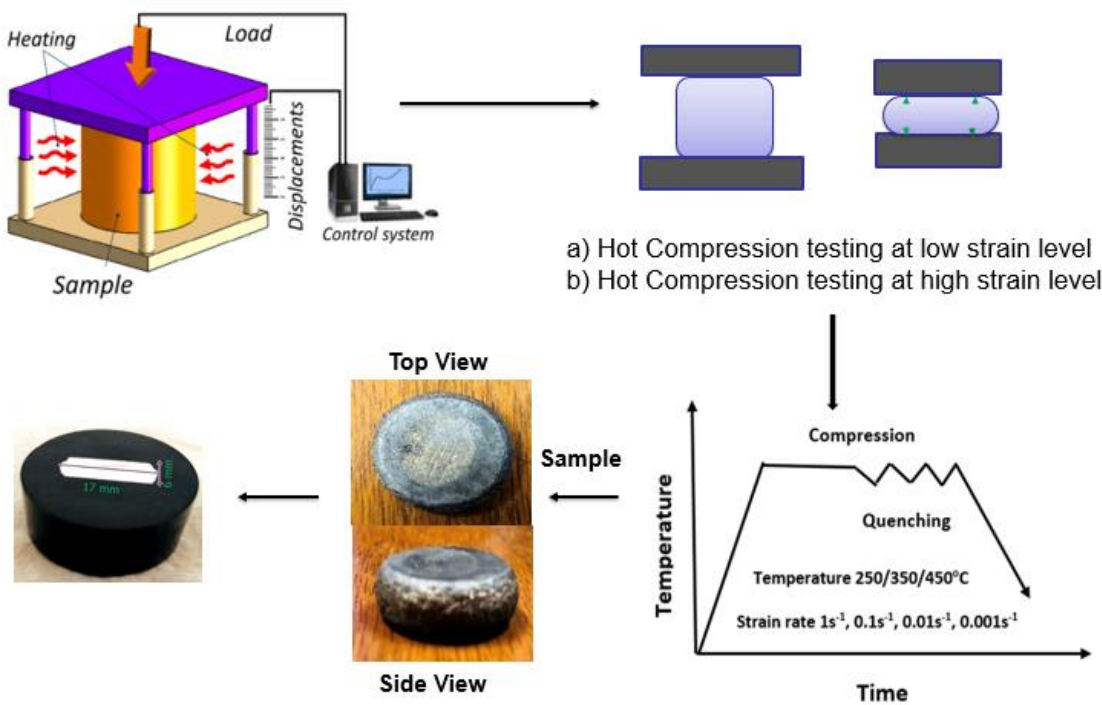


Figure 3-2. Experimental set up for TMP.

Initial dimensions for Mg-3.5Li-Al alloy has been listed in the Table 7. Before TMP all the samples were in around 16 mm length and 9 mm in width. After TMP, samples have achieved changed length and width which were around 17 mm and 6 mm respectively.

For the Mg-14% Li-1% Al addition the change in dimensions are much more noticeable compare to the 3.5% Li addition

Table 3-1. Initial dimensions for Mg-3.5Li-Al

Mg-3.5Li-1Al			
T (°C)	$\dot{\varepsilon}$ (s ⁻¹)	H ₀ (mm)	D ₀ (mm)
250	1	16.19	9.8525
350	1	16.065	9.8525
450	1	17.0925	9.8475
250	0.1	16.645	9.79
350	0.1	16.925	9.845
450	0.1	16.46	9.8525
250	0.01	16.9025	9.795
350	0.01	16.27	9.8325
450	0.01	16.7425	9.87
250	0.001	16.2825	9.85
350	0.001	16.7125	9.8325
450	0.001	16.97	9.86

Table 3-2. Initial dimensions for Mg-14Li-Al

Mg-14Li-1Al			
T (°C)	$\dot{\varepsilon}$ (s ⁻¹)	H ₀ (mm)	D ₀ (mm)
250	1	17.285	9.8525
350	1	16.645	9.8775
450	1	16.6675	9.865
250	0.1	17.025	9.885
350	0.1	17.1975	9.8775
450	0.1	17.275	9.88
250	0.01	16.8925	9.8625
350	0.01	17.125	9.8725
450	0.01	16.395	9.8625
250	0.001	16.4775	9.8725
350	0.001	16.7225	9.87
450	0.001	16.895	9.8725

Table 3-3. Dimensions after TMP for Mg-14Li-Al

Mg-14Li-1Al			
T (°C)	$\dot{\varepsilon}$ (s ⁻¹)	H ₀ (mm)	D ₀ (mm)
250	1	17	4
350	1	17	6
450	1	21	4
250	0.1	17	4
350	0.1	17	4
450	0.1	20	4
250	0.01	17	4
350	0.01	17	4
450	0.01	20	4
250	0.001	17	6
350	0.001	17	6
450	0.001	18	5

3.3. Nanoindentation

Nanoindentation system (Fig. 3-3) continuously measured force and displacement (depth). Utilizing the Oliver and Pharr method [44], the hardness and elastic modulus were calculated from data (load/depth) achieved during experimental analysis.

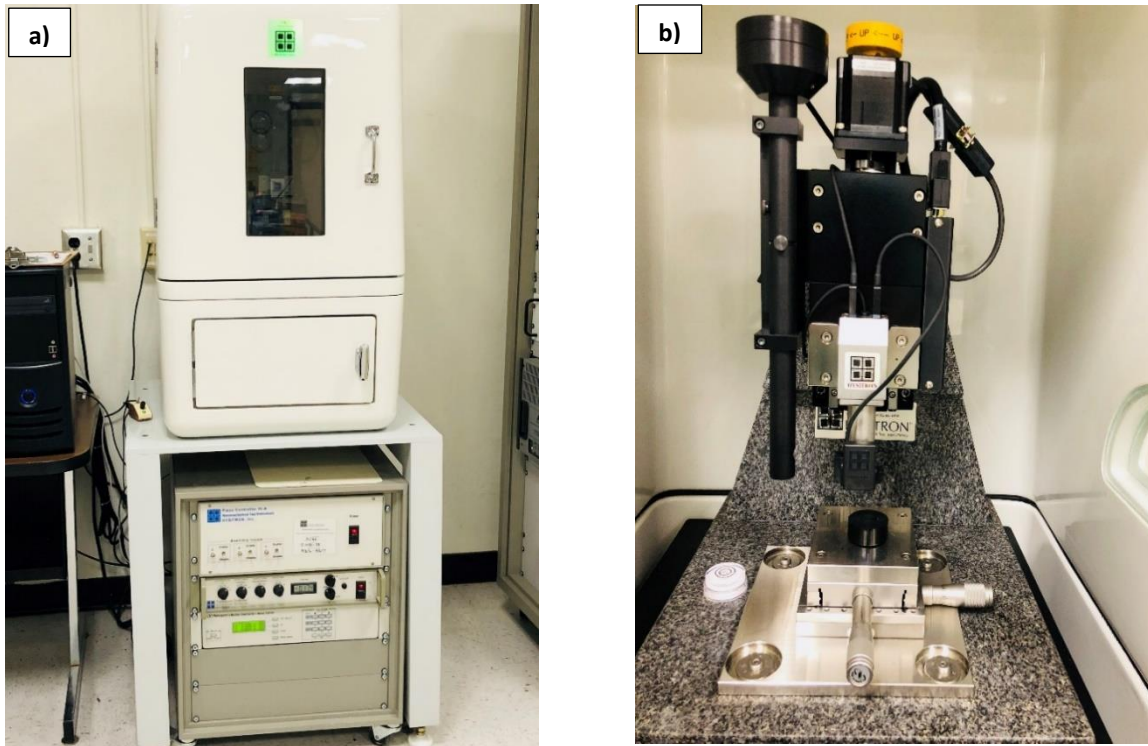


Figure 3-3. a) Nanoindentation machine b) Indentation platform.

Upon microstructural assessments, each sample was re-polished to a very fine level to expel any surface harshness impact. Normally, all genuine metal piece has some level of surface roughness. Usually, the rougher the surface, the more factor gets included in outcomes. Therefore, an appropriate decision of maximum load is required to suit the surface harshness of the testing samples.

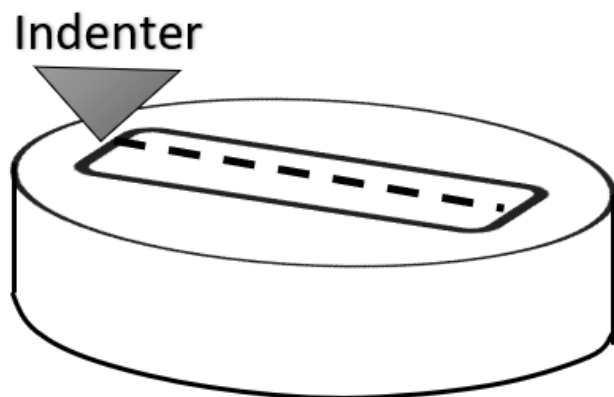


Figure 3-4. Nano indenter set perpendicular to surface of the sample.

The mounted samples (Fig. 3-4) after polishing and etching needs to be positioned on to the XY stage of the instrument.

The Nano-hardness and elastic modulus of deformed samples were examined using a Nano-indentation tester (TI-700 Ubi-1) using a self-similar pyramidal (Berkovich) (Fig. 3-5) indenter at a constant load rate of 1.5 mN/s. The load-controlled indentation tests were done with a peak load of 7.5 mN. The distance between two adjacent indentations was 500 nm across the deformed sample perpendicular to the compression direction to ensure that the deformation by one indentation could not interfere by another.

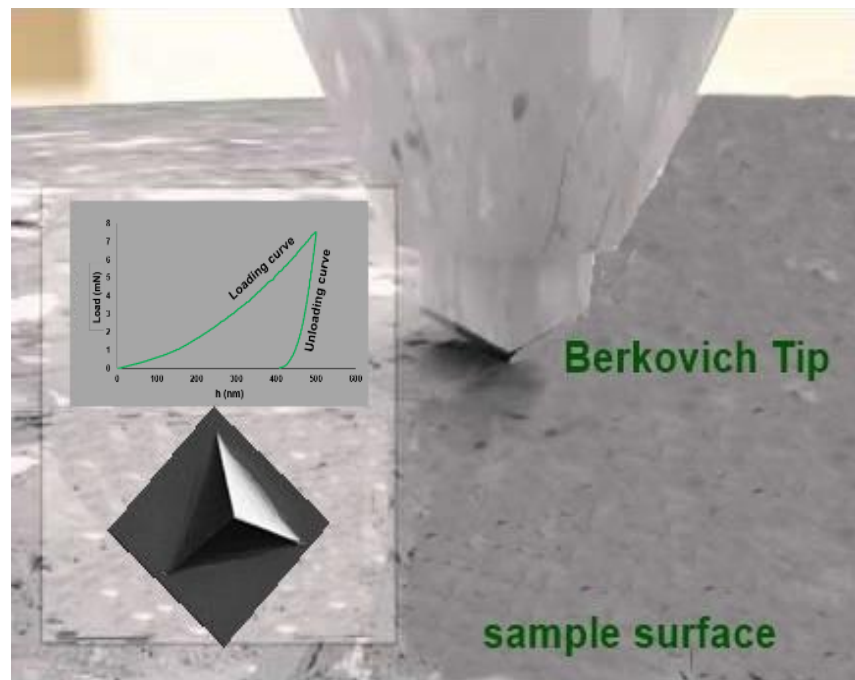


Figure. 3-5. Nanoindentation with Berkovich indenter.

Oxide layers of a few nm form easily on most cases even after fine polishing over metal surfaces within a few microseconds and usually cannot be avoided.

All the indentation tests are done at ambient (room) temperature. The nanoindentation apparatus is a fairly sophisticated instrument and several commercial instrument makers, who employ differing design principles, manufacture it. Preparation of the test surface which is to be probed with the indenter is an extremely important first step, as the final surface finish can exert significant influence on the results obtained. There are two important points to keep in mind here. Firstly, the surface should be as smoothly as possible, because (a) loading should be normal to the surface and (2) the effective contact area is estimated assuming that the surface is flat. Thus, if the amplitude of the

surface roughness is comparable to the contact diameter, indentations at 'valleys' or 'peaks' will result in underestimation or overestimation, respectively, of the true contact area. Secondly, surface preparation should be performed in such a way that possible alteration of the surface in terms of its mechanical properties (due to heat or work hardening generated upon polishing) or chemistry (due to absorption of chemicals in the polishing media, evaporation of elements in the sample, and/or hydration/dehydration) are minimized [25].

3.4. Microstructural Assessment

3.4.1. Optical Microscope

The microstructures were examined by a metallurgical optical microscope (MODEL-MM500T) (Fig 3-6.) after etching. The etchant was composed of 100 mL ethanol, 2.5 gm Picric acid, 25 mL acetic acid, 25 mL water with etching time as long as the 30s for Mg-3.5Li-Al alloy. The other alloy Mg-14Li-Al was etched with a solution of 8% nitric acid and 92% ethanol along with an etching time of 50s.

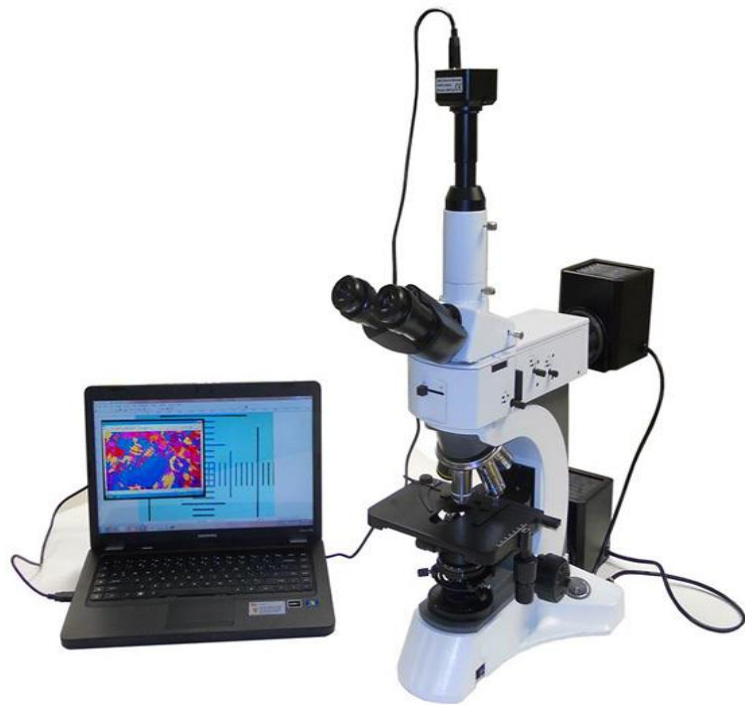


Figure 3-6. Optical Microscope (MODEL-MM500T).

3.4.2. Scanning Electron Microscopy (SEM)

Before observing the samples, they were polished and etched and also before positioning the samples in SEM (MODEL: QUANTA FEG 650) (Fig. 3-7) blower was used, so that no dust can stay over the surface.



Figure 3-7. SEM (MODEL: QUANTA FEG 650).

3.4.3. XRD (X-ray Diffractometer)

XRD measurements were performed by a Rigaku Diffractometer (SmartLab, Rigaku, Japan) (Fig. 3-8) at continuous scan rate of 4° /min, scanning from 20° to 80° .



Figure 3-8. X-ray diffractometer.

CHAPTER IV

4. RESULTS AND DISCUSSION

The resolution of this chapter is to present and confer the experimental results of this study. The results of the experiments contain microstructural characterization, Nanoindentation results and OM, SEM analysis. The chapter is divided into two sections investigation the following alloys:

1. Mg-3.5Li-Al

2. Mg-14Li-Al

4.1. Mg-3.5Li-1Al Alloy

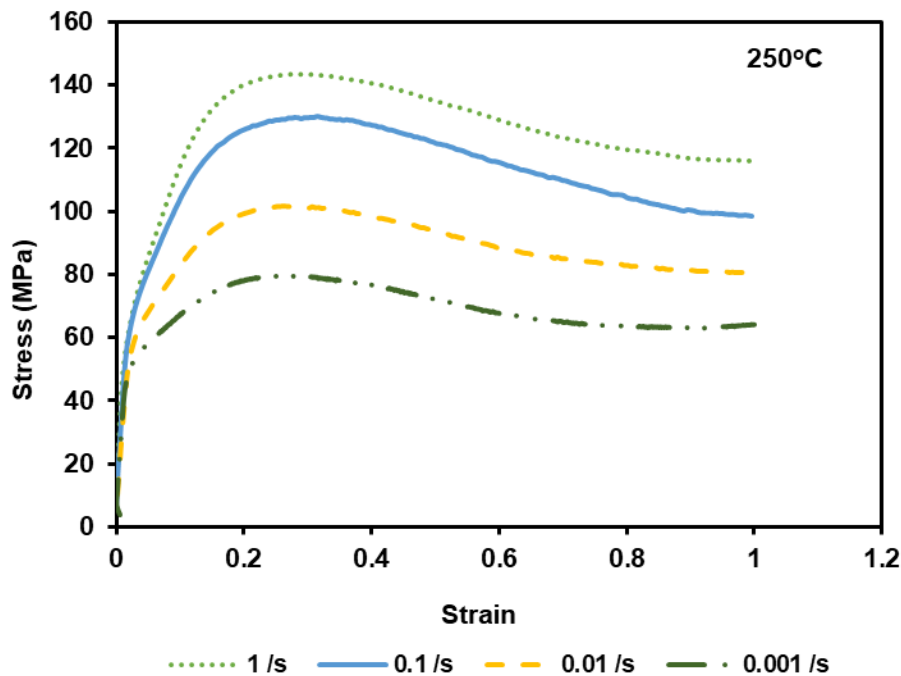
4.1.1. Effect of temperature on flow graphs

Flow curves reflect the microstructural changes at the grain level and the crystal structure. During thermomechanical processing of the studied alloy, several deformation conditions have been observed by analyzing stress-strain curves.

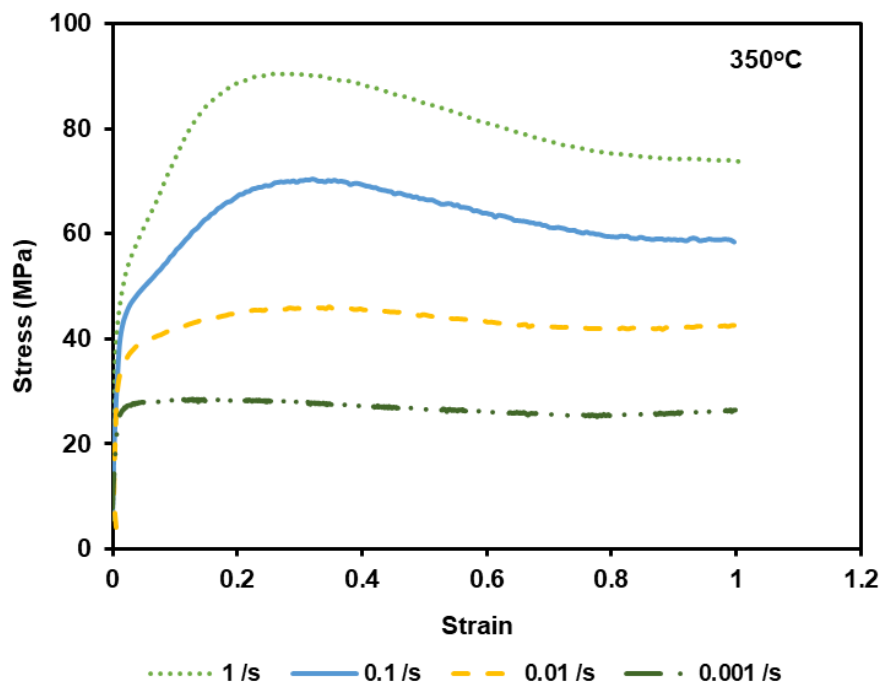
Fig. 4-1 shows that both temperature and strain rate possess considerable effects on the flow stress curves. The flow stress response for all the temperatures and strain rates is that the stress initially increases sharply to a peak value and afterwards decreases gradually to an enduring state as the strain increments. A decline in the stress level is seen with the expansion of deformation temperature and the decline of strain rate.

Effect of thermomechanical processing on this alloy can be expressed step by step. Initially, there is a sharp increase in flow stress, and it is work hardening stage. At the underlying stage of strain, hardening rate is higher than the softening, thus the flow stress rises forcefully, due to the generation and multiplication of dislocations which results in the work hardening effect. Dislocations entangle and multiply, thus dislocation motion gets difficult. Then the dynamic recovery stage begins; thermal energy allows some dislocation motion, and later, the annihilation of dislocation is done by cross slip, climb and dislocation unpinning showing dynamic recovery. However, the temperature of hot working is too frail to even consider overcoming work hardening. As a matter of fact, hardness and ductility are mostly unchanged [45].

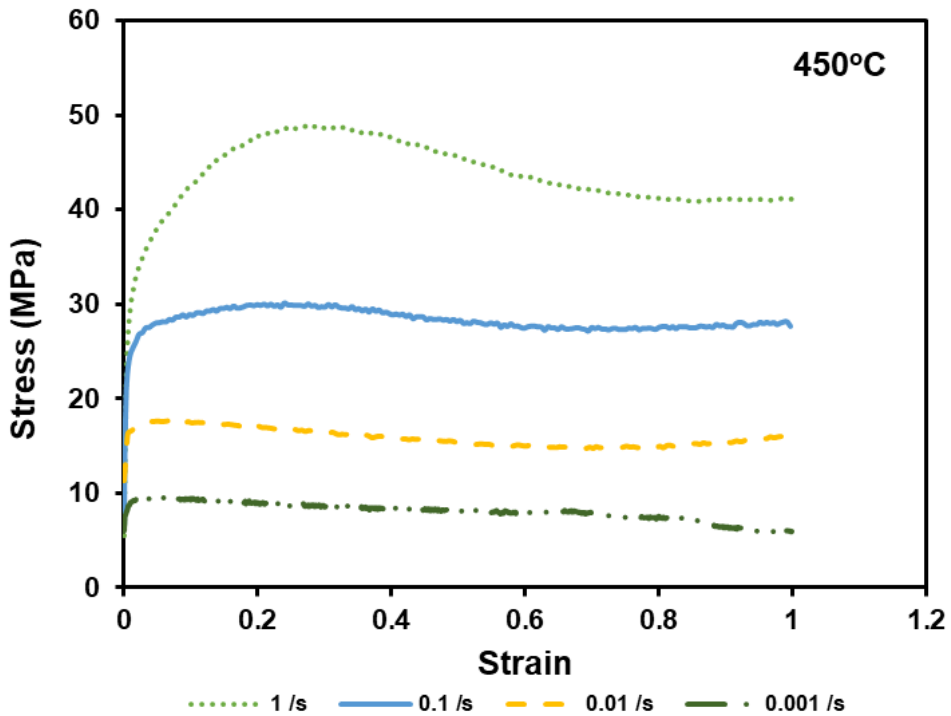
With the increase in temperature (say from 250°C to 350°C) [45], the gradual decrease of work hardening rate occurs inducing another softening mechanism, dynamic recrystallization (DRX). Comparatively, new grains formed having low dislocation density, smaller in size consuming previous cold working history [45].



a



b



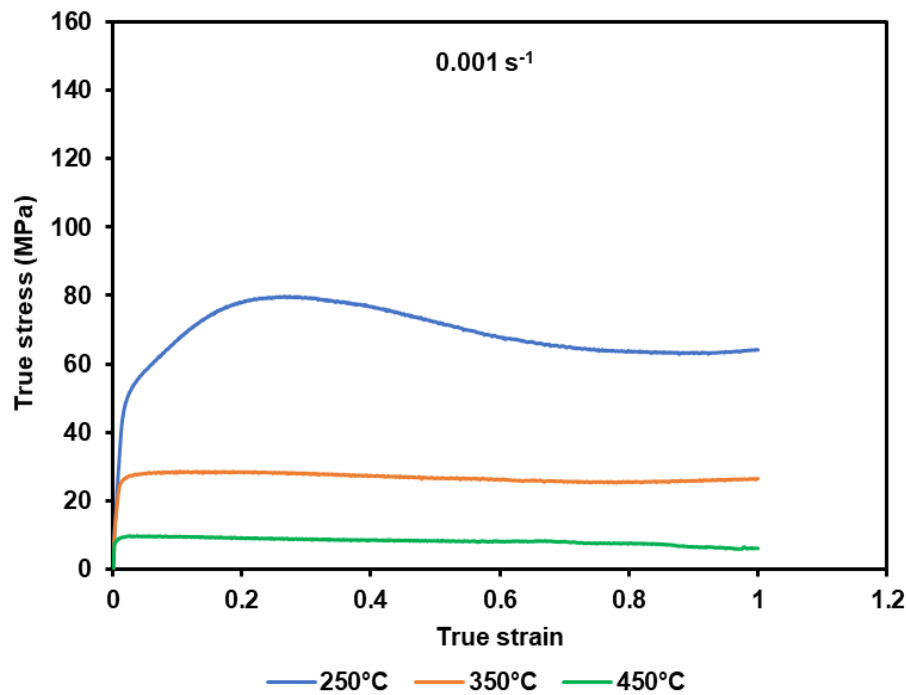
c

Figure 4-1. Flow curves showing dynamic recovery and recrystallization at a) 250°C, b) 350°C, c) 450°C.

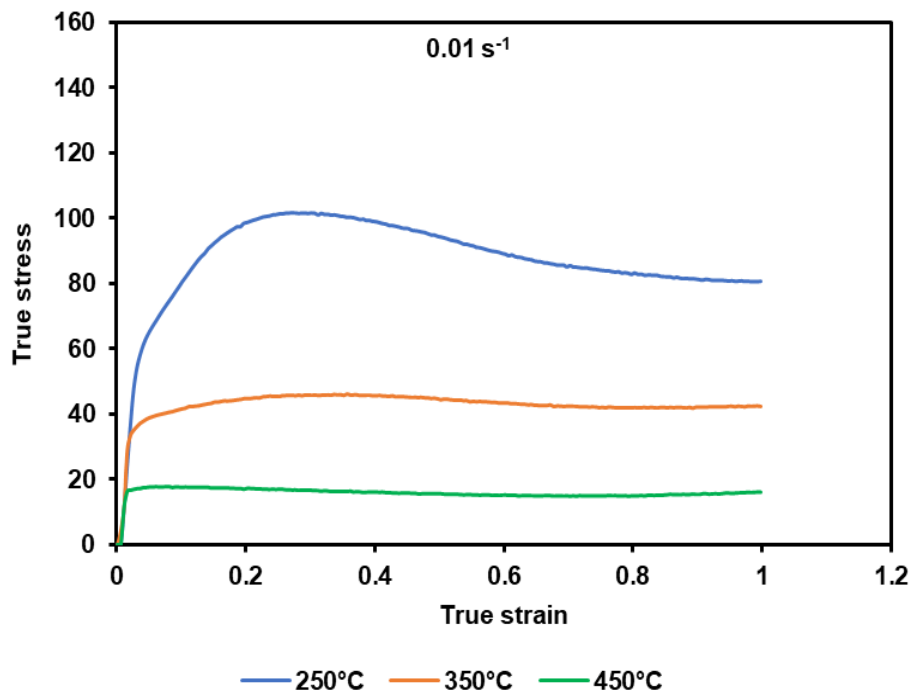
4.1.2. Effect of strain rate on Flow Graphs

The stress-strain curves (Fig. 4-2) are leveled off after attaining the peak stress; this is directly related to a balance which is established between work hardening and softening (dynamic recovery). Dynamic softening (Dynamic Recovery + Dynamic Recrystallization) rate almost equal to work hardening rate; thus, flow stress gradually decreases to a steady stage, because of the prevalent softening mechanism is attained. At the steady state, despite the increase in strain, the flow stress maintains a reasonably constant level. Additionally, at a consistent strain rate, the flow stress diminishes with the expansion of deformation temperature. The dynamic recrystallization that comes

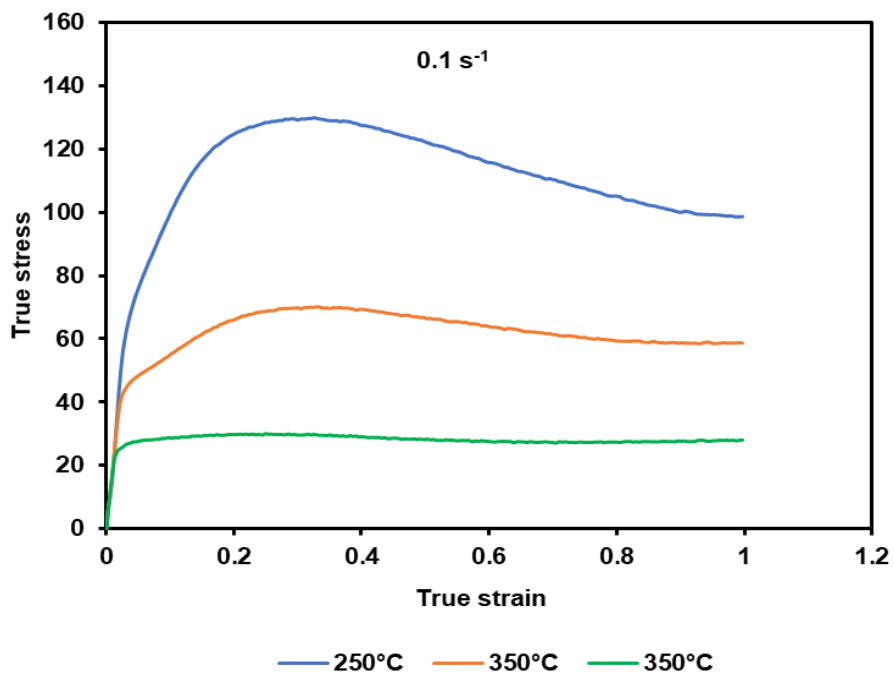
along with an increase in temperature comparatively easier, and afterwards the softening effect is upgraded, which result in a decline of flow stress. Because of steady temperature, with an increase in the strain rate, the dynamic recrystallization cannot be completed; besides, quick augmentation and aggregation of dislocations result in the enhanced flow stress [46].



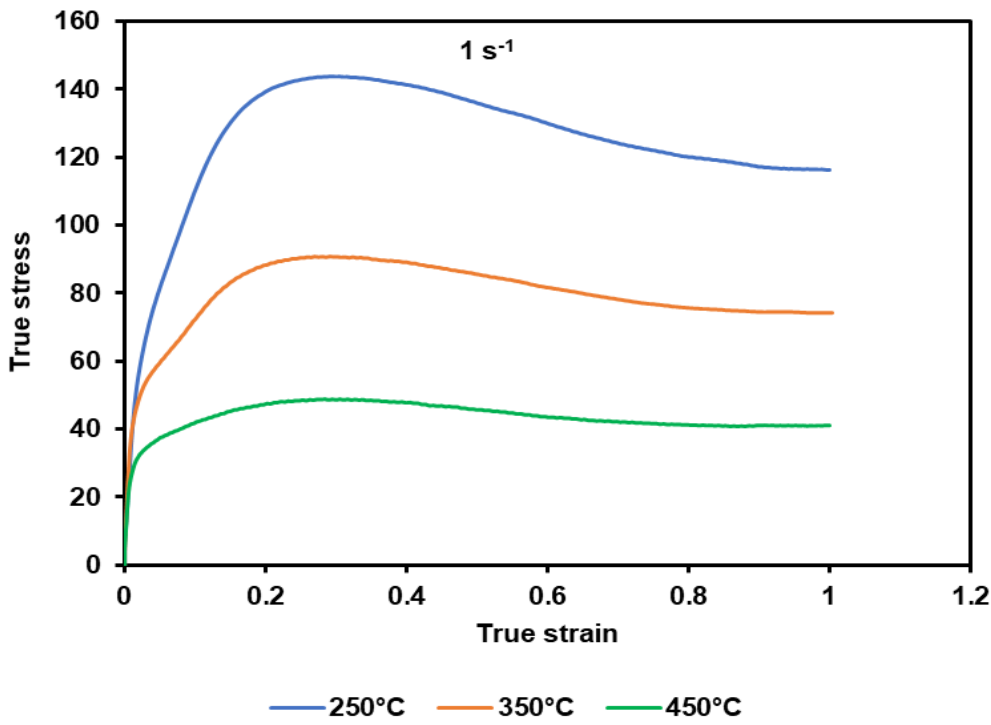
a



b



c



d

Figure 4-2. True stress-strain curves for Mg-3.5Li-Al alloy during compression at a) 0.001 s^{-1} , b) 0.01 s^{-1} , c) 0.1s^{-1} , d) 1 s^{-1} .

4.1.3. Microstructure

The microstructure evolution of the Mg alloy for different temperatures and strain rates is analyzed through optical microscopy. Fig. 4-3 shows initial single-phase microstructure of the alloy which is a single phase (α -Mg) with HCP structure and containing equiaxed grains. The uniform grain size is around $70\text{ }\mu\text{m}$. As there is no evidence of any second phase, the α -Mg phase is the only constituent for this alloy. Also, some twin bands are easily visible in the initial microstructure. Some precipitates containing Al in Mg alloys (MgLiAl_2) are visible mostly near the grain boundaries. Very

few are found inside the grains. Twins are observed inside the grains comparatively at a low temperature of deformation and strain rates, probably generated at the time of sample preparation [47].

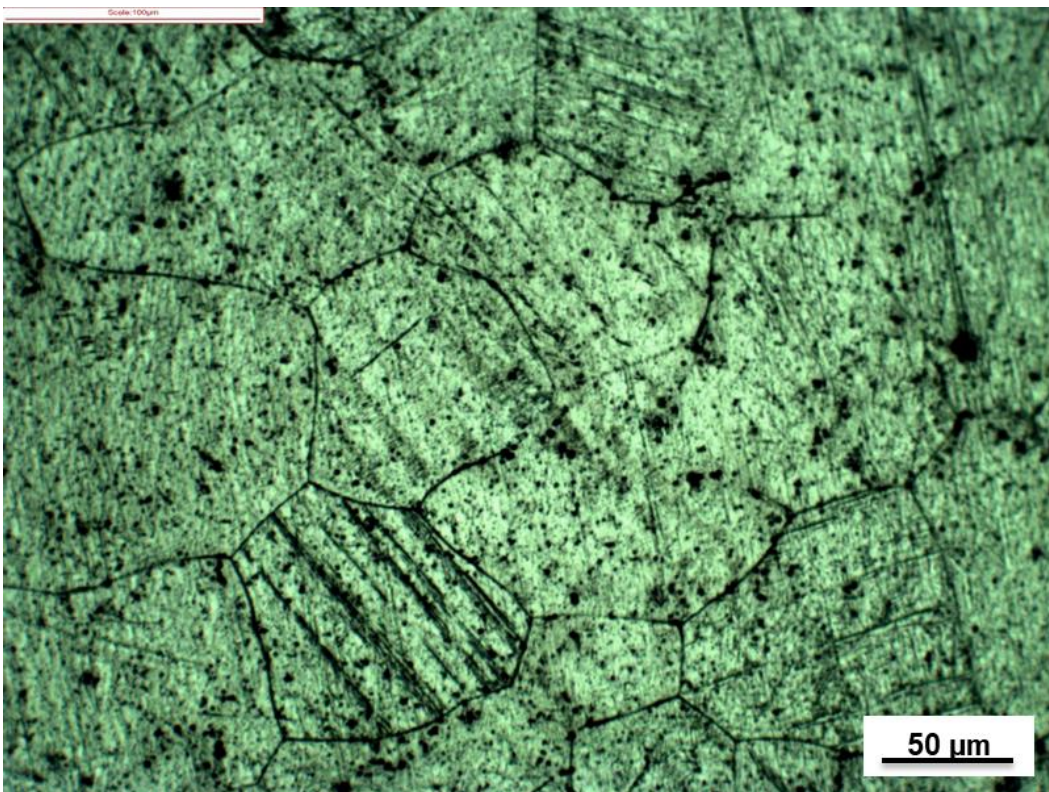


Figure 4-3. Initial microstructure of the Mg-3.5Li-1Al alloy.

From Fig. 4-4, changes in microstructures for the deformed samples are detectable satisfactorily. It is apparent that with enhancing the deformation temperature and strain rate new grains appeared through recrystallization and replaced old grains. The gradual change for all the temperatures and strain rates needed to be described explicitly.

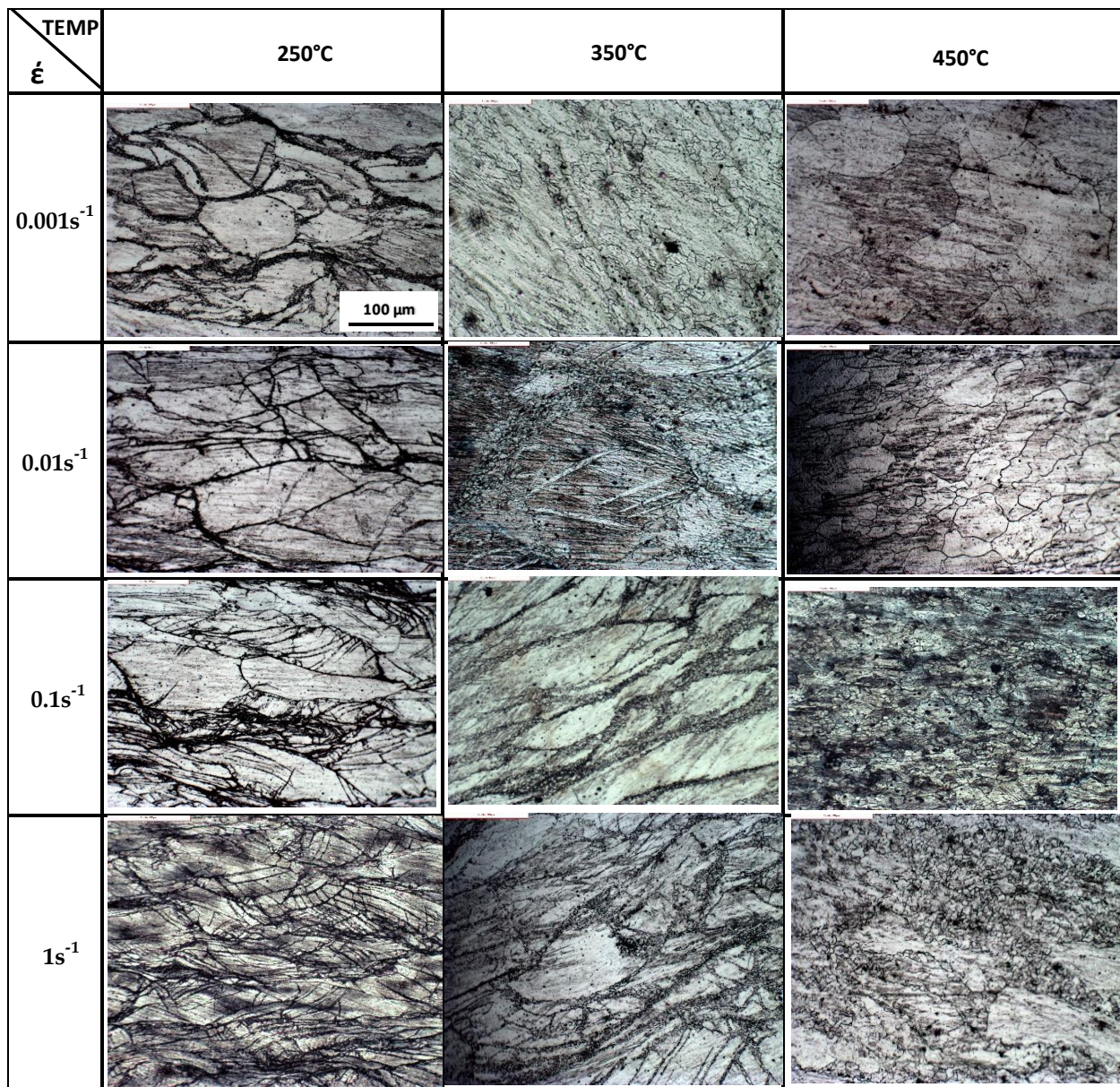


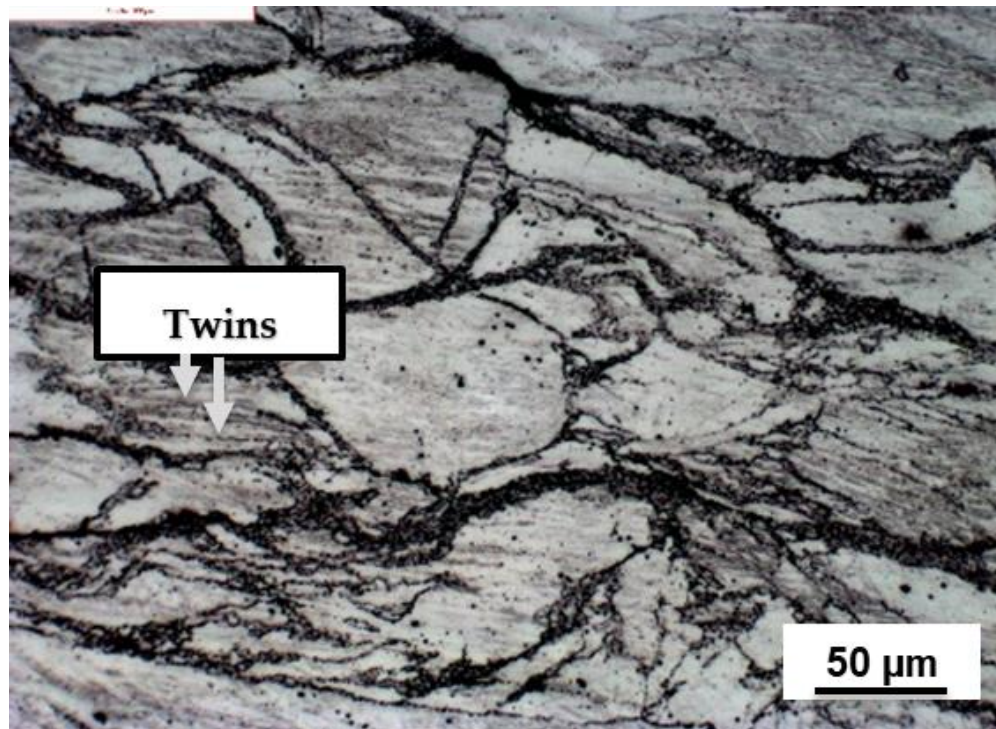
Figure 4-4. Microstructures of the thermomechanically processed Mg-3.5wt%Li-Al alloy at different temperatures 250°C, 350°C, and 450°C and strain rates of 1, 0.1, 0.01, and 0.001 /s.

Fig. 4-5a shows the occurrence of partial recrystallization or incomplete recrystallization comparatively at the low temperature of 250°C and strain rate of 0.001/s. Also, in the tested Mg-Li-Al alloy, deformation twinning is observed in the α -Mg phase in the

deformed material. Fig. 4-5b contains comparatively small grains indicating that complete recrystallization occurred during hot compression. At this temperature, twinning dominates the deformation. Consequently, high density of twins can be distinguished. In the meantime, fine “necklace” grains encompassing the subgrains nucleate and develop altogether, coalesce and consume the greater part of the grains. The dynamically recrystallized necklace grains are sandwiched between the encroached twins. New grains may likewise nucleate inside the twins and develop dividing the large twins into unpredictable islands. As such, high thickness twins can be viewed. Subsequently, new grains show up, and a necklace like structure is shaped through the dynamic recrystallization. The hot-compression temperature is 450°C, which is much higher than the low recrystallization temperature (Fig. 4-5c). Comparatively, large recrystallized grains formed because of hot working at 450°C and 0.01 /s strain rate. The DRX grain size expanded with expanding temperature and diminishing strain rate. Also, during processing at 450°C and 0.01 /s the low angle subgrain boundaries were gradually changed into the high angle grain boundaries by diminishing the dislocation density.

The density of recrystallizing grains increases with expanding temperature and strain rate (Fig. 4-5d). Due to elevated thermal activation with the high temperature of deformation, nucleation rate of recrystallization and the growing rate of grains increased. Microstructures demonstrate that the recrystallization was taken completely,

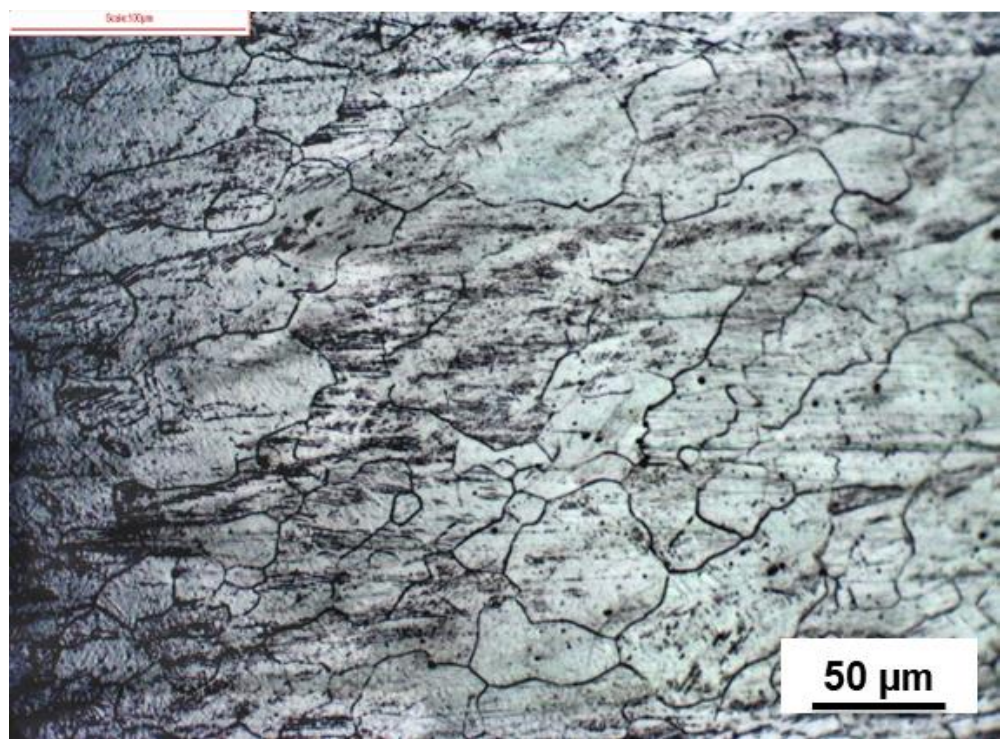
and the grains were supplanted by the recrystallization on the cross-area of the specimen. It is notable that the Mg-3.5Li-Al resulted in finer grains at 450°C and strain rate of 1 /s. The DRX grains expanded with rising the temperature and diminishing the strain rate. Partial recrystallization happened in alloys at every deformation condition, even at the peak temperature of 450°C and the bottom strain rate of 0.001 /s.



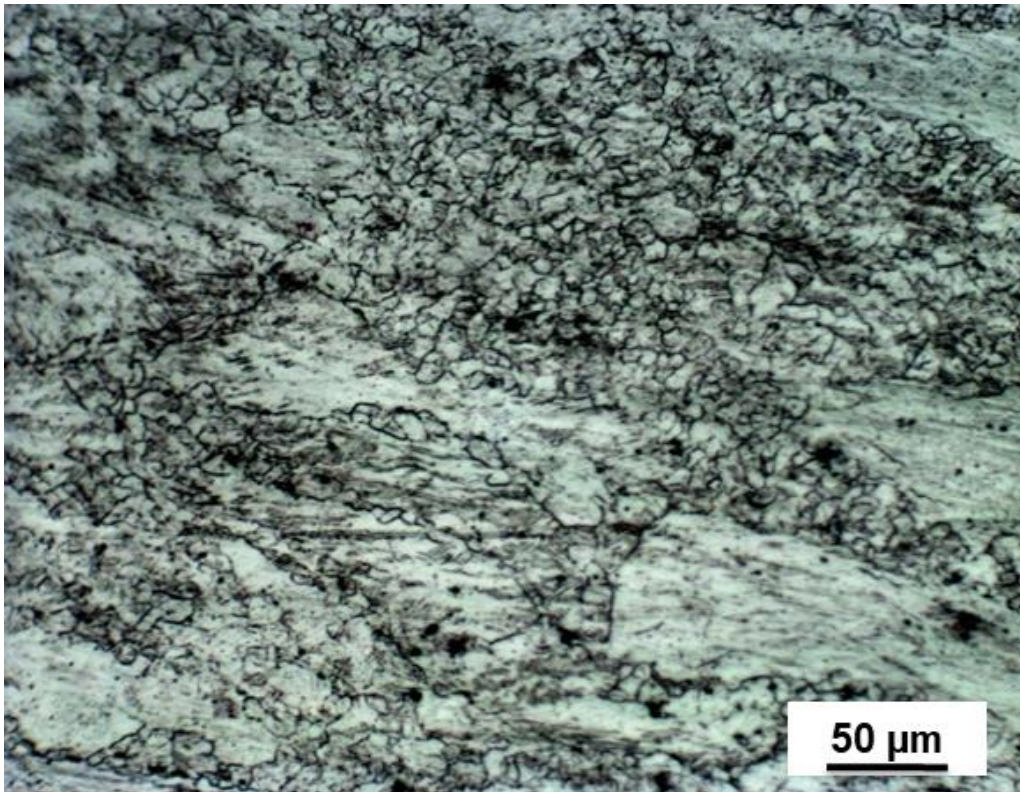
a



b



c



d

Figure 4-5. a) 250 °C 0.001/s evidence of twins at this deformation stage, b) 350 °C 0.1/s chains of recrystallized grains, necklace like structure, c) 450 °C 0.01/s recrystallized structure, d) 450 °C 1/s recrystallized structure.

4.1.4. Indentation load/displacement

The typical load-displacement graph observed at room temperature has been shown in Fig. 4-7. The loading curve represents a stair step like behavior with the increase of strain for all temperatures and strain rates. Though, the same kind of serration was observed for as received alloy demonstrated in Fig. 4-6. Comparing Fig. 4-6 and Fig. 4-7 the serration effect becomes more pronounced in the thermomechanically processed samples. These serrations are widely known as Portevin Le Chatlier effect (PLC),

resulting from the interaction between the Mg solutes and the mobile dislocations. For as received alloy, dislocations form during fabrication. However, the TMP samples are plastically deformed at high temperature and strain rates, the stress results from that process give rise to the number of dislocations during their forming process. Thus, giving rise to the serrated flow for all the TMP samples.

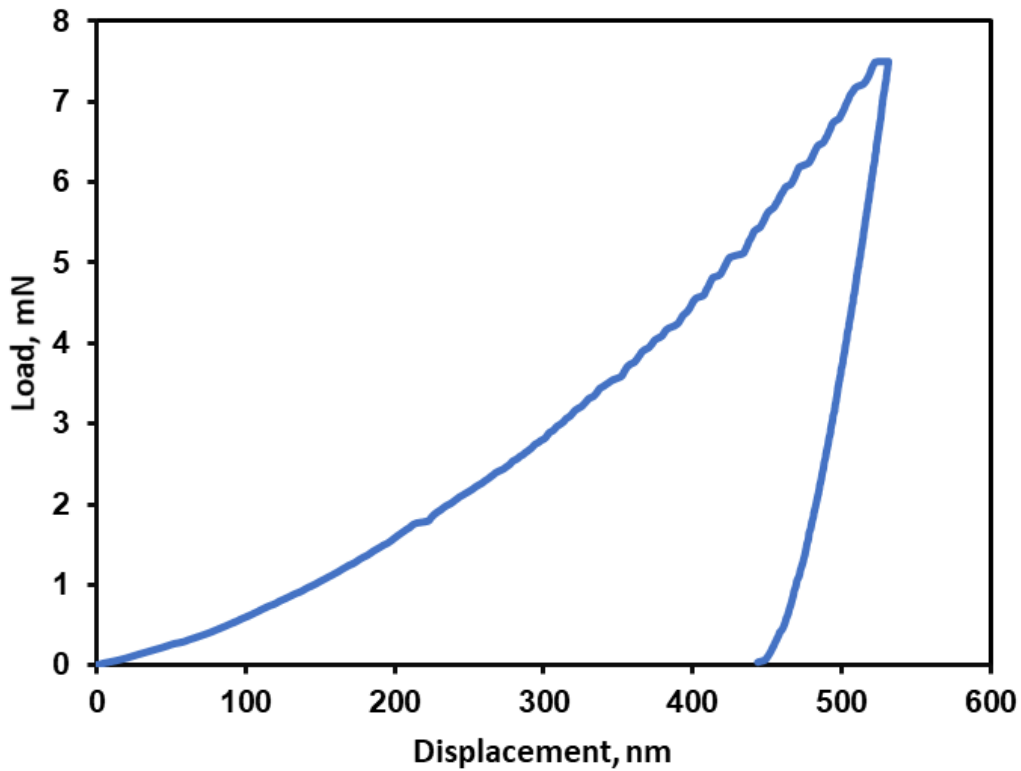


Figure 4-6. Nanoindentation results for as received alloy.

From the nanoindentation results, it was observed that the hardness and the elastic modulus are increased for all the TMP samples compared to the as-received sample. The hardness (H) and elastic modulus (E) values are presented in Table 1. As observed in Table 1, the as-received alloy possesses low hardness and elastic modulus compared

to the thermomechanically processed samples. This can be attributed to the grain refinement in the TMPed samples.

The hardness and elastic modulus comparison among the TMP samples show downward trend with increasing the deformation temperature (Table 4-1). This is attributed to a decrease in the work hardening rate as well as grain growth and coarsening of the precipitates/microstructural phases.

Table 4-1. Hardness and elastic modulus of Mg-3.5Li-Al alloy (for 1/s strain rate).

Material Condition	E (GPa)	H (GPa)
As received alloy	48 ± 2.5	1.01 ± 0.02
After TMP	250°C	82 ± 4.5
	350°C	61 ± 3.1
	450°C	57 ± 3.7

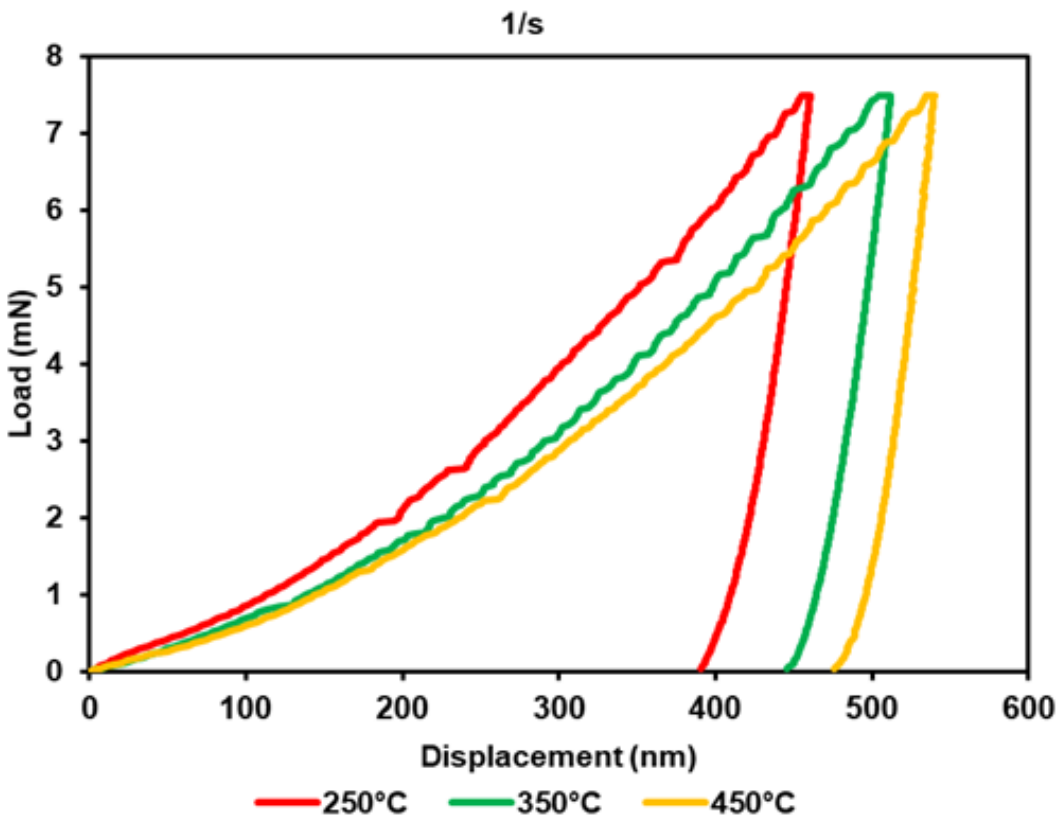


Figure 4-7. Nanoindentation results for samples deformed at the constant strain rate of 1/s.

Most importantly, the PLC effect is evident in all the samples at room temperature from nanoindentation results. Plastic deformation happens inhomogeneously on the microscopic level because of thermally initiated dislocation motion through numerous sorts of obstacles [48]. This kind of plastic instability occurs in a solid solution because of the repetitive locking of dislocations by solute atoms and unlocking of dislocations [49]. Therefore, the need for understanding and controlling the mechanisms underlying the PLC effect seems necessary in the studied Mg-Li alloy.

Macroscopically, due to the PLC effect, polished surfaces of the examined samples will become rippled and the overall plasticity will be diminished significantly [50]. One point that requires great consideration is that the PLC effect for the most part happens in the face-centered cubic (FCC) alloys and is only occasionally revealed in the hexagonal close-packed (HCP) alloys [51].

From the phase diagram it is clear that Mg-3.5Li-Al is a solid solution alloy. Serrations on load-displacement curves are usually explained in term of Dynamic Strain Ageing (DSA) mechanism. However, there might be a few other physical processes [52] which yield serrated flow curves. Among those, twinning and thermomechanical instabilities are of importance because of the nanoindentation. Twins are one type of obstacles; in hcp alloys twins represent an important role in plastic deformation.

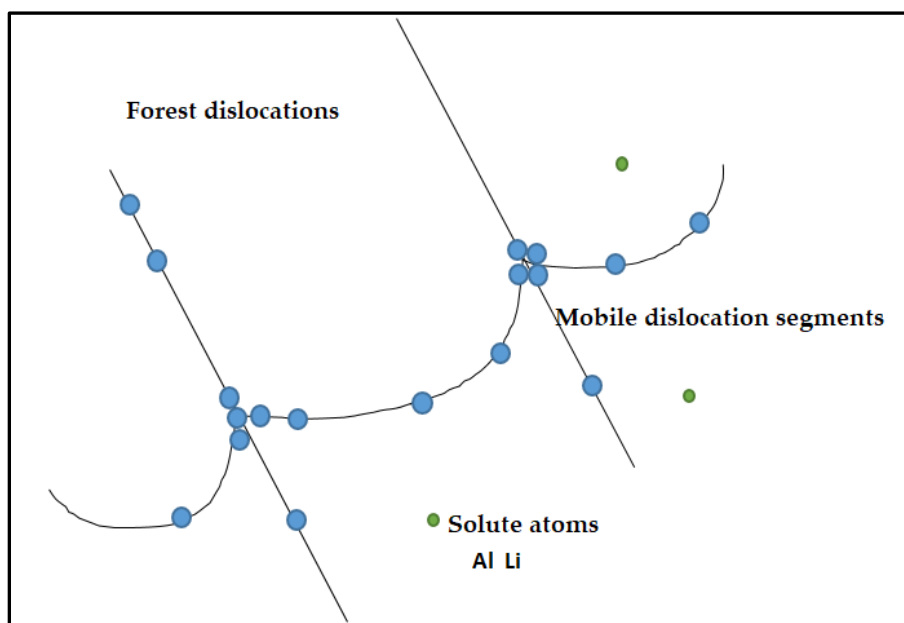


Figure 4-8. Schematic of dynamic strain aging (DSA) causing PLC effect [12].

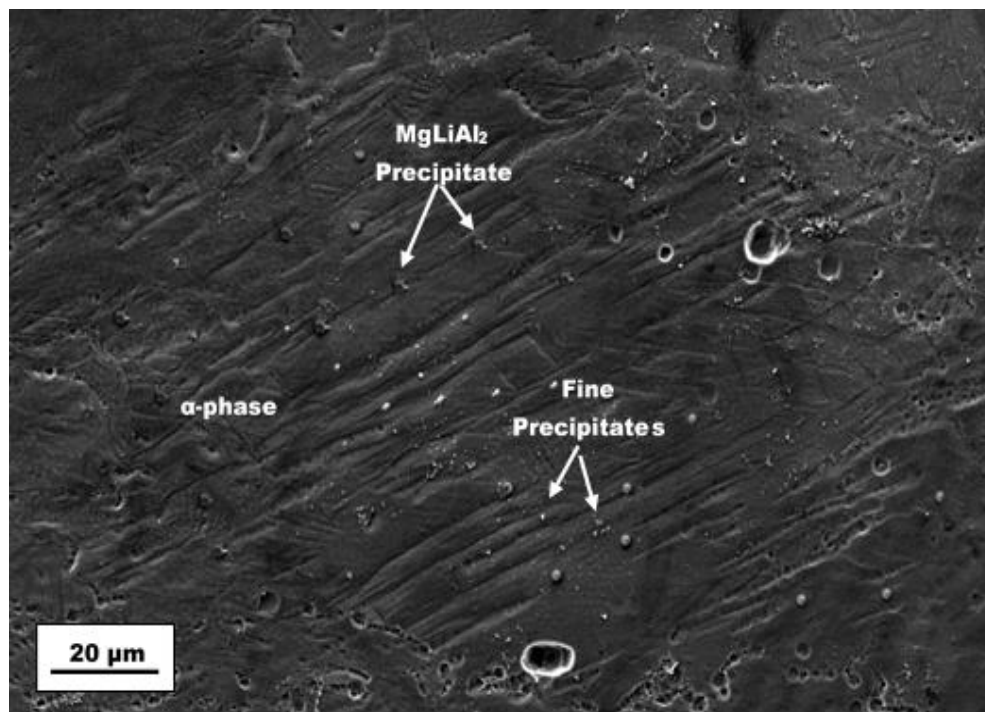


Figure 4-9. SEM microstructure of Mg-3.5Li-Al alloy (deformation temperature 350 °C and strain rate of 0.1/s) the precipitates.

Also, when dislocations density equals the solute atoms density; solutes start creating obstacles for mobile dislocations; forming forest dislocations [51] Fig. 4-8. Besides, the dislocation forming process is aided by a double cross slip mechanism. The forest dislocations in non-basal slip system (prismatic slip) are formulated by double cross slip mechanism of basal dislocations by means of prismatic planes. Due to the addition of the Li in Mg, the value of both c and a lattice parameter is reduced in Mg-Li solid solution and prismatic slip system is activated easily. Thus, the interaction between the basal slip plane and prismatic slip plane is quite easy in this alloy causing double slipping mechanism which results in the formation of forest dislocations [53]. Small

segments of forest dislocations formed through this process increase in density with strain [54]. And these forest dislocations act as obstacles for moving dislocations.

The PLC effect is the visible flow pattern that is related with the phenomenon of dynamic strain aging (DSA). This happens as flow instability is developed in a deformed alloy under explicit conditions, such as medium strain rate, elevated temperatures and the presence of solutes and interaction between the solutes and the dislocations [55]. In particular, during nanoindentation testing, the reason behind the DSA is the loading rate, the composition of the alloy and for a few materials, the orientation of the grains concerning the direction of the indentation [56].

Results and studies show that the main obstacles for the motion of dislocations particularly for this alloy are MgLiAl_2 precipitates and solute atoms (Fig. 4-9) [57]. During the nanoindentation, dislocations start moving and particularly mobile dislocations are hindered by the solute atoms, causing material hardening. That is because; dissolved solutes (Li and Al atoms) migrate towards the dislocations. These small atoms lower the dislocation strain energy. Then it requires more external energy in the form of stress to move the dislocation. The total dislocation density increases with increasing the strain while the number of free solute atoms is constant. Thus, dislocation-solute interactions reduced with increasing strain and mobile dislocations are released. Therefore, the load needed for deformation decreases which can be observed in the load-displacement curve as a serration [51]. The stress level increment

depends on strain value during the indentation for all TMP samples. Therefore, it is obvious that the PLC effect is dominant in the Mg-3.5wt%Li-Al alloy at room temperature.

4.1.5. Constitutive equation of Mg-3.5Li-Al alloy from flow stress-strain behavior

To understand the high-temperature plastic deformation behavior, it is required to investigate the constitutive characteristics of Mg-3.5Li-Al alloy. To figure out the material parameters necessary for constitutive equations, the hot compression flow stress-strain curves of the alloy with strain rates of 1, 0.1, 0.01, 0.001 /s and temperature range of 250°C, 350°C, and 450°C are shown in Fig. 4-2. The variety of peak stress of the test alloy under different hot compression testing conditions is visible on the graphs (Fig. 4-10). Under all the testing conditions the impact of deformation temperature and strain rate on the flow stress is remarkable. Strain rate and deformation temperature have significant impacts on the deformation behavior of the tested alloy; for instance, the flow stress diminishes with expanding deformation temperature at a certain strain rate and increments with the expansion of strain rate at a given temperature.

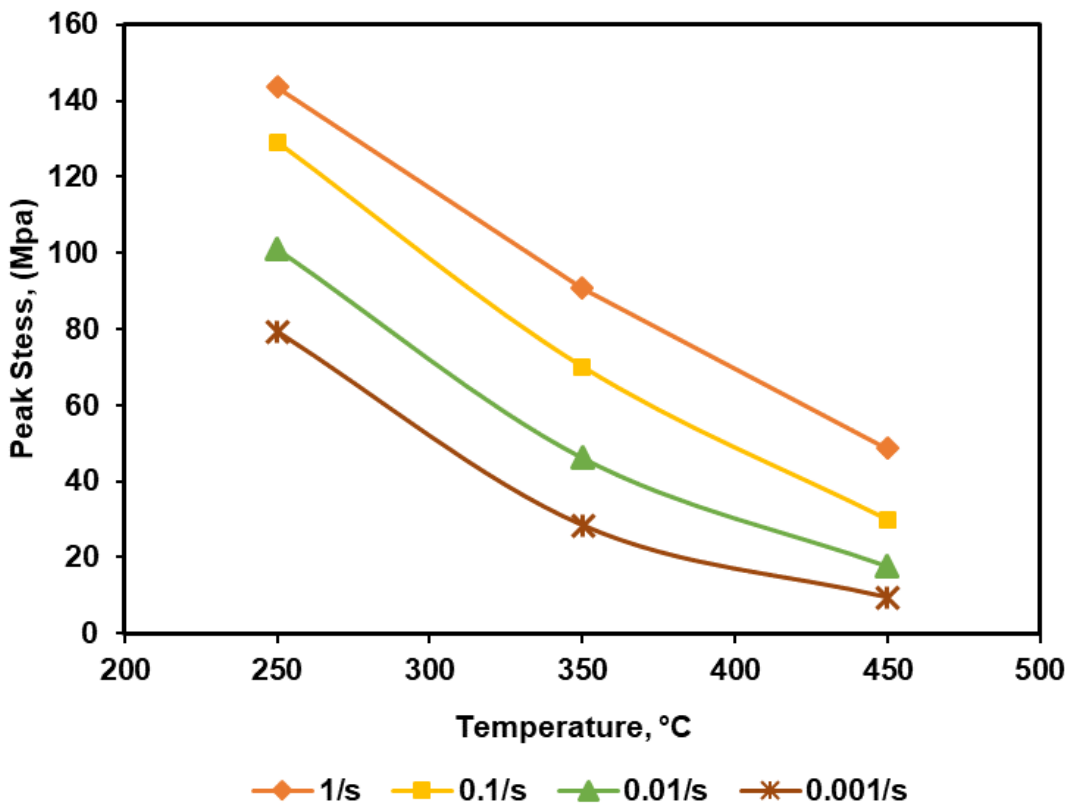


Figure 4-10. Peak stress for different strain rates.

Considering the deformation temperature (T), strain (ε), strain rate ($\dot{\varepsilon}$) & the true stress-strain curves the value of compressive flow stress is determined. Therefore, flow stress can be written as [58]:

$$\sigma = \sigma(T, \varepsilon, \dot{\varepsilon}) \quad (4-1)$$

The relation between temperatures (T), strain (ε), and strain rate ($\dot{\varepsilon}$) at different stress levels can be expressed using the following equations:

$$\dot{\varepsilon} = A\sigma^m \exp\left(-\frac{Q}{RT}\right) \quad (4-2)$$

$$\dot{\epsilon} = A \exp(\beta\sigma) \exp\left(-\frac{Q}{RT}\right) \quad (4-3)$$

$$\dot{\epsilon} = A [\sinh(\alpha\sigma)]^n \exp\left(-\frac{Q}{RT}\right) \quad (4-4)$$

where, Q is the activation energy for hot deformation (KJ/mol), R is the ideal gas constant (8.314 J/ (mol.K)), T is the absolute temperature (K), σ is the flow stress (MPa) at a given strain, A , n , α , and β are temperature independent materials constants, where $\alpha = \beta/n_1$, A is hyperbolic sine constant, n is hyperbolic sine power, and α is the stress multiplier.

Eqs. 4-2 & 4-3 are valid for low stresses when $\alpha\sigma < 0.8$, and for high-stress level $\alpha\sigma > 1.2$, respectively. Eq. 4-4 is applicable to all stress levels.

By taking the natural logarithm of equation 2, 3, and 4 one can find that [59, 53]:

$$\ln\dot{\epsilon} = \ln A + m \ln \sigma - \frac{Q}{RT} \quad (4-5)$$

$$\ln\dot{\epsilon} = \ln A + \beta \sigma - \frac{Q}{RT} \quad (4-6)$$

$$\ln\dot{\epsilon} = \ln A - \frac{Q}{RT} + n \ln[\sinh(\alpha\sigma)] \quad (4-7)$$

From Eqs. 4-6 & 4-7 the relation between $\ln\dot{\epsilon}$ - σ and between $\ln\dot{\epsilon}$ - $\ln\sigma$ are found by utilizing flow stress data under various temperatures and strain rates under a definite deformation condition (e.g. $\dot{\epsilon} = 0.2$) plotted Figs. 4-11 & 4-12. The slope of linear relationship fitting graphs would be n_1 and β .

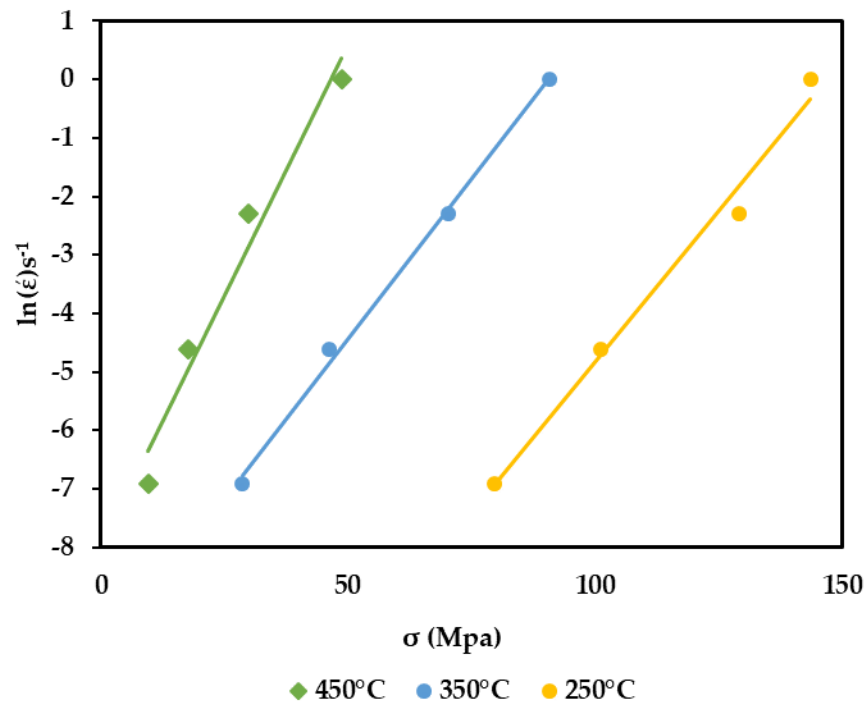


Figure 4-11. $\ln\dot{\epsilon}$ – σ relation curve, symbols show the experimental data and solid lines represent best linear fit.

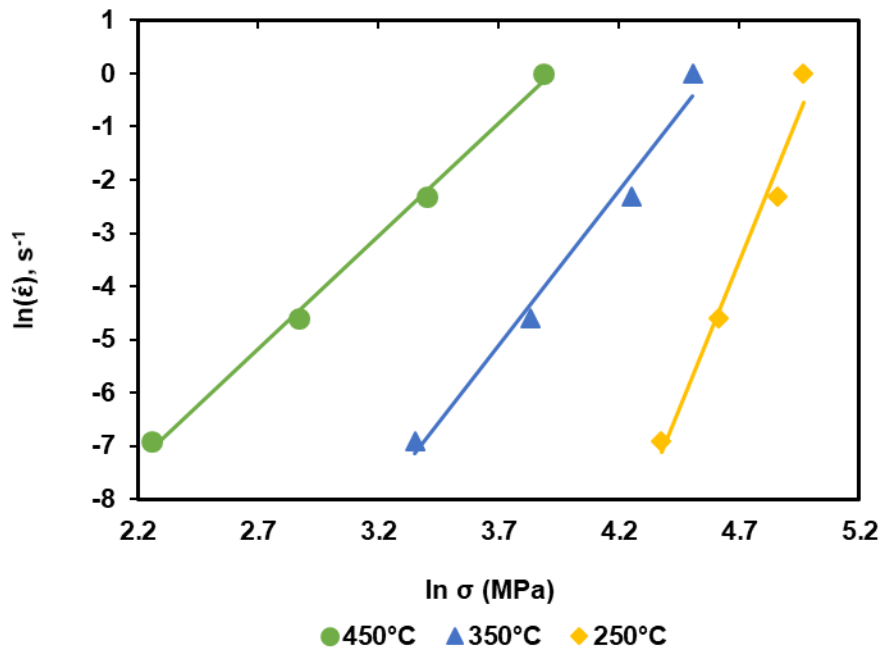


Figure 4-12. $\ln\dot{\epsilon}$ – $\ln\sigma$ relation curve, symbols show the experimental data and solid lines represent best linear fit.

4.1.6. Constitutive analyzing using the Zener-Hollomon model

Zener Hollomon (Z) parameter is commonly utilized to depict both the effects of strain rate and temperature on the hot deformation behavior of materials. The equation for Z parameter can be written as:

$$Z = \epsilon \cdot \exp\left(\frac{Q}{RT}\right) = A[\sinh(\alpha\sigma)]^n \quad (4-8)$$

Activation energy can be found by differentiating equation 8:

$$Q = R \left\{ \frac{\partial \ln \epsilon}{\partial \ln [\sinh(\alpha\sigma)]} \right\} \left\{ \frac{\partial \ln [\sinh(\alpha\sigma)]}{\partial 1000/T} \right\} \quad (4-9)$$

The slopes of the lines are derived with a certain strain ($\epsilon = 0.2$). Considering the mean value of the slopes, $n= Q_1 = 4.63$, $Q_2 = \left\{ \frac{\partial \ln [\sinh(\alpha\sigma)]}{\partial 1000/T} \right\}$ is achieved from the slope of the curve $\ln[\sinh(\alpha\sigma)] - 1000/T$ in a certain strain [53] from Fig. 4-13 & 4-14. The value of $\ln[\sinh(\alpha\sigma)]$ is calculated utilizing the experimental stress data and α under different temperature and strain rate. The mean value of slopes gives $Q_2= 4.12$.

The value of $\ln A - Q/RT$ would be average intercept of the fitted curve. Therefore, $\ln A = 36.5$, and $\alpha = 0.018$. In the constitutive equation, the effect of strain is explained by expecting that the material constants (α , n , Q and $\ln A$) are a polynomial function of strains. The values have repeated calculations using data for different strains, $\epsilon = 0.2$, 0.25, 0.3, 0.35, 0.4.

Zener Hollomon equation can be expressed as [53]:

$$\sigma = \frac{1}{\alpha} \ln \left\{ \left(\frac{Z}{A} \right)^{\frac{1}{n}} + \left[\left(\frac{Z}{A} \right)^{\frac{2}{n}} + 1 \right]^{\frac{1}{2}} \right\} \quad (4-10)$$

$$\sigma = \frac{1}{\alpha} \ln \left\{ \left(\frac{\varepsilon \cdot \exp\left(\frac{Q}{RT}\right)}{A} \right)^{\frac{1}{n}} + \left[\left(\frac{\varepsilon \cdot \exp\left(\frac{Q}{RT}\right)}{A} \right)^{\frac{2}{n}} + 1 \right]^{\frac{1}{2}} \right\} \quad (4-11)$$

Substituting the values of (α , n , Q and $\ln A$) in Eq. 4-11, we get the flow stress at elevated temperature.

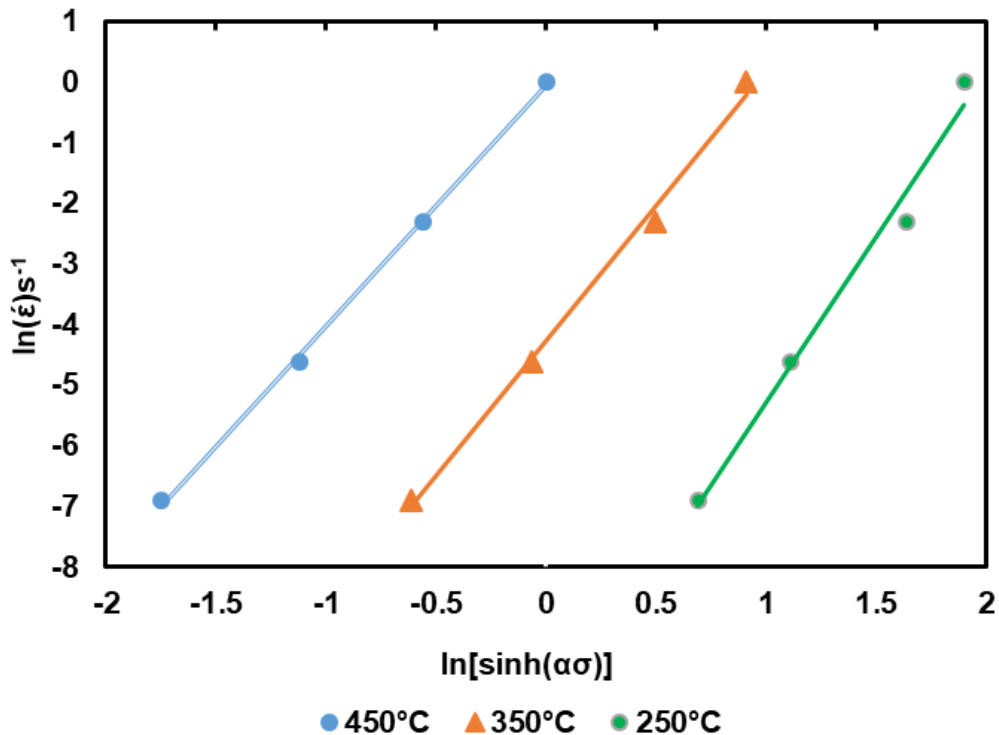


Figure 4-13. $\ln\dot{\varepsilon}$ - $\ln[\sinh(\alpha\sigma)]$ relation curve, symbols show the experimental data and solid lines represent best linear fit.

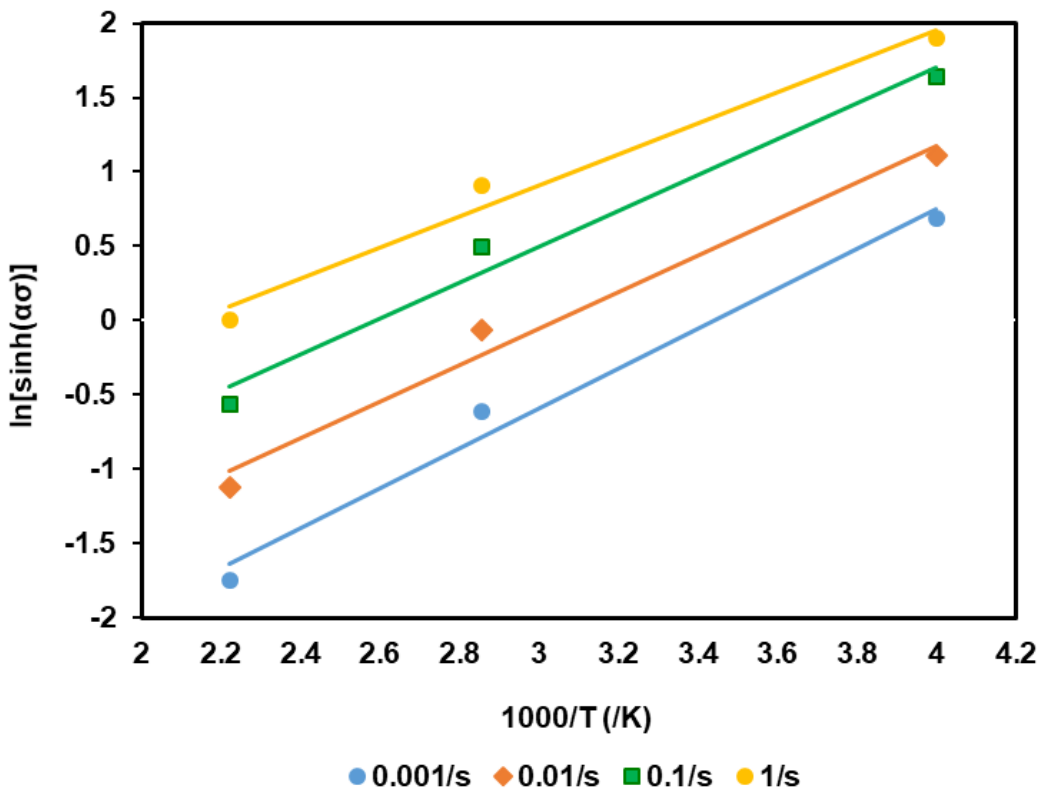


Figure 4-14. $\ln\dot{\epsilon}$ - $\ln[\sinh(\alpha\sigma)]$ relation curve symbols show the experimental data and solid lines represent best linear fit.

Fig. 4-15 represents the calculated stress-strain graph (particularly shown for 450 °C and 1/s as testing sample) to verify the effectiveness of the Zener Hollomon method. The plotted graph confirms that the calculated values are like the measured values.

Fig. 4-16 demonstrates a correlation between the determined peak stresses dependent on hyperbolic-sine function and the deliberate peak stresses. The outcomes show that the computed stresses are reliable with the measured stresses, displaying that hyperbolic-sine function can depict the hot deformation process precisely. Along these lines, the hyperbolic-sine function is resolved as the constitutive condition for the tested

Mg-Li-Al alloy; as proposed deformation constitutive equation gives an exact and precise estimate of the flow stress for this alloy, and can be utilized to examine the issues amid forming and casting process.

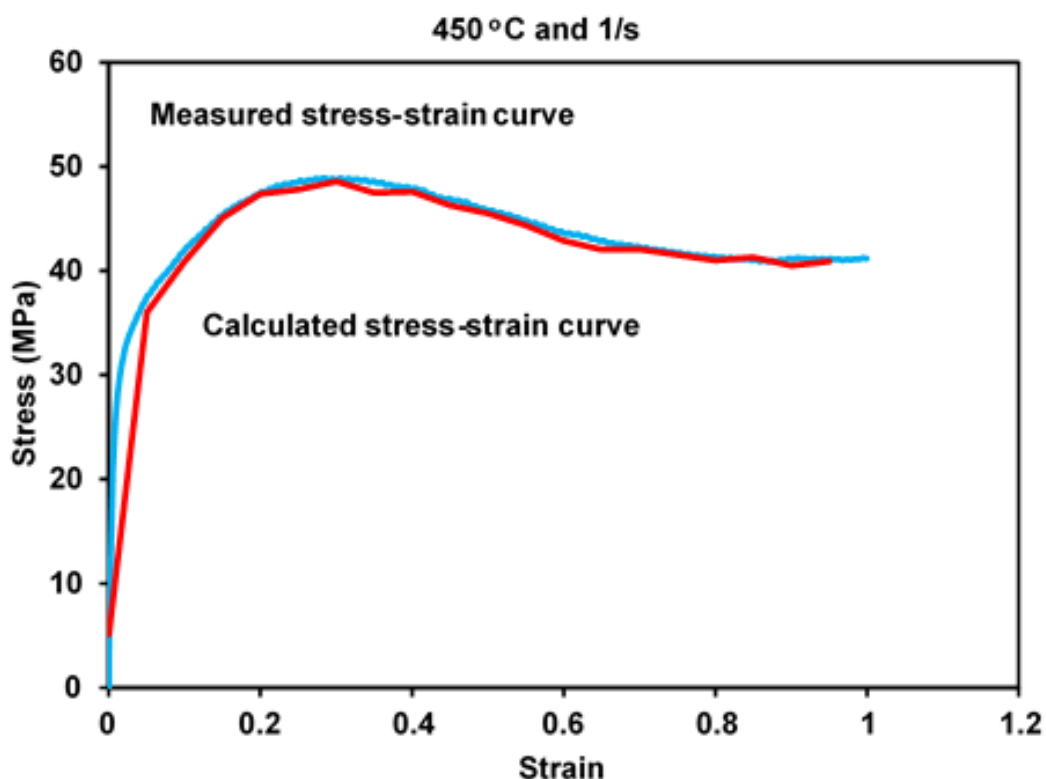


Figure 4-15. Comparison between the measured and the calculated stress-strain graph for 450 °C and 1/s.

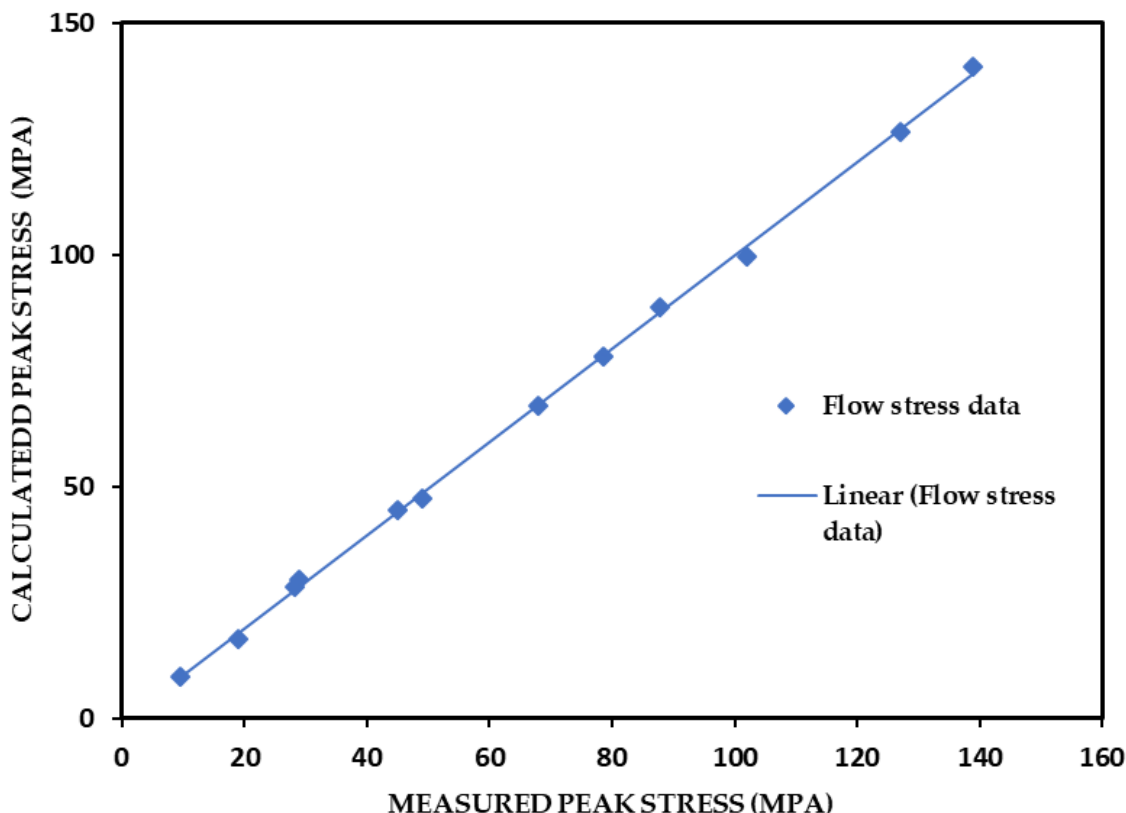
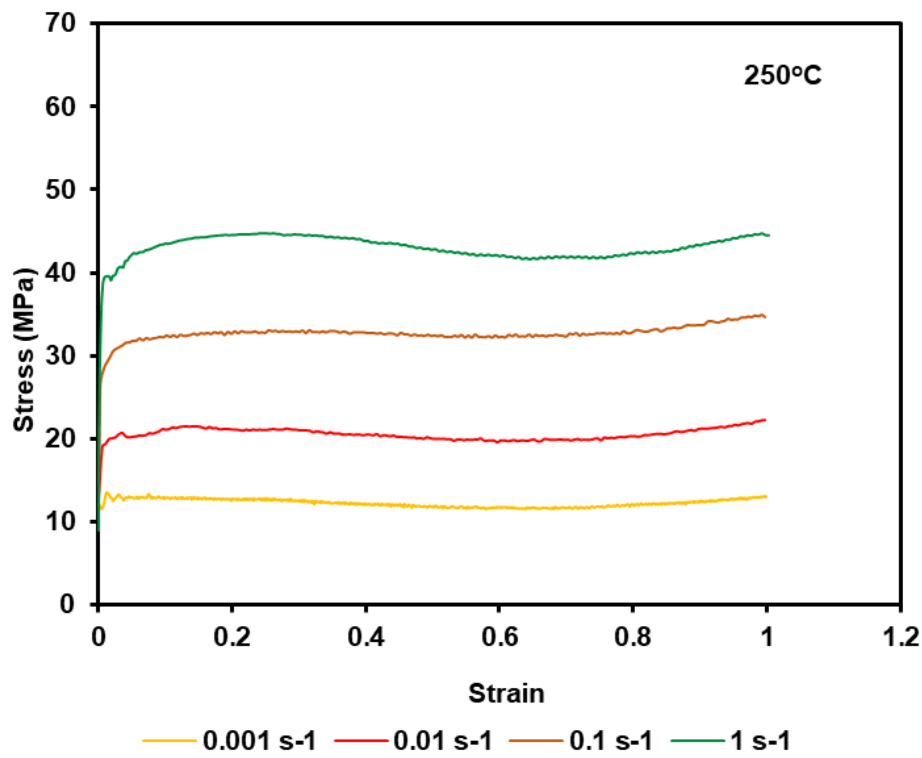


Figure 4-16. Comparison between the measured peak stress and the calculated peak stresses based on hyperbolic sine function.

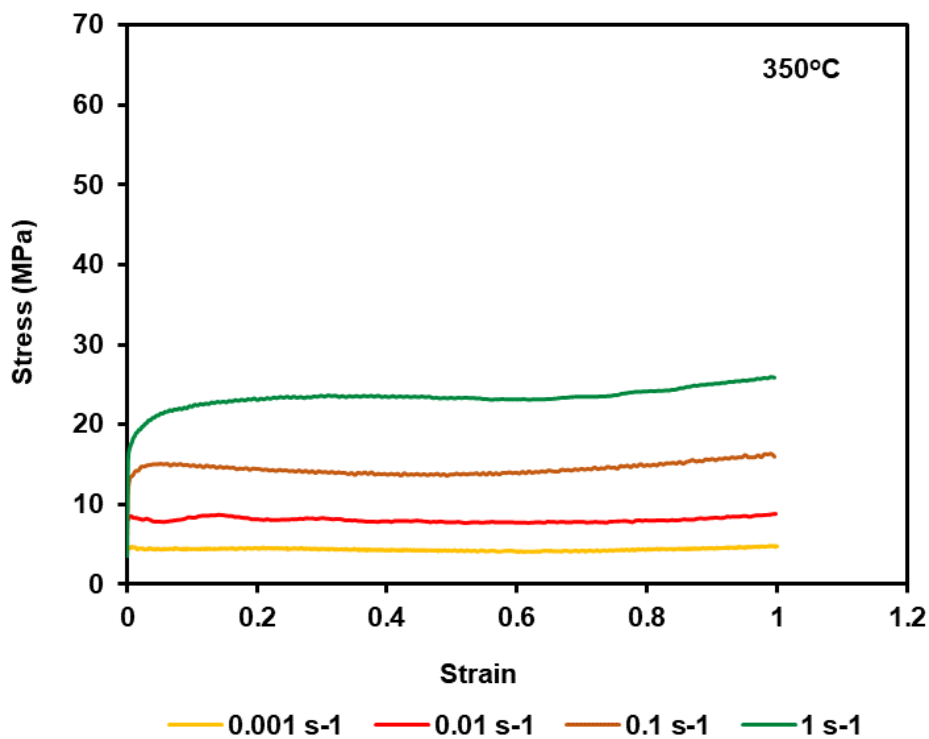
4.2. Mg-14Li-1Al alloy

4.2.1. Effect of temperature on flow graphs

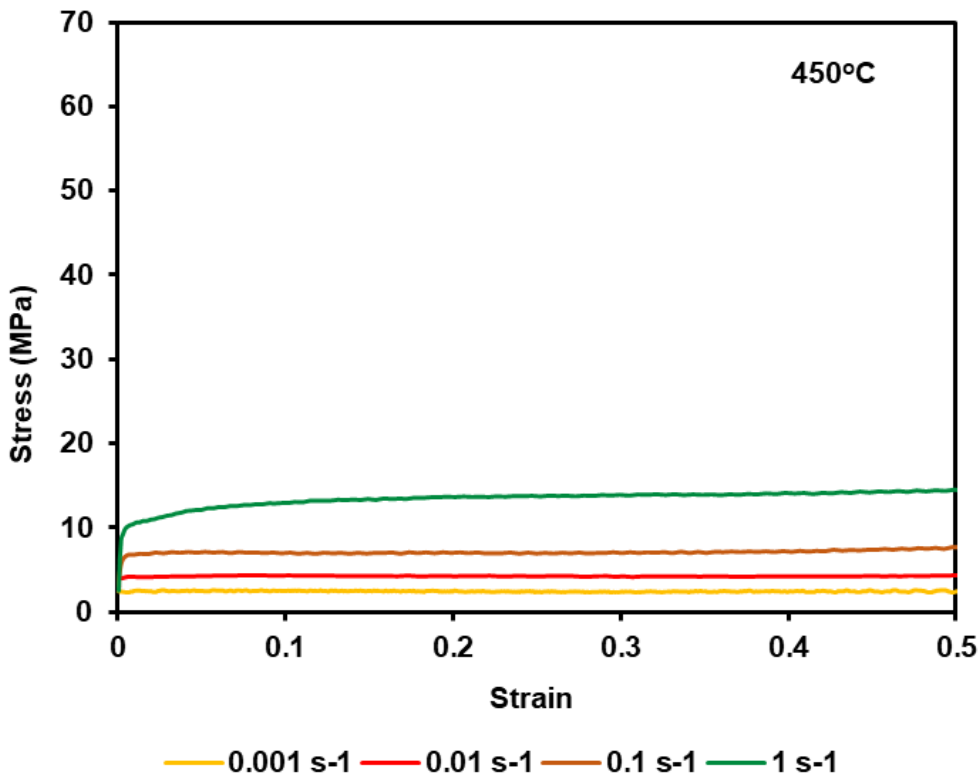
Figure 4-17 shows that temperature possesses significant effects on the flow stress curves. The variety pattern of the flow is that the stress initially increases sharply to a peak value and afterwards decreases gradually to an enduring state as the strain increments. A decline in the stress level is seen with the expansion of deformation temperature.



a



b



c

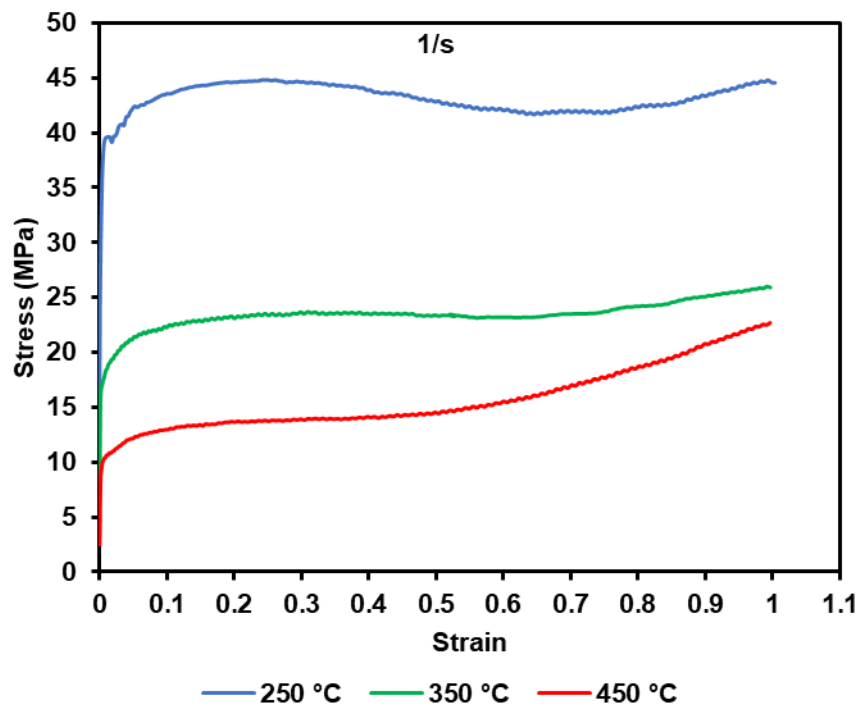
Figure 4-17. Flow curves of the Mg-14Li-1Al alloy at a) 250°C, b) 350 °C, c) 450°C.

At 450 °C, one feature that is observed in the graphs is different than the common characteristics of reaching to a maximum peak; i.e. the flow graphs do not show any maximum peak point. The graphs are more like at steady state for the strains of 0.001/s, 0.01/s and 0.1/s. A steady state flow graph at elevated temperature is usually an outcome of a well balance between work hardening and work softening (dynamic recovery). For this alloy, it is notable that the flow stress is reduced at the elevated temperatures. One reason behind this is more slip system has been activated at high temperatures in bcc structured Mg-Li alloys. Another reason is, the consequences of

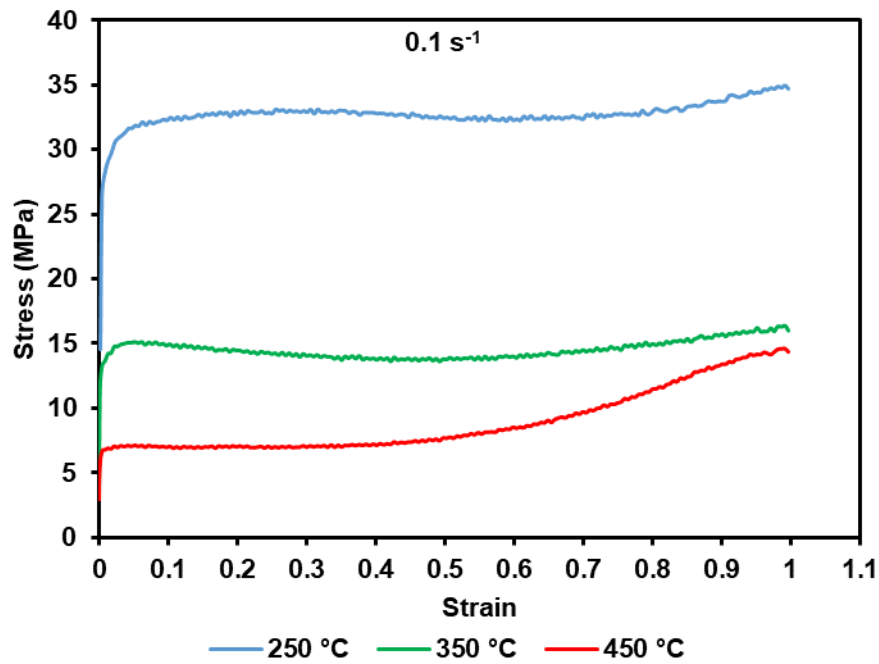
high temperature deformation renders better mobility at the grain boundaries for dynamic recovery. Therefore, the stress level has decreased.

4.2.2. Effect of strain rate Flow Graphs

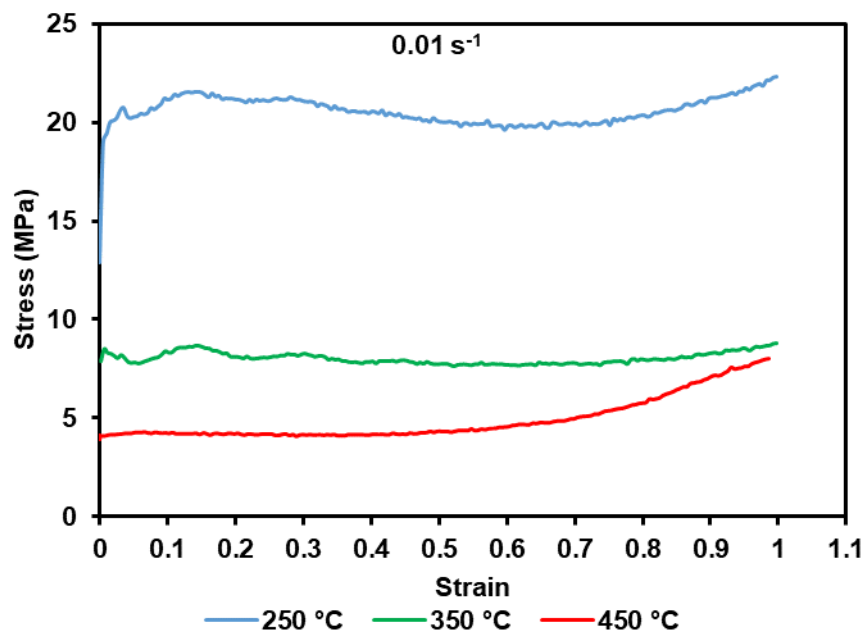
The effect of strain rate on flow curves has been analyzed by plotting true stress vs true strain curves at four different strain rates of 0.001/s, 0.01/s, 0.1/s and 1/s, for three different temperatures of 250 °C, 350 °C and 450 °C (Fig. 4-18). It has been observed that the flow stress for this alloy is increasing with higher strain rate at all three temperature of deformation. The reason behind this flow stress rising is dislocation density which increases with increment of strain rate. This feature also confirms the positive strain rate sensitivity of this alloy.



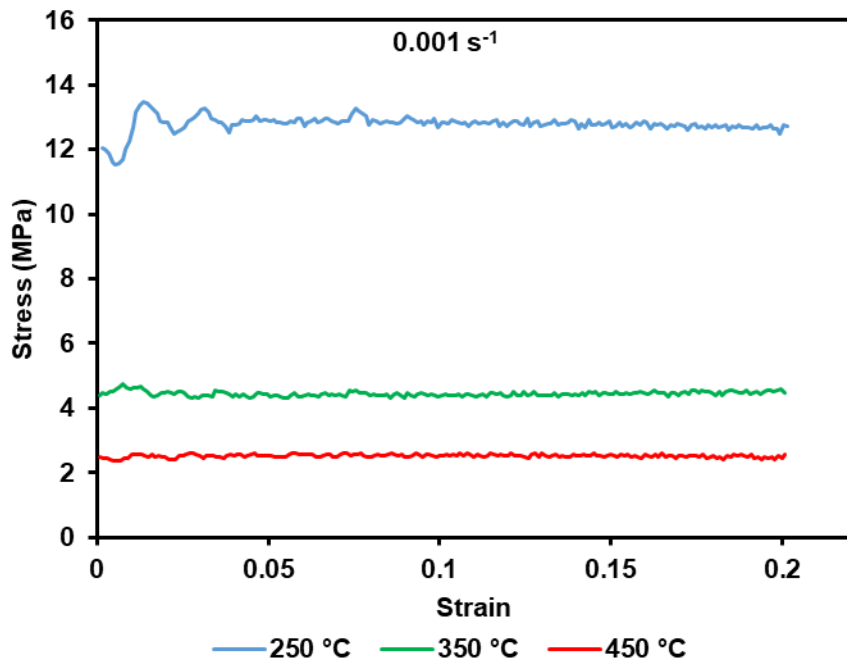
a



b



c



d

Figure 4-18. Flow graphs at different strain rates a) 1/s, b) 0.1/s, c) 0.01/s, and d)

0.001/s.

4.2.3. Microstructure

4.2.3.1. As received alloy

The optical microscopic image for the as received alloy is shown in Fig. 4-19. The microstructure illustrates that it is a single β -phase and BCC structured alloy with equiaxed grains. The average grain size is 100 μm . No other phase is detected through microstructural studies.

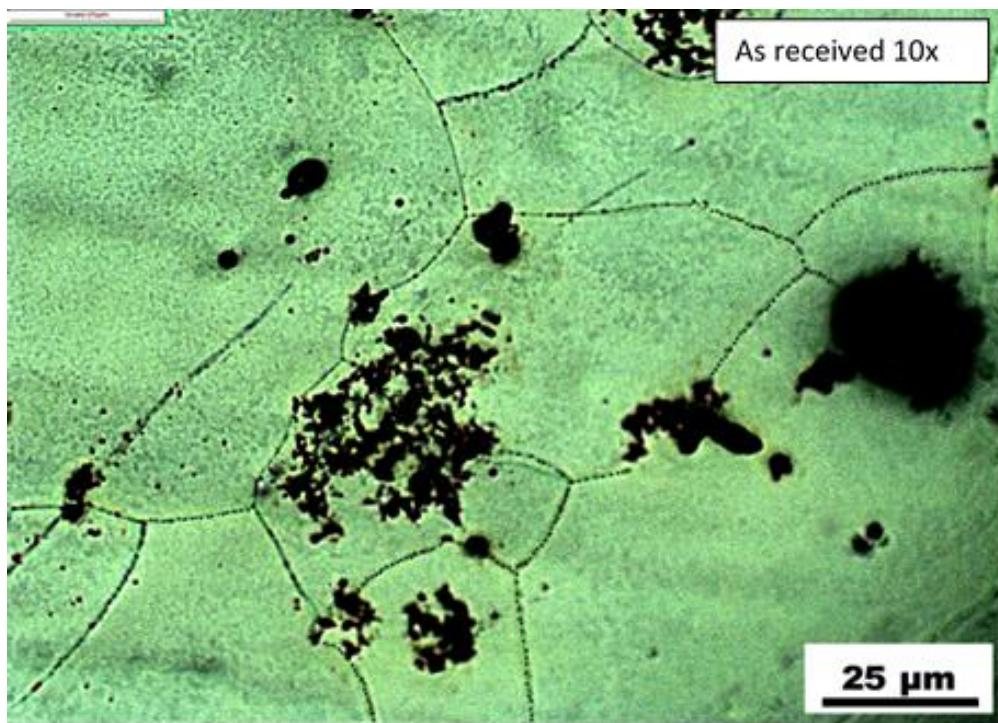


Figure 4-19. Image of microstructure for as-received alloy.

Due to the TMP, the initial microstructure has been affected, especially the grain size of the alloy has changed. When the deformation temperature is 250 °C and the strain rate is 1/s the grain size reduced a lot, afterwards for a deformation temp of 350 °C grain size has started increasing.

Transformation in microstructures for the deformed samples are observed satisfactorily. It is apparent that with enhancing the deformation temperature and strain rate there is change in grain sizes.

During microstructural characterization of the Mg-14Li-Al alloy, one of the most important factor that has been observed is that dynamically recrystallized grains do not

show up on the surface of the alloy. That happens due to the high rate of diffusion of Li in Mg which does not allow enough time to formulate the nuclei. A faster recovery process occurred which cause the annihilation of dislocation without formulation of nuclei. As a result, there is no DRX grains for most of the temperatures and strain rates samples [60].

From Fig. 4-20, changes in microstructures for the deformed samples are observable satisfactorily. It is apparent that with enhancing the deformation temperature grain size increases and with enhancing the strain rate grain size decreases. The gradual change for all the temperatures and strain rates need to be discussed thoroughly.

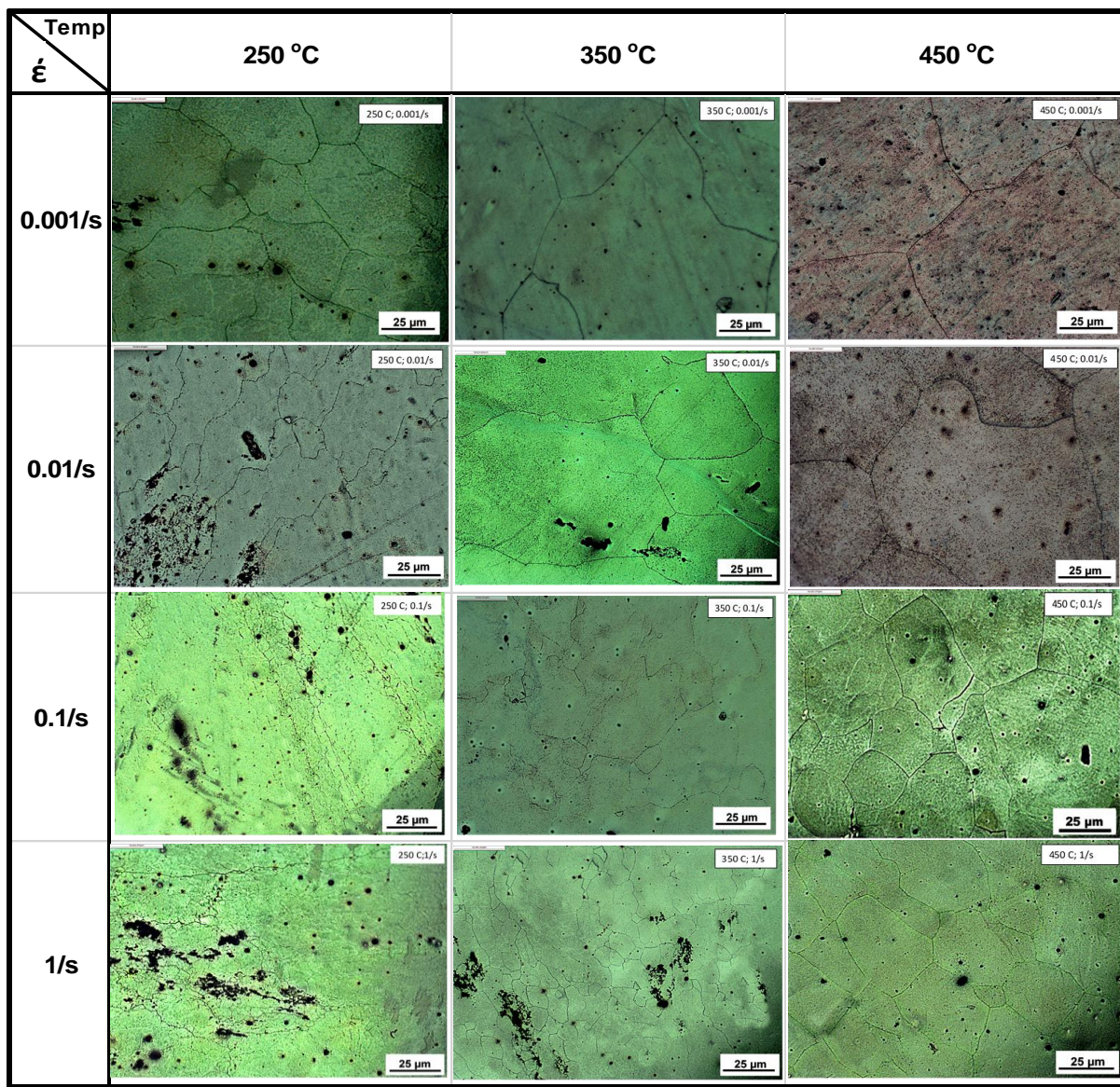


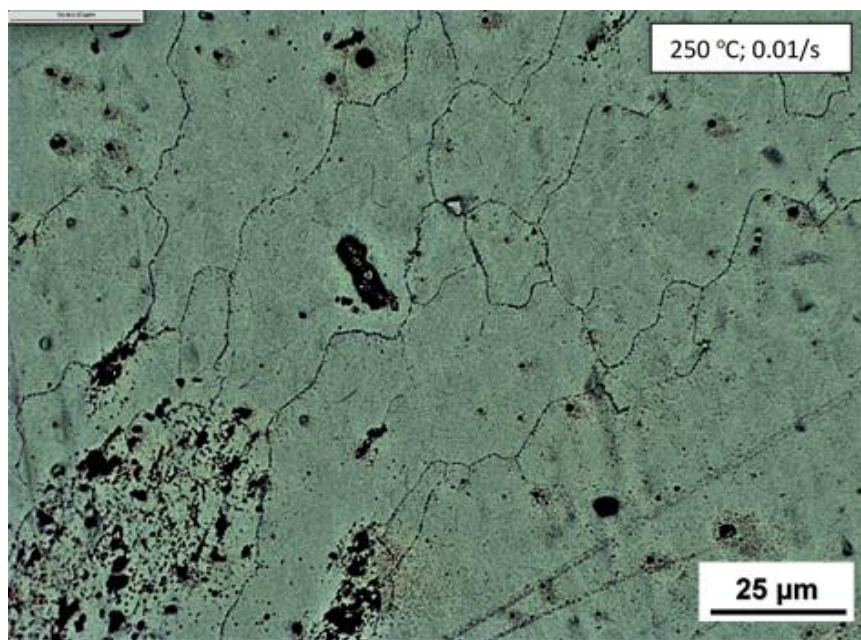
Figure 4-20. Microstructures of the thermomechanically processed Mg-14wt%Li-Al alloy at different temperatures 250°C, 350°C, and 450°C and strain rates of 1, 0.1, 0.01, and 0.001 /s.

Fig. 4-21 represents the optical microscopic images of the post TMP alloys at a constant strain rate and different temperatures. In all the samples equiaxed grains have been observed, no other types of structures have been noticed (e.g., columnar).

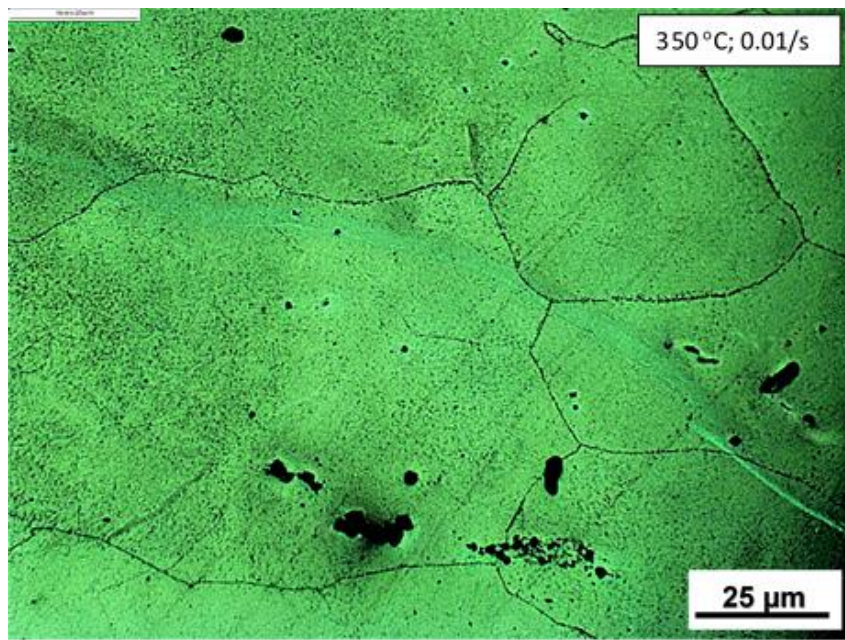
4.2.3.2. Effect of temperature on microstructure

A significant increment in grain size has been observed while the temperature is increasing. The elevated temperature of 250 °C to 450 °C has a significant effect on grain size increment at a constant strain rate. The grain size increment at high temperature follows the simple grain growth rule.

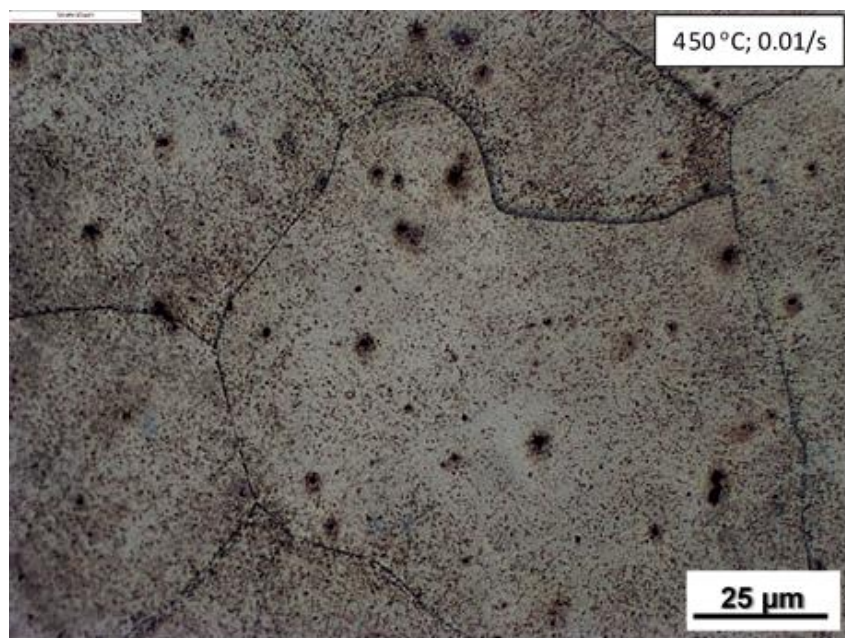
According to the literature, grains will grow in size from very small to very large. The material with smallest grains would possess the largest surface area to volume ratio. Due to their bigger surface area, it is more probable they will dissolve (melt) with rising temperature. Afterwards, this melted or dissolved portion gradually deposits on the remaining large grains. The large size grains turn into even larger consuming the small grains turning smaller or disappearing altogether.



a



b



c

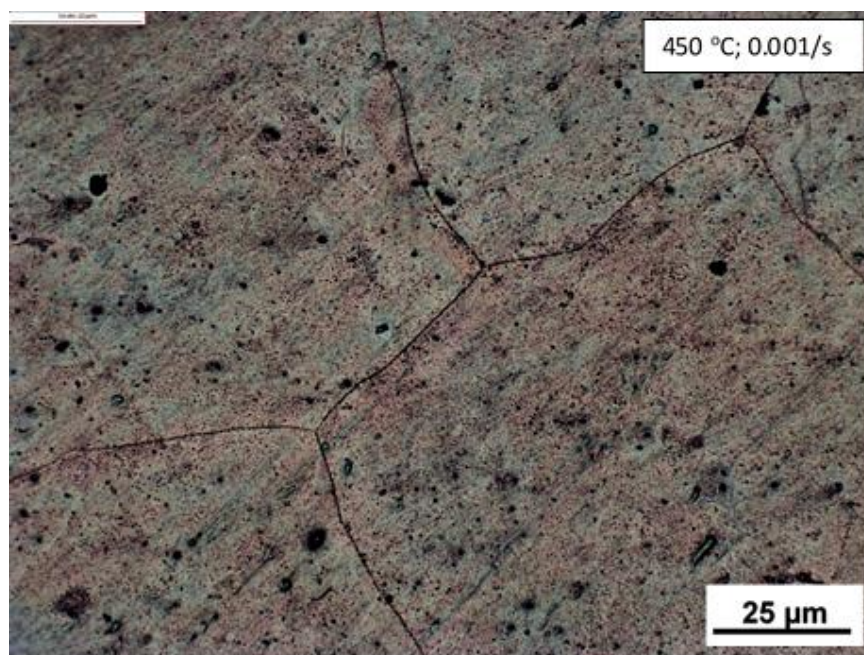
Figure 4-21. Microstructure at 0.01/s a) 250 °C, b) 350 °C, c) 450 °C.

However, when the microstructure of post-TMP samples was compared with the as received alloy, a significant reduction in the grain size for the 250 °C deformed sample

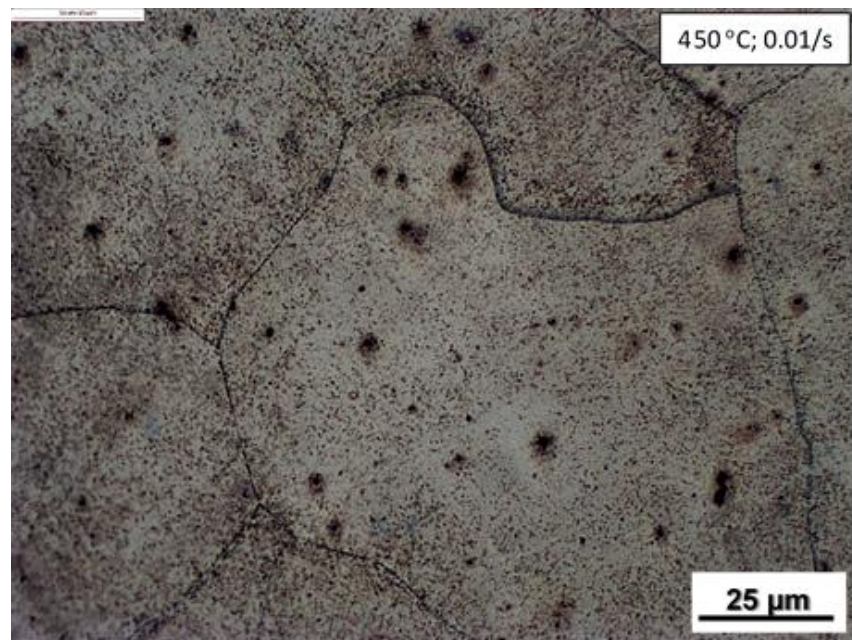
was observed. This deformation temperature was not enough to start grain growth process after dynamic recovery and recrystallization.

4.2.3.4. Effect of strain rate on microstructure

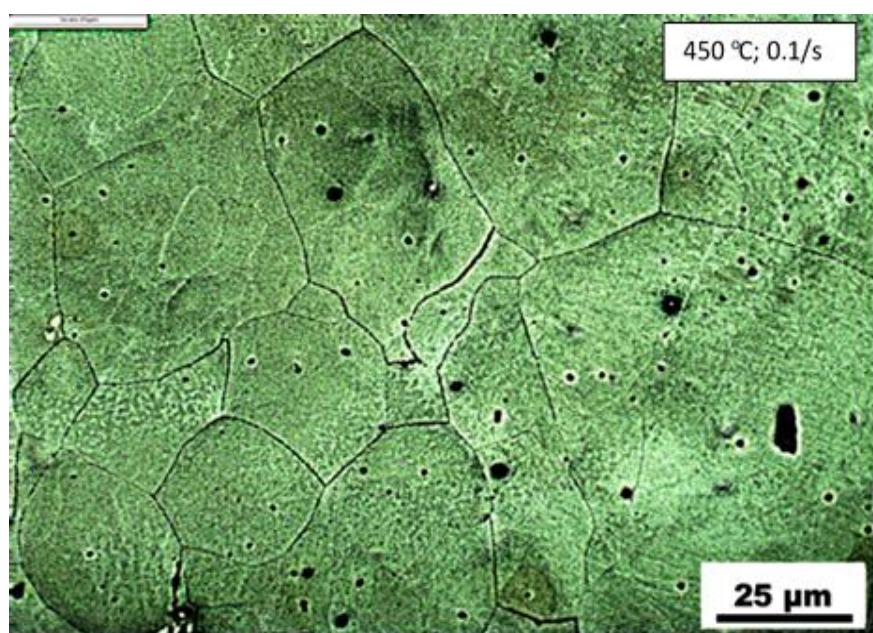
Fig. 4-22 illustrates the microstructural changes as a result of strain rate change at a constant temperature. Because of strain rate increment, grain size decrement is notable. The microstructure for 1/s strain rate is much finer than the 0.001/s at a constant temperature of 450 °C. Potentially, a higher strain rate does not provide enough time for grain growth.



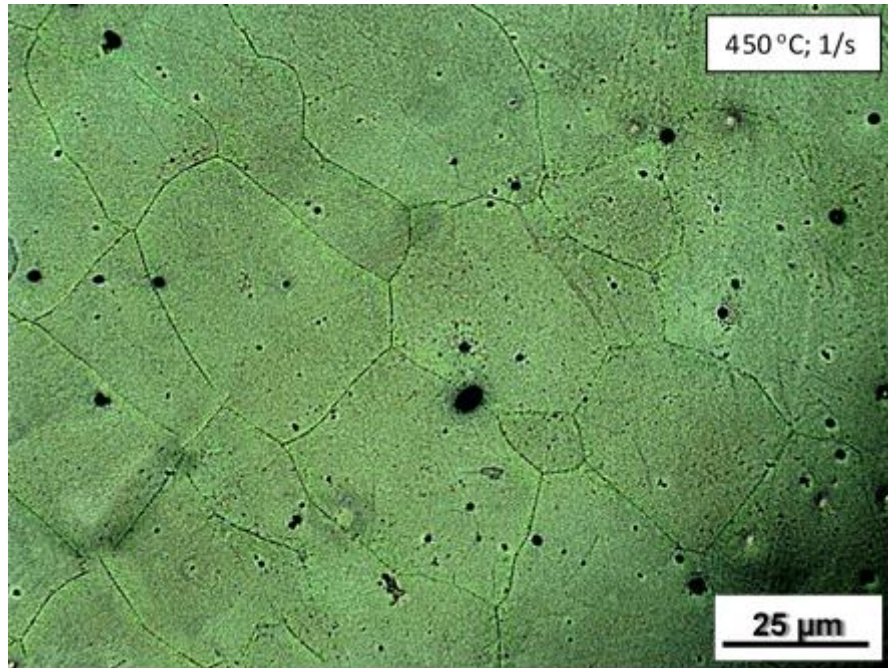
a



b



c



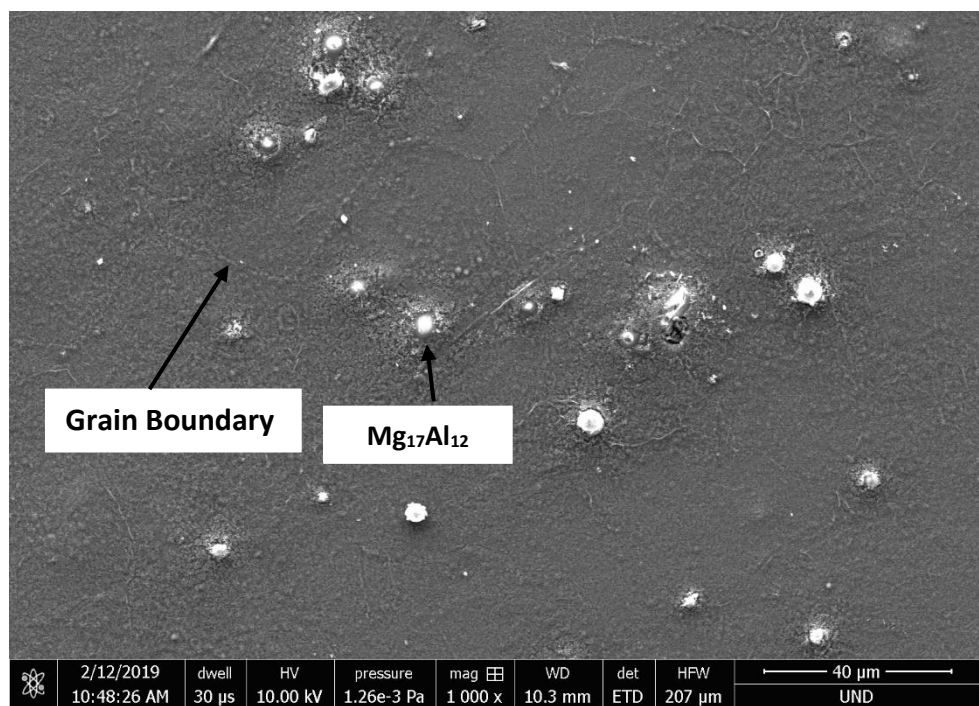
d

Figure 4-22. Microstructures at 450 °C and different strain rates a) 0.001/s b) 0.01/s c) 0.1/s c) 1/s.

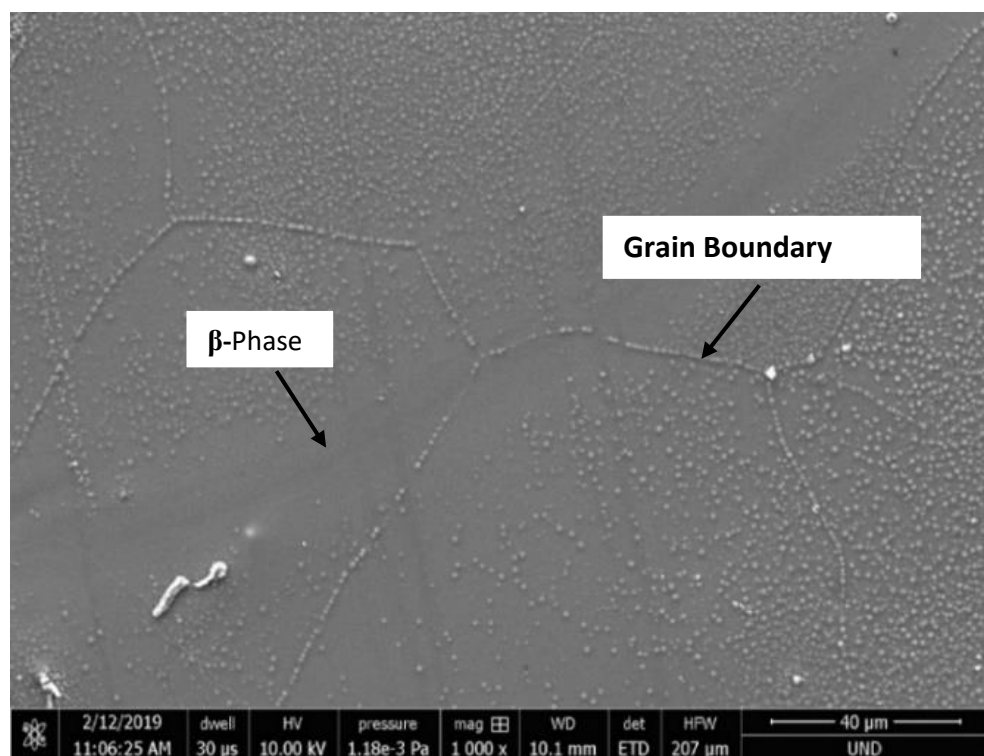
4.2.3.5. SEM

SEM images are demonstrated in Fig. 4-23 for the same strain rate of 0.01/s at various temperatures of 250°C, 350°C and 450 °C. It has been observed that the single β -Li phase is dispersed inside the grain or at the grain boundaries. Also, the grain boundaries are visible clearly. It is worth mentioning that $Mg_{17}Al_{12}$ compounds exist in this alloy.

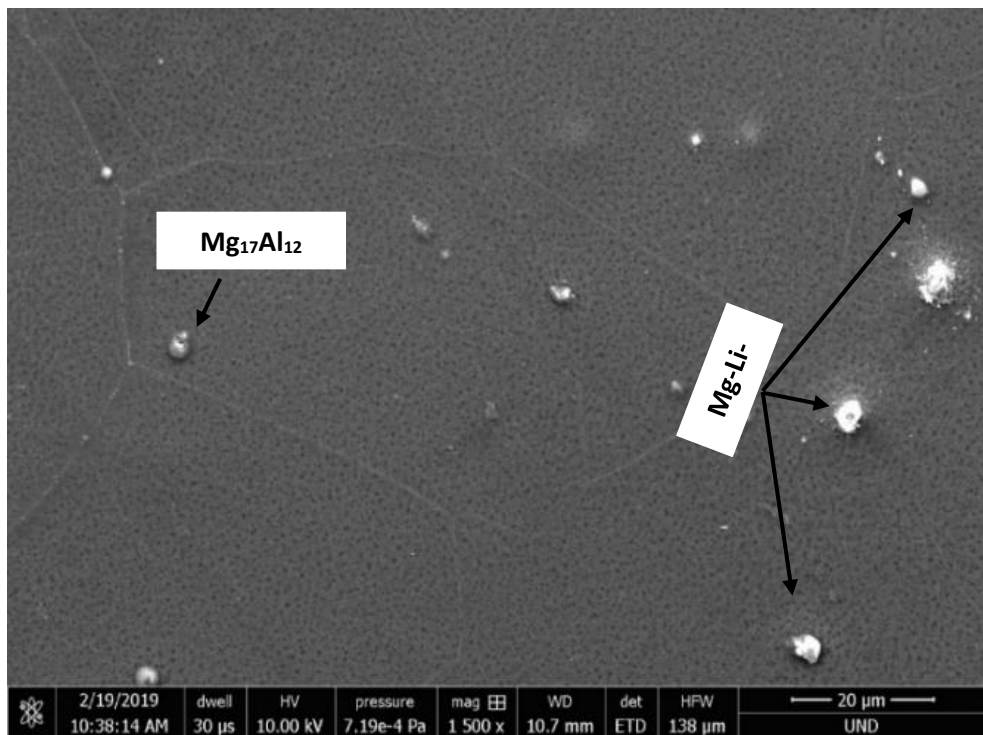
Upon comparing the Figs. 4-24a, b and c, it is obvious that elevated temperature deformation increases the grain size and decreases the density of particulates ($Mg_{17}Al_{12}$). The minimum grain size observed is estimated in the range of ~230 μm to ~ 400 μm .



a



b



c

Figure 4-23. SEM images for deformed samples at 0.01/s strain rate and deformation temperature of a) 250 °C, b) 350 °C, c) 450 °C.

Figure 4-24 shows the graph of mass percent of Mg, Al and O in this alloy. Mg possesses the highest peak because of its high mass percent in this alloy. Al shows the smallest peak due to its low mass percent. Micro-area chemical compositions are presented in the Table. 4-2. According to the EDS result, the presence of mass percent of Oxygen in the composition of this alloy is high which means that an oxide or hydroxide layer has formed due to oxidization. As this type of alloy can easily be oxidized amid sample preparation. Convincing part is that this has no effect on maintaining Mg to Al ratio.

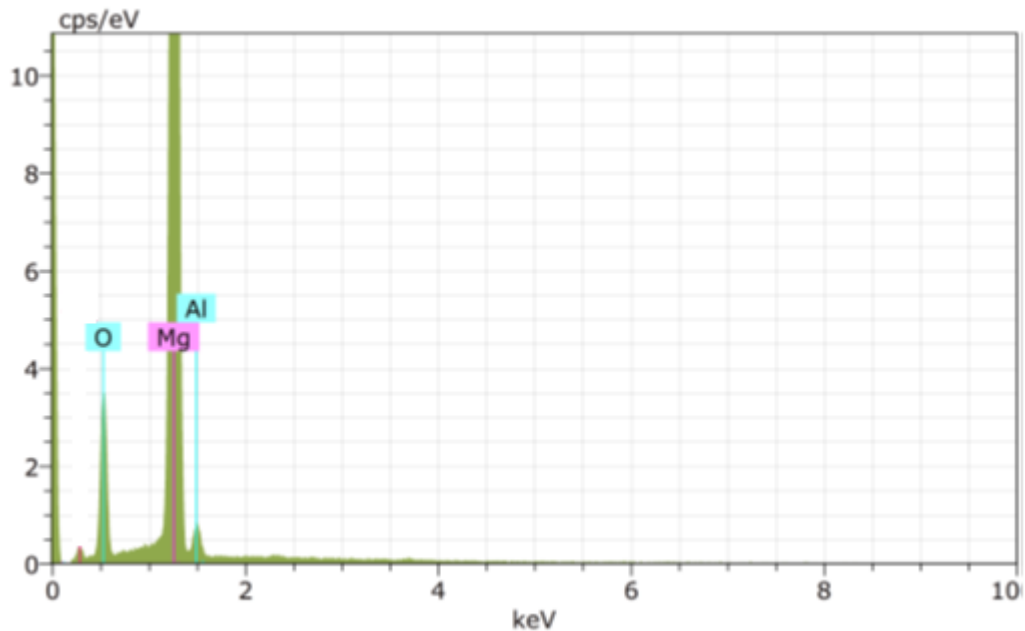


Figure 4-24. Micro-area chemical composition graph from SEM-EDS.

Table 4-2. Micro-area chemical composition analysis result of alloy from Fig. 4-24.

Spectrum	Norm. mass percent (%)		
	O	Mg	Al
14	49.81	32.08	1.39
15	52.76	30.88	1.58
16	53.26	32.14	-
17	48.80	30.37	3.03
18	31.50	44.59	-
20	12.96	62.67	-
21	16.28	79.62	-
Mean value:	37.91	44.62	2.00
Sigma:	17.55	19.39	0.90
Sigma mean:	6.63	7.33	0.34

Mg and Al are identified by SEM-EDS in the alloy surface at point 14, 15 and 17 (Fig 4-25). Li cannot be detected through EDS because of high reactivity of Li and its very low density. Due to that reason during chemical process Li compounds easily formed.

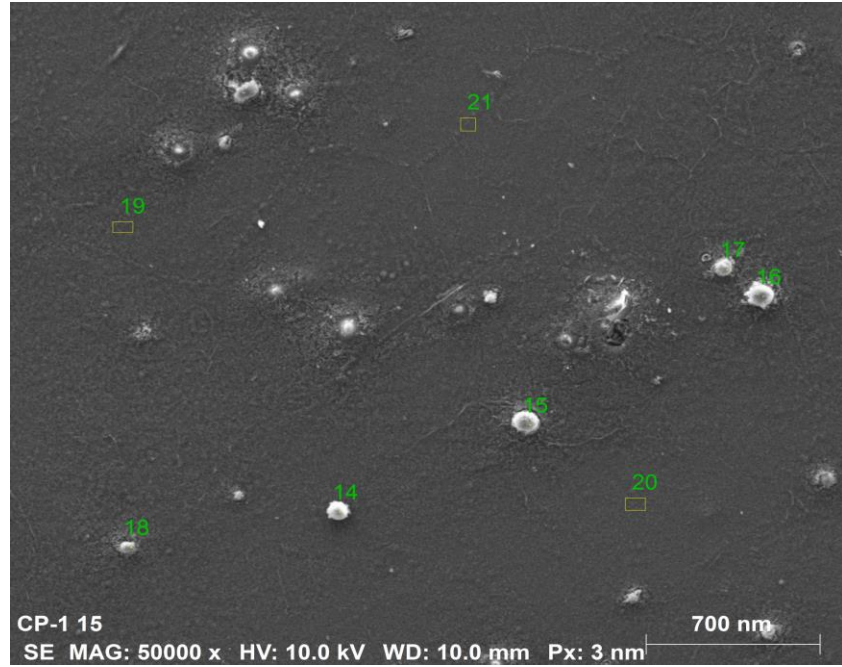


Figure 4-25. SEM-EDS for alloy composition at surface point.

4.2.4. XRD

Typical microstructure for the Mg-14Li-Al alloy before TMP is a wrought alloy microstructure (Fig 4-19). This is composed of Li-rich β phase. In general Mg is α -phase (HCP). Therefore, it is obvious that the presence of alloying elements has altered the phase of the crystal structure. The phase distribution is quite spontaneous. For this phase the weight of Li content is 95.9% and Mg content is 4.1%.

The XRD pattern (Fig 4-26) shows the sharp peaks of β -Li phase in both extreme deformation conditions of this alloy. By comparing Fig 4-25. a and b, in the sample deformed at 450°C and 0.001/s, evidences of β -Li phase and $Mg_{17}Al_{12}$ are observed.

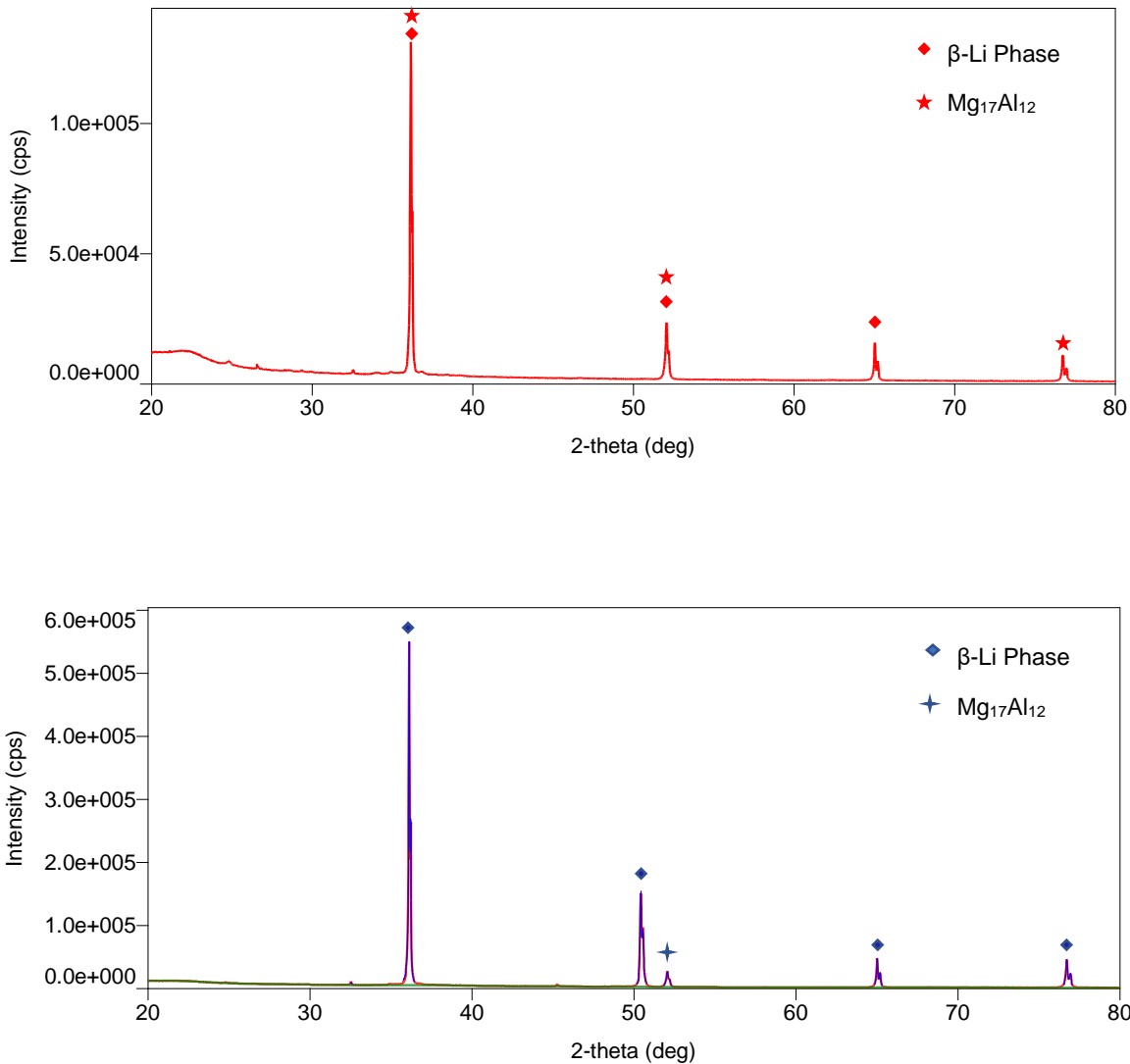


Figure 4-26. XRD pattern of Mg-Li-Al alloy a) 250 °C, 1/s b) 450 °C, 0.001/s.

4.2.5. Nanoindentation

In the nanoindentation process, the loading process is divided into three phases; at first, loading to the peak load of 7.5 mN in loading time of 5 s, then holding time of 2 s, and unloading time of 5 s. This results in an indentation depth of around 400 to 500 nm. Fig.

4-27 represents the load-displacement graph attained from nanoindentation results, for the as-received alloy.

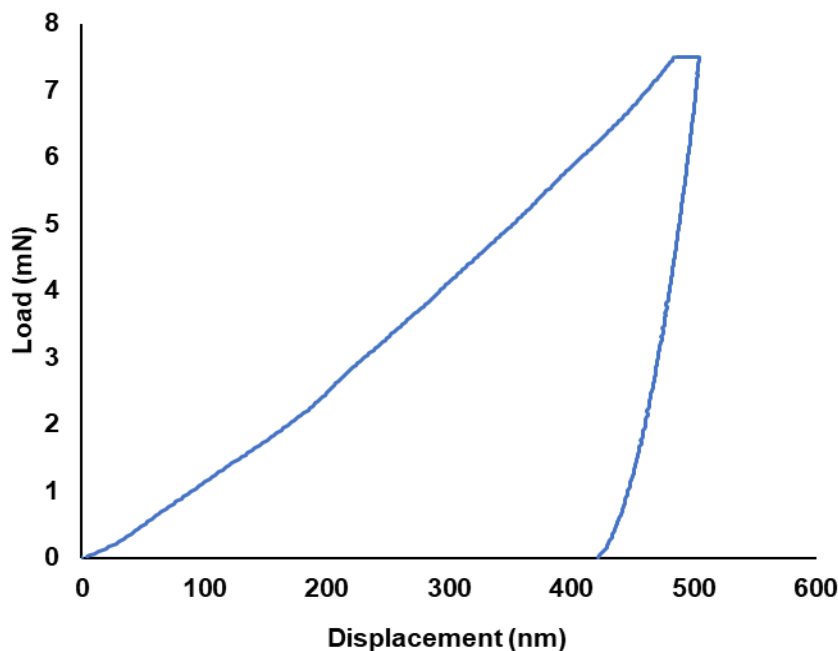


Figure 4-27. Nanoindentation results of the as-received alloy.

Later, for all the thermomechanically processed samples, the same amount of load (7.5 mN) and loading time have been enforced. The typical load-displacement graph observed at room temperature has been shown in Fig. 4-28. The load-displacement curve shows the variation of indentation depth for different temperatures.

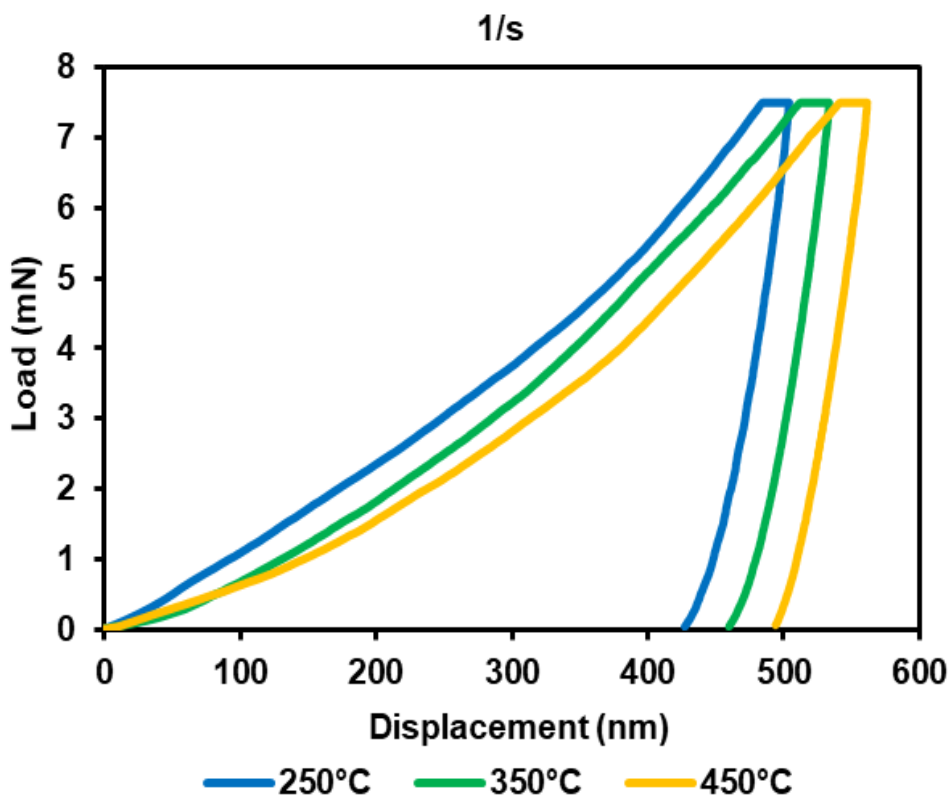


Figure 4-28. Nanoindentation results of the TMPed alloy.

Fig. 4-28 illustrates that the nanomechanical behavior of β -phase present in the investigated Mg-Li-Al alloy which is analyzed by the load–displacement ($P-h$) relationship. The $P-h$ curves of the deformed samples at different temperature overlap with each other and this shows their similar deformation behavior, which might outcome in same type of nanomechanical properties. A close look at Fig. 4-28 depicts that the deformed sample at 250 °C is harder than the 450 °C (depth of penetration is less for the same amount of load). The hardness and elastic modulus values found for different samples are provided in Table. 4-3.

It is interesting to figure it out that the hardness of the as received alloy was lower than the TMP samples. This is because of the grain refinement induced by the TMP cycles. The nanoindentation technique can evaluate the nanohardness and elastic modulus of the deformed samples at different conditions. It has been observed from the SEM diagram that (Fig. 4-24) in case of the TMP samples, ultrafine precipitates exist together with the $Mg_{17}Al_{12}$ compounds. It is most probable that these ultrafine precipitates and coarse $Mg_{17}Al_{12}$ precipitates trap the dislocations motion and restrict the deformation mechanism. Therefore, the hardness and elastic modulus of the deformed samples are higher than that of as received one.

The maximum penetration depth value of the sample deformed at 250 °C was lower than the 350 °C, as illustrated in Fig. 4-29. In case of deformed samples, while increasing the deformation temperature a decrease in the hardness level has been noticed. With the increment of temperature, grain growth as well as precipitation coarsening occur, thus, dislocation trapping decreases in compare to the low deformation temperature. This results in the enhanced ductility of the sample. Moreover, thermomechanical processing promotes the multiplication of mobile dislocations. This illustrates that TMP is also responsible for an increase in the hardness of the individual deformed sample in compare to the initial sample.

The nanoindentation load/depth graph confirms that there is no mechanical instability, *i.e.* serrated yielding characteristic, was observed for all the samples of Mg-14Li-Al

alloy. This yields that the deformation of all the samples including initial sample (before TMP), are homogenous. Therefore, dislocation source activation and their multiplication are appropriate.

As observed in Table 4-3, the as-received alloy possesses low hardness and elastic modulus compared to the thermomechanically processed samples. This can be attributed to the grain refinement in the TMPed samples. The hardness and elastic modulus among the TMP samples show downward trend with increasing the deformation temperature (Table 4-3). This is attributed to a decrease in the work hardening rate as well as grain growth and coarsening of the precipitates/microstructural phases.

Table 4-3. Hardness and elastic modulus results

Material Condition	E (GPa)	Hardness (GPa)
As received alloy	45 ± 1.5	$0.95 \pm .01$
TMPed alloy	250°C	62 ± 2.5
	350°C	56 ± 3.2
	450°C	55 ± 2.1

4.2.6. Constitutive equation of the Mg-14Li-Al alloy

To comprehend the high-temperature plastic deformation behavior, it is required to research the constitutive attributes of the Mg-14Li-Al alloy. To find out the material parameters required for the constitutive equations, the hot compression flow curves at different strain rates and temperatures can be utilized. The stress-strain curves attained from the experimental analysis for this alloy at the strain rates of 1, 0.1, 0.01, 0.001 /s and temperature range of 250°C, 350°C, and 450°C, are appeared in Fig. 4-18. The peak stress graph of the deformed samples during different hot compression testing conditions is shown in the graphs (Fig. 4-29). Due to the decreasing trend of flow stress there is an increase of deformation temperature at a constant strain rate. Also, flow stress rises with the increase of strain rate at a given temperature.

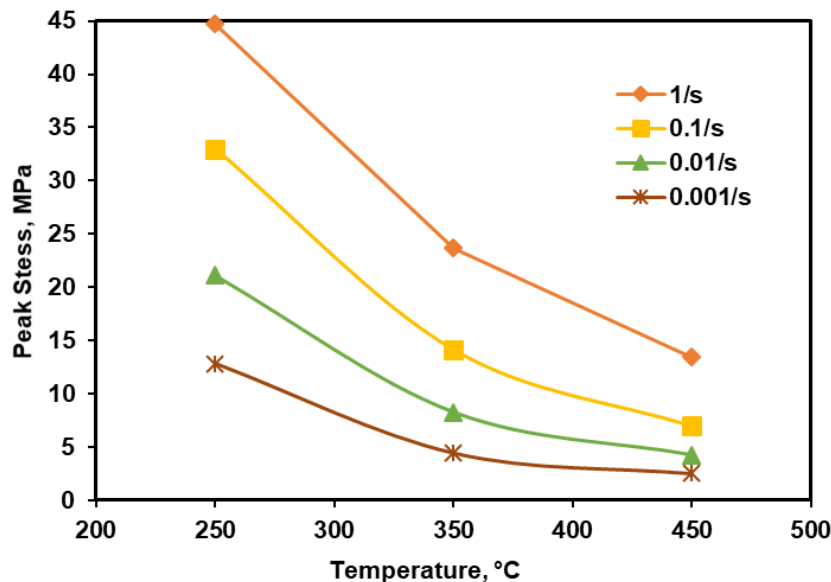


Figure 4-29. Peak stress curves of the studied Mg-14Li-Al alloy.

Considering the deformation temperature (T), strain (ε), strain rate ($\dot{\varepsilon}$) the true stress-strain curves the value of compressive flow stress is determined. Therefore, flow stress can be written as [58]:

$$\sigma = \sigma(T, \varepsilon, \dot{\varepsilon}) \quad (4-12)$$

The relation between temperatures (T), strain (ε), and strain rate ($\dot{\varepsilon}$) at different stress levels can be expressed using the following equations:

$$\dot{\varepsilon} = A\sigma^m \exp\left(-\frac{Q}{RT}\right) \quad (4-13)$$

$$\dot{\varepsilon} = A \exp(\beta\sigma) \exp\left(-\frac{Q}{RT}\right) \quad (4-14)$$

$$\dot{\varepsilon} = A[\sinh(\alpha\sigma)]^n \exp\left(-\frac{Q}{RT}\right) \quad (4-15)$$

where, Q is the activation energy for hot deformation (KJ/mol), R is the ideal gas constant (8.314 J/ (mol.K)), T is the absolute temperature (K), σ is the flow stress (MPa) at a given strain, A , n , α , and β are temperature independent materials constants, where $\alpha = \beta/n_1$, A is hyperbolic sine constant, n is hyperbolic sine power, and α is the stress multiplier.

Equations. 4-13 & 4-14 are valid for low stresses when $\alpha\sigma<0.8$, and for high-stress level $\alpha\sigma > 1.2$, respectively. Eq. 4-15 is applicable to all stress levels.

By taking the natural logarithm of equation 2, 3, and 4 one can find that [59, 53]:

$$\ln\dot{\varepsilon} = \ln A + m \ln \sigma - \frac{Q}{RT} \quad (4-16)$$

$$\ln \dot{\epsilon} = \ln A + \beta \sigma - \frac{Q}{RT} \quad (4-17)$$

$$\ln \dot{\epsilon} = \ln A - \frac{Q}{RT} + n \ln [\sinh(\alpha \sigma)] \quad (4-18)$$

From Eqs. 4-17, 4-18 the relation between $\ln \dot{\epsilon}$ - σ and between $\ln \dot{\epsilon}$ - $\ln \sigma$ are found by utilizing flow stress data under various temperatures and strain rates under a definite deformation condition (i.e. $\varepsilon = 0.2$), see Figs. 4-31 & 4-32. The slope of linear relationship fitting graphs would be n_1 and β .

4.2.7. Constitutive analyzing using the Zener-Hollomon model

Zener Hollomon (Z) parameter is commonly utilized to depict both the effects of strain rate and temperature on the hot deformation behavior of materials. The equation for Z parameter can be written as:

$$Z = \dot{\epsilon} \exp\left(\frac{Q}{RT}\right) = A[\sinh(\alpha \sigma)]^n \quad (4-19)$$

Activation energy can be found by differentiating equation 8:

$$Q = R \left\{ \frac{\partial \ln \dot{\epsilon}}{\partial \ln [\sinh(\alpha \sigma)]} \right\} \left\{ \frac{\partial \ln [\sinh(\alpha \sigma)]}{\partial 1000/T} \right\} \quad (4-20)$$

The slopes of the lines are derived with a certain strain ($\varepsilon = 0.2$). Considering the mean value of the slopes, $n = Q_1 = 4.63$, $Q_2 = \left\{ \frac{\partial \ln [\sinh(\alpha \sigma)]}{\partial 1000/T} \right\}$ is achieved from the slope of the curve $\ln [\sinh(\alpha \sigma)]$ - $1000/T$ in a certain strain [53] from Figs. 4-33 & 4-34. The value of $\ln [\sinh(\alpha \sigma)]$ is calculated utilizing the experimental stress data and α under different temperature and strain rate. The mean value of slopes gives $Q_2 = 4.12$.

The value of $\ln A - Q/RT$ would be average intercept of the fitted curve. Therefore, $\ln A = 36.5$, and $\alpha = 0.018$. In the constitutive equation, the effect of strain is explained by expecting that the material constants (α , n , Q and $\ln A$) are a polynomial function of strains. The values have repeated calculations using data for different strains, $\varepsilon = 0.2, 0.25, 0.3, 0.35, 0.4$.

Zener Hollomon equation can be expressed as [53]:

$$\sigma = \frac{1}{\alpha} \ln \left\{ \left(\frac{Z}{A} \right)^{\frac{1}{n}} + \left[\left(\frac{Z}{A} \right)^{\frac{2}{n}} + 1 \right]^{\frac{1}{2}} \right\} \quad (4-21)$$

$$\sigma = \frac{1}{\alpha} \ln \left\{ \left(\frac{\varepsilon \cdot \exp(\frac{Q}{RT})}{A} \right)^{\frac{1}{n}} + \left[\left(\frac{\varepsilon \cdot \exp(\frac{Q}{RT})}{A} \right)^{\frac{2}{n}} + 1 \right]^{\frac{1}{2}} \right\} \quad (4-22)$$

Substituting the values of (α , n , Q and $\ln A$) in Eq. 4-22, we get the flow stress at elevated temperature.

Fig. 4-31 demonstrates a correlation between the determined peak stresses dependent on hyperbolic-sine function and the deliberate peak stresses. The outcomes show that the computed stresses are reliable with the measured stresses, displaying that hyperbolic-sine function can depict the hot deformation process precisely. Along these lines, the hyperbolic-sine function is resolved as the constitutive condition for the tested Mg-Li-Al alloy; as proposed deformation constitutive equation gives an exact and precise estimate of the flow stress for this alloy, and can be utilized to examine the issues amid forming and casting process.

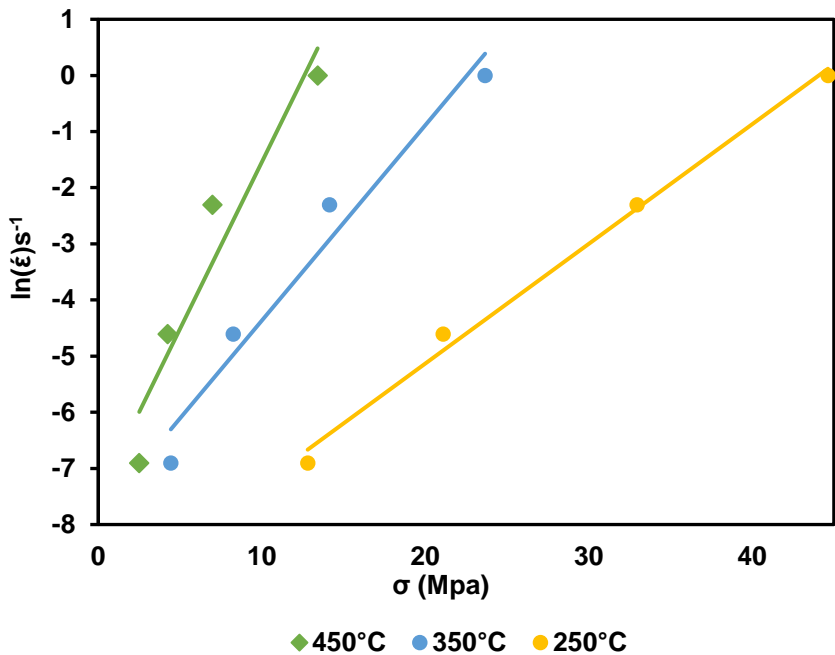


Figure 4-31. $\ln\dot{\epsilon}$ - σ relation curves; symbols show the experimental data and solid lines represent best linear fit.

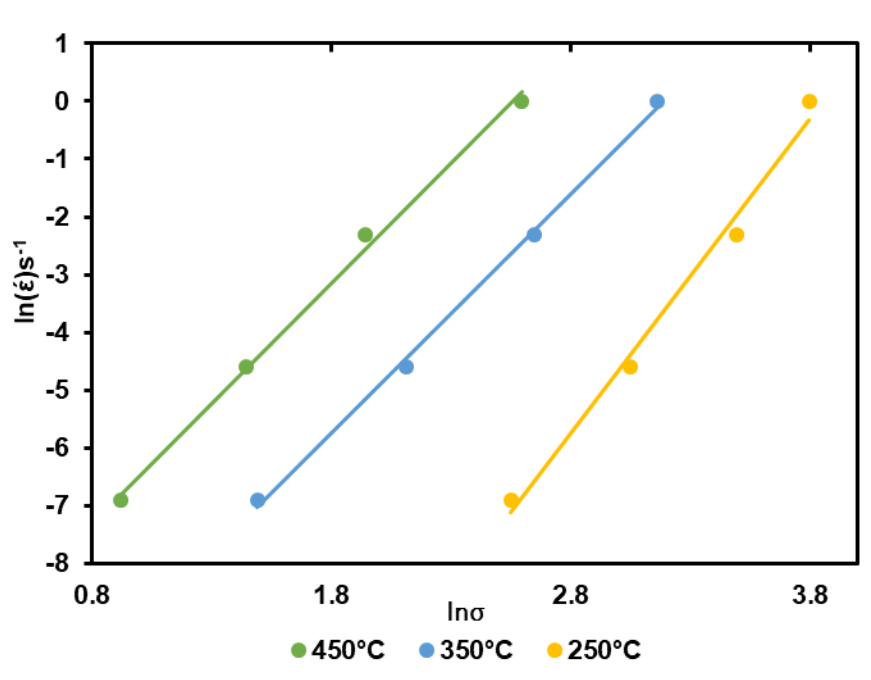


Figure 4-32. $\ln\dot{\epsilon}$ - $\ln\sigma$ relation curves; symbols show the experimental data and solid lines represent best linear fit.

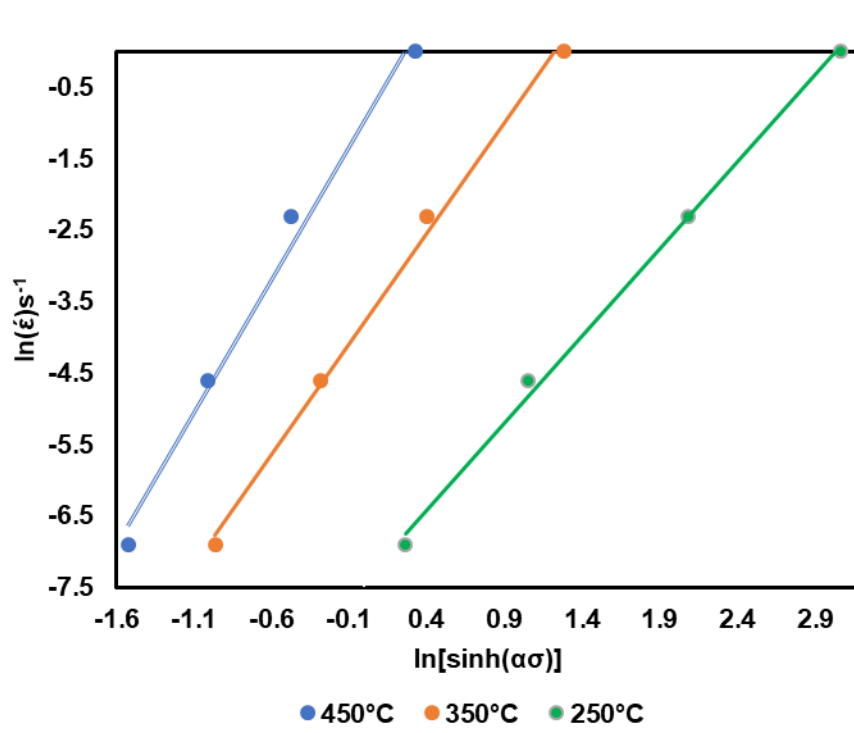


Figure 4-33. $\ln\dot{\epsilon}$ - $\ln[\sinh(\alpha\sigma)]$ relation curves; symbols show the experimental data and solid lines represent best linear fit.

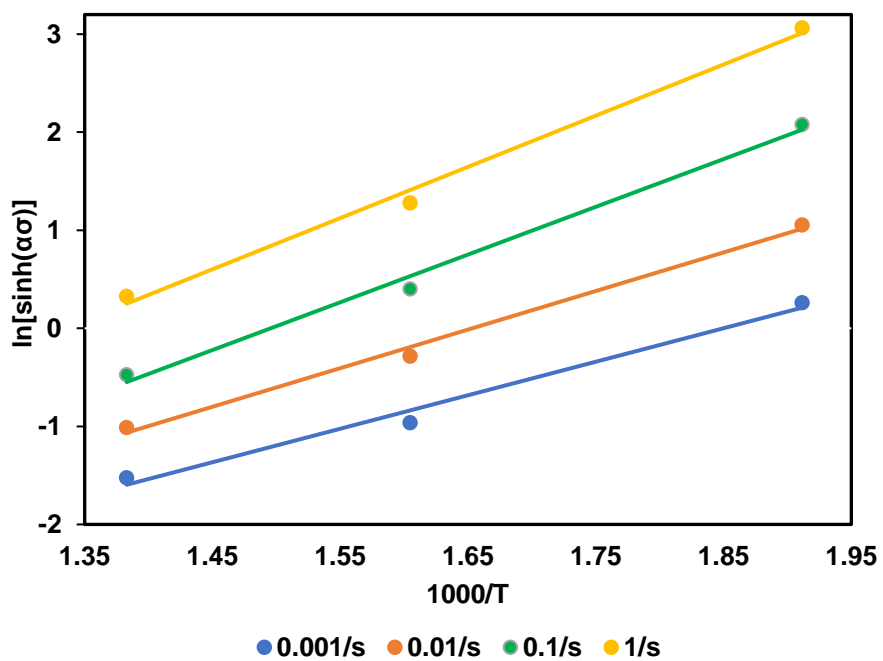


Figure 4-34. $\ln\dot{\epsilon}$ - $\ln[\sinh(\alpha\sigma)]$ relation curve symbols show the experimental data and solid lines represent best linear fit.

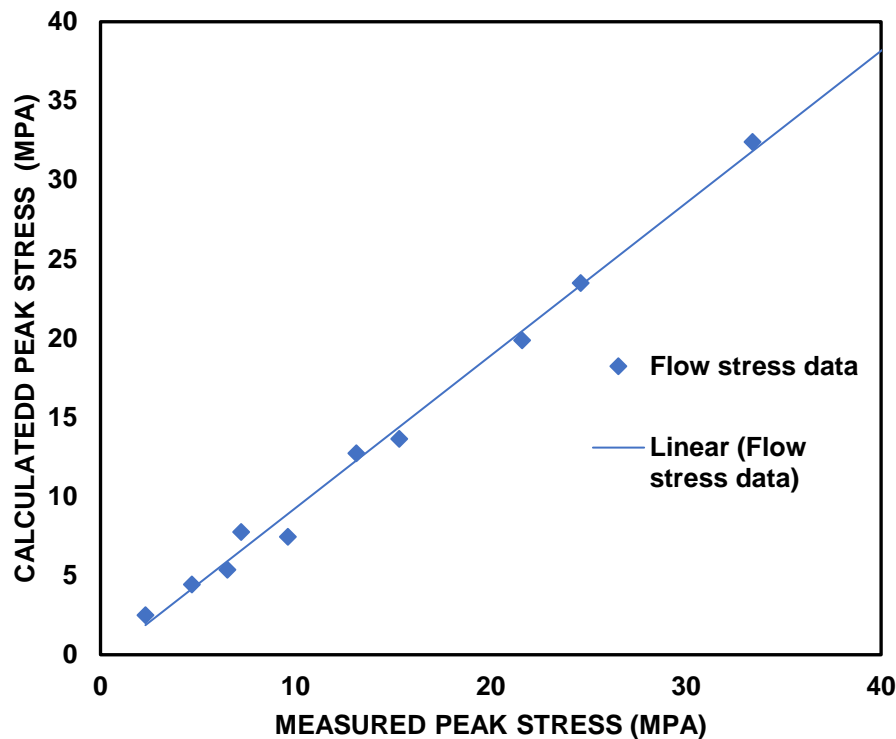


Figure 4-35. Comparison between the measured peak stress and the calculated peak stresses based on hyperbolic sine function.

In this part of the thesis a comparison is made between two studied alloys, Mg-3.5Li-Al and Mg-14Li-1Al, to provide an overview on their mechanical and microstructural characteristics as well as their TMP responses.

4.3. Comparison between Mg-3.5Li-Al & Mg-14Li-Al alloy

4.3.1. Mechanical Properties

Mg-3.5Li-Al is denoted as "A" and Mg-14Li-Al denoted as "B" to follow easily in the comparison.

Due to the difference in weight percentage of Li inclusion in Mg there is phase transformation in alloy "B" and thus have dissimilarities with alloy "A". Thereby, their

structure and mechanical properties are different. Table. 4-4 provides the fundamental differences between these alloys.

Table 4-4. Characteristics differences of the alloys

Characteristics	Mg-3.5Li-Al	Mg-14Li-Al
Phase	α -Mg	β -Li
Structure	HCP	BCC
Type of Phase	Hard	Soft
Deformation behavior	Brittle	Ductile
Corrosion resistance	Better	Poor

4.3.2. TMP results comparison

Upon TMP, some major changes happen in both alloys in compare to their as-received samples. Hot compression flow graphs highlight the deformation characteristics after deforming the samples at elevated temperature of 250 °C, 350 °C and 450 °C and strain rates of 0.001/s, 0.01/s, 0.1/s and 1/s.

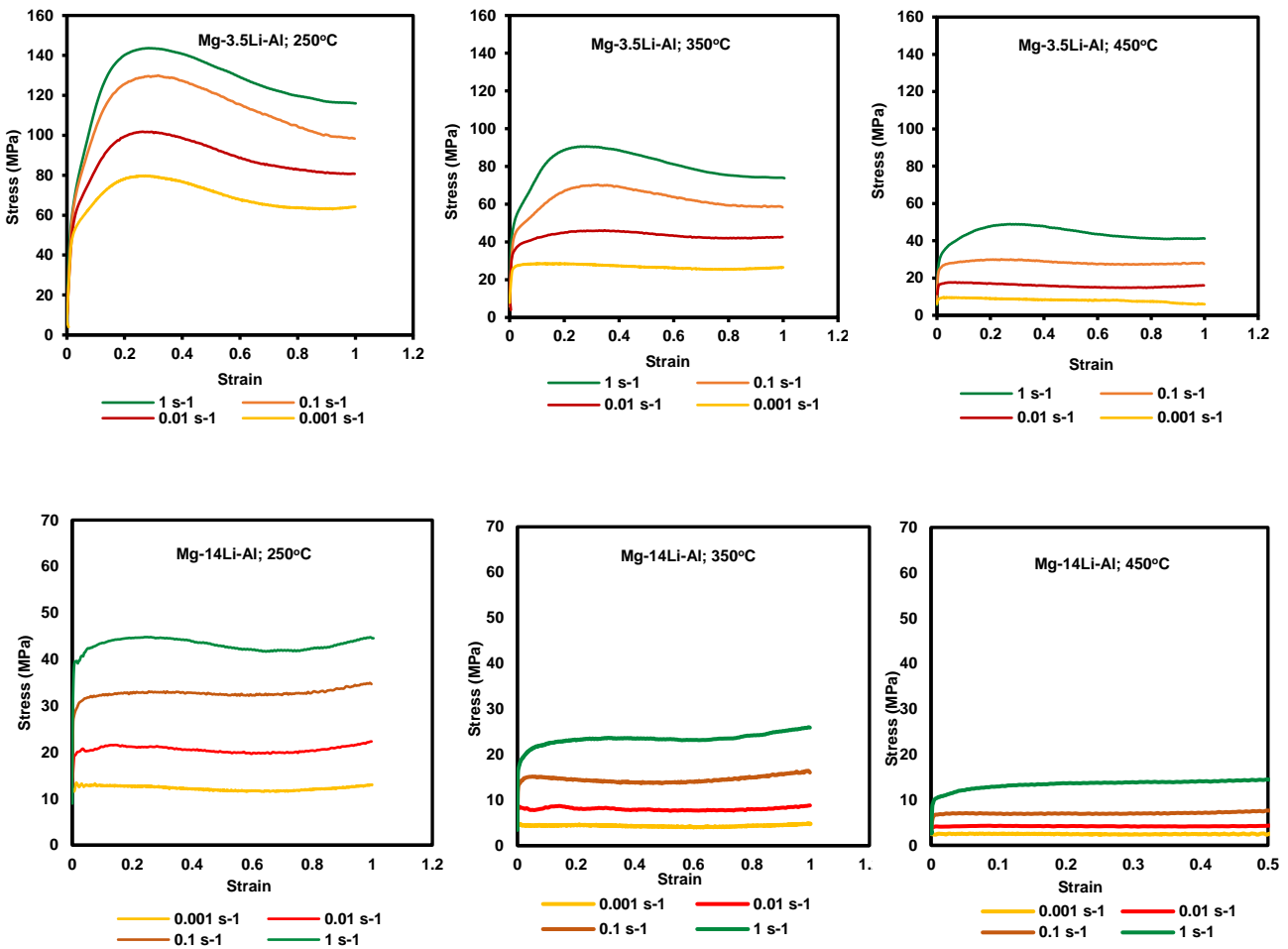


Figure 4-30. Flow graph comparison.

Fig.4-36 shows the flow behavior for two alloys. Since the alloy "A" contains α -phase, it is the harder one, when deformed at lowest temperature of 250 °C and highest strain rate of 1/s. Alloy "B" contains β -phase which is softer; if deformed in highest temperature of 450 °C and lowest strain rate of 0.001/s it gives the very low stress value of ~ 1 MPa. For the alloy "A" the stress level at all conditions are higher than that of alloy "B". Also, same trend of flow graph has been observed for all the temperature and strain rate for both alloys. At a constant temperature with increase in the strain rate,

stress level increases. At a constant strain rate, with increase in the temperature stress level decreases.

4.3.3. Microstructures

Microscopic observations (Fig. 4-31) yield that in the alloy "A" some recrystallized grains called "necklace structure" are present. However, in the case of alloy "B" there is no evidence of that kind of recrystallized structure. This can be attributed to the presence of higher percentage of Li which is reactive. When Li content is more, diffusion occurs faster therefore the recrystallized grains cannot form.

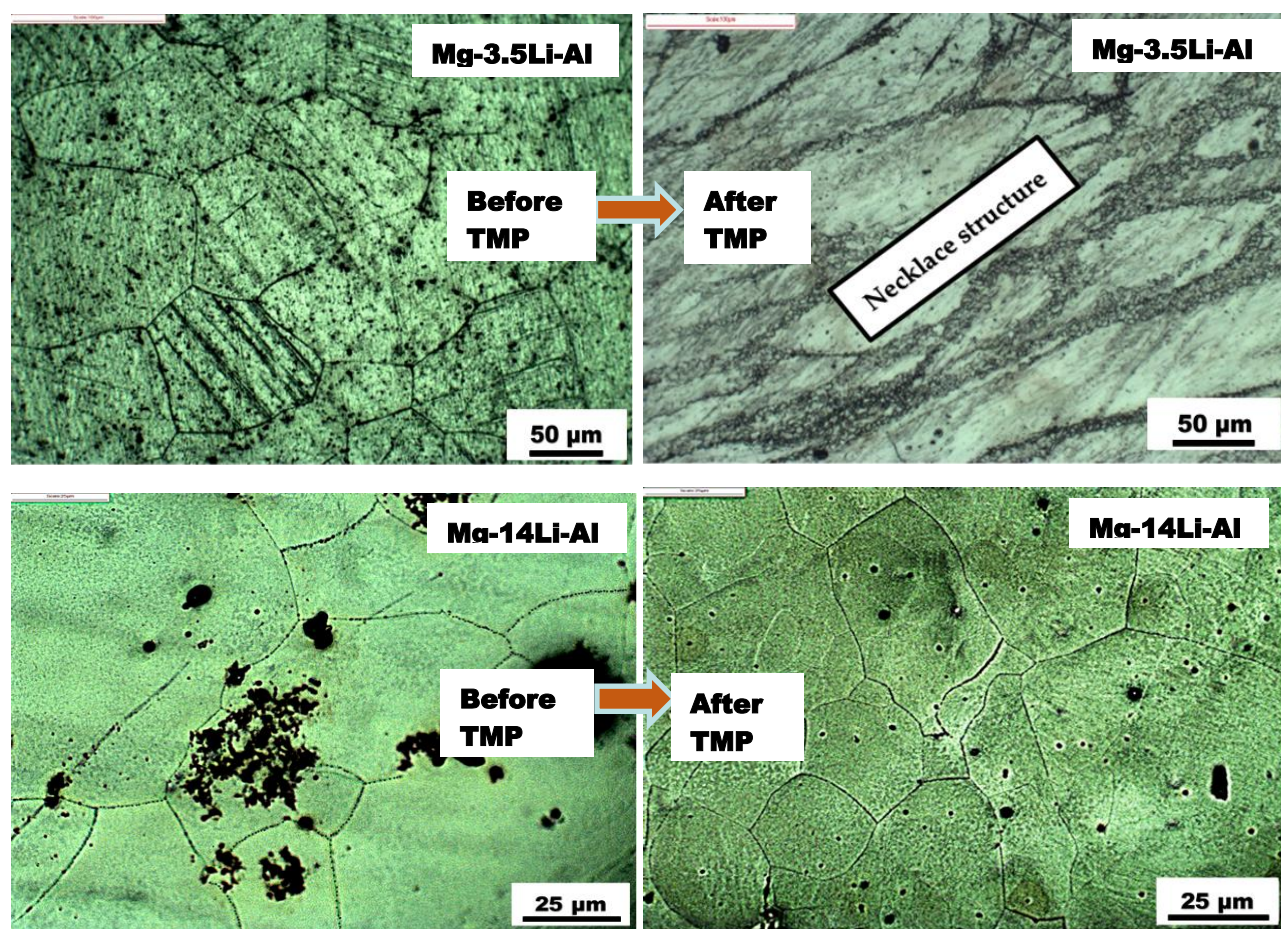


Figure 4-31. Microstructural changes upon TMP.

4.3.4. Nanoindentation results

In this study, nanoindentation testing on two thermomechanically (TM) processed Mg–3.5Li–1Al and Mg–14Li–1Al alloys were carried out within the *hcp* α -phase and the *bcc* β -phase respectively to reveal the mechanical properties of the individual compositions.

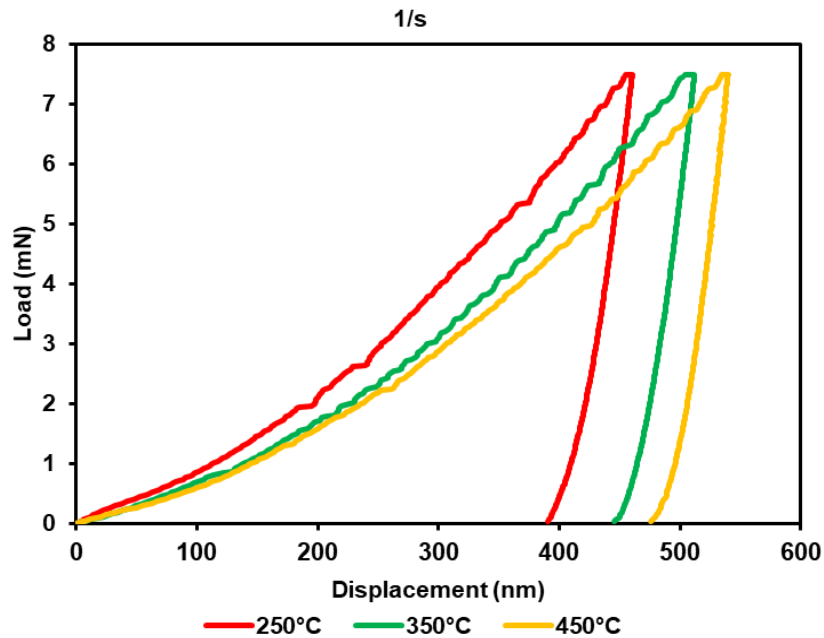
A comparative study on post-TMP properties at 1/s strain rate has been provided in Table. 4-5.

Table 4-5. Hardness & elastic modulus properties comparison

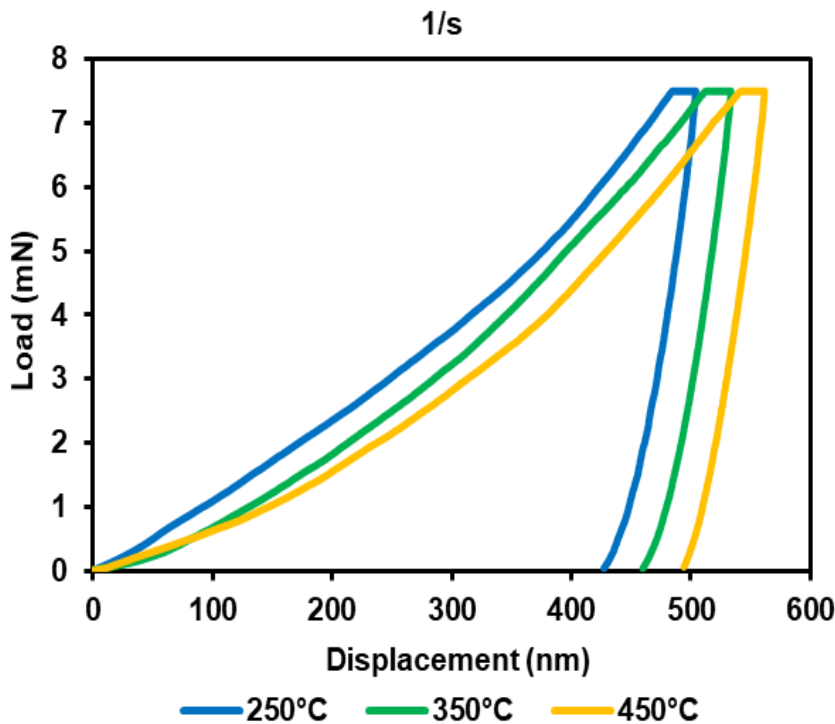
Characteristics		Mg-3.5Li-Al	Mg-14Li-Al
Hardness	As-received alloy	1.01 ± 0.02	0.95 ± .01
	250 °C	1.45 ± 0.05	1.30 ± .02
	350 °C	1.23 ± 0.04	1.12 ± .04
	450 °C	1.12 ± 0.03	1.08 ± .03
Elastic Modulus	As-received alloy	48 ± 2.5	45 ± 1.5
	250 °C	82 ± 4.5	62 ± 2.5
	350 °C	61 ± 3.1	56 ± 3.2
	450 °C	57 ± 3.7	55 ± 2.1

As received alloys for two different compositions were also analyzed to study the effect of TMP on the mechanical properties, such as hardness and elastic modulus. The average hardness and elastic modulus values of TM processed samples measured by nanoindentation were observed and found to be higher than that of as-received alloy.

The elastic modulus and hardness values of both alloys are increased upon the TMP. Serrated flow due to the Portevin–Le Chatelier effect has appeared in the TMPed Mg–3.5Li–1Al alloy and explained in detail; however, in the Mg–14Li–1Al alloy serrations are disappeared (Fig. 4-32a).



a



b

Figure 4-32. Nanoindentation results comparison a) the Mg-3.5Li-Al alloy, b) the Mg-14Li-Al alloy.

Both alloys are single-phase extruded wrought alloys; α - phase alloy "A" and β -phase alloy "B". Both phases are characterized by the load-displacement ($P-h$). In the case of alloy "A" containing α -phase, the highest displacement (h_{max}) was observed for the as-received alloy. For alloy "B" the maximum displacement is comparatively less which means alloy "A" is the harder one.

A close observation of the TMP samples reveals the hardness and elastic modulus values. The hardness values for the deformed samples in the "A" alloy in comparison to the "B" alloy was higher in (table 4-5). In addition, it is interesting to note that the

elastic modulus value is higher for alloy "A" compared with the alloy "B". The investigated magnesium alloys are age-hardenable; it could be possible that the ultrafine precipitates and coarse MgLiAl₂ precipitates anchor the motion of dislocations and provide resistance to deformation in the alloy "A". Hence, the hardness and elastic modulus of the α -phase in the alloy "A" is higher than that of β -phase in alloy "B". Thus, the nanoindentation technique could evaluate the nanohardness and elastic modulus of the α - and β -phases. [61]

The mechanical instability, i.e. serrated flow, was also commonly observed in the alloy "A", as shown in Fig. 4-32. This proves the mechanical instability during the deformation of all the α -Mg phase, due to activation and multiplication of dislocation sources. The phenomenon in which repeated yielding happens during plastic deformation of the alloys is known as the Portevin–Le Chatelier (PLC) effect or serrated yielding. The PLC effect leads to dynamic strain ageing and is caused by interaction between dislocations and mobile solute atoms. It is notable from Fig. 4-32b that alloy "B" does not show any serrations in the load-displacement graph and it is same for all the conditions. Since, 14 wt% addition of Li into Mg forms a less dense structure. It does not allow to grow that volume fraction of precipitates which end up blocking dislocations during plastic deformation.

In this project, the instrument used, and the indentation rate were kept identical for the phase present in alloys "A" and "B". Thus, the effect of indentation rate and

instrumental error was common for all hardness tests and consequently neglected in comparison between mechanical instability behaviors of different phases of Mg-based alloys during the nanoindentation tests.

CHAPTER V

5. Conclusion and Future Work

This research was all about a single-phase Mg-3.5Li-Al (wt%) and a dual phase Mg-14Li-Al (wt%) alloy, considering their structure-property-processing condition for various weight saving applications. To do so, the mentioned alloys were first thermomechanically processed (uniaxial hot compression testing). Afterwards, microstructural, post thermomechanical properties, and hot compression stress-strain graphs were studied to observe the changes in properties upon the thermomechanical processing (TMP). We intend to observe the relation among the microstructure with the small-scale properties and processing parameters (*i.e.* thermomechanical parameters, temperature and strain rate). The hot compression tests were carried out at temperatures of 250°C, 350°C, and 450°C and strain rates of 1, 0.1, 0.01, and 0.001 /s using a Gleeble® 3500 thermal-mechanical simulation testing system. True stress-true strain graphs obtained from the thermomechanical tests were studied to observe and analyze the working behavior of the materials, and to comprehend the microstructural evolution which express intrinsic mechanical properties. Microstructural evolutions, hot compression stress-strain curves, and nanoindentation load/displacement response, to study post-processing mechanical properties, for both alloys were discussed thoroughly in this research work. Additionally, a generic comparison between the two assessed alloys was done to comprehend differences in their mechanical properties.

5.1. Conclusions

In this study, elevated temperature behavior (or TMP) and post-TMP micromechanical properties of ultralight Mg-Li alloys were studied. To this end, OM, SEM, flow patterns, and instrumented indentation results were assessed in detail. The followings are the main findings of this research:

5.1.1. Mg-3.5Li-Al alloy

- Trends show a dynamic recrystallization response at all temperature and strain rates during the thermomechanical processing of Mg-3.5Li-1Al alloy.
- PLC effect is observed in the studied Mg-3.5Li-Al alloy in both as received and TMPed materials.
- The hyperbolic-sine function can explain the hot deformation process of the alloy quite accurately.
- MgLiAl₂ precipitates and solute atoms are considered as contributing factors to the observed PLC effect.

5.1.2. Mg-14Li-Al alloy

- At constant strain rate with an increase in deformation temperature, grain size increases. At constant temperature, with increase of strain rate grain size decreases.
- Dominant microstructural mechanism is Dynamic Recovery.

- Hardness and elastic modulus of the TMPed samples are comparatively higher than the as-received sample.
- The presence of $Mg_{17}Al_{12}$ compounds are the reason for increased hardness and elastic modulus in the TMPed samples.
- No PLC effect were observed in the Mg-14Li-Al alloy neither in as-recived nor in the TMPed materials.
- The hyperbolic-sine function can calculate the stress values quite accurately.

5.1.3. Comparison of Mg-3.5Li-Al and Mg-14Li-Al alloy

- Compared to the Mg-14Li-Al alloy, Mg-3.5Li-Al alloy is the harder.
- No PLC effect were observed in the Mg-14Li-Al alloy. This is probably due to the higher percentage of Li addition.

5.2. Future Work

The main limitation of this work was lack of advanced microstructural assessment to be able to expalin the contolling mechanism in detail. Therefore, to further expand this research work it is suggested to run electron backscaterred difraction (EBSD) as well as TEM assessmenst to clearly observe the evolution in the microstructure employing different TMP parameters. By doing this, one can study, more in detail, the texture and pole figures of the deformed specimens and the as-recived material. The TEM can well be adopted to better explain the PLC effect with robust crystalline evidences. It is also

recommended to run high strain rate compression tests (i.e. 10^1 , 10^2 , and 10^3) to shed light on the strain rate sensitivity of the TMPed samples as compared with the as-received material. It could be interesting to study the microstructural and physical phenomena, i.e. dynamic recovery, DRX, grain refinement, and adiabatic heating, at such high deformation rates.

References

- [1] Pekguleryuz, M. O. "Current developments in wrought magnesium alloys." In Advances in wrought magnesium alloys, pp. 3-62. Woodhead Publishing, 2012..
- [2] Thermomechanical Processing; West virginia University; Mechanical & Aerospace Engineering Department.
- [3] H. S. T. T. Imao Tamura, Thermomechanical Processing of High-Strength Low-Alloy Steels.
- [4] http://www.ndhu.edu.tw/ezfiles/29/1029/img/3034/Chapter8_1041223.pdf.
- [5] [https://en.wikipedia.org/wiki/Recovery_\(metallurgy\)](https://en.wikipedia.org/wiki/Recovery_(metallurgy)).
- [6] Flow and Fracture of Metals and Alloys in Nuclear Environments, Chicago: American Society for testing of materials, 1964, p. 182.
- [7] Guo-Zheng, Quan. "Characterization for dynamic recrystallization kinetics based on stress-strain curves." In Recent developments in the study of recrystallization. IntechOpen, 2013..
- [8] <http://users.encs.concordia.ca/~mmedraj/tmg-books/Recrystallization%20and%20Related%20Annealing%20Phenomena/Introduction.pdf>.
- [9] Kumar, Anil, Santosh Kumar, and N. K. Mukhopadhyay. "Introduction to magnesium alloy processing technology and development of low-cost stir casting process for magnesium alloy and its composites." *Journal of Magnesium and Alloys* (2018).
- [10] Opportunities in Protection Materials Science and Technology for Future Army Applications, The national academics of science engineering and medicine, 2011, p. Chapter: Appendix H: Metals as Lightweight Protection Materials.
- [11] S. M. Chowdhury, D. L. Chen, S. D. Bhole and X. Cao, "Tensile properties of a friction stir welded magnesium alloy: Effect of pin tool thread orientation and weld pitch," *Materials Science and Engineering*, vol. 527, no. 21-22, pp. 6064-6075, 2010.
- [12] A. A. Luo, "Magnesium casting technology for structural applications," *Journal of Magnesiu and Alloys*, vol. 1, no. 1, pp. 2-22, 2013.
- [13] A. K. Dahle, Y. C. Lee, M. D. Nave, P. L. Schaffer and D. H. StJohn, "Development of the as-cast microstructure in magnesium–aluminium alloys," *Journal of Light Metals*, vol. 1, no. 1, pp. 61-72, 2001.
- [14] L. Chen, C. Wang, W. Wu, Z. Liu, G. M. Stoica, L. Wu and P. K. Liaw, "Low-cycle fatigue behavior of an as-extruded AM50 magnesium alloy," *Metallurgical and Materials Transactions A*, vol. 38, no. 13, pp. 2235-2241, 2007.
- [15] A. Boone, "Metals Processing Chapter 14," 2016.

- [16] The Minerals, Metals & Materials Society, "Magnesium Alloys for Automotive Applications," The Minerals, Metals & Materials Society, [Online]. Available: <http://www.tms.org/Communities/FTAttachments/Mg%20Alloys%20for%20Automotive.pdf>.
- [17] Wei, Guo-bing, Xiao-dong Peng, Bao Zhang, Amir Hadadzadeh, Tian-cai Xu, and Wei-dong Xie. "Influence of I-phase and W-phase on microstructure and mechanical properties of Mg–8Li–3Zn alloy"., "Transactions of Nonferrous Metals Society of China 25,, pp. no. 3 (2015): 713-720..
- [18] Singh, P. Bhagat, R. K. Sabat, S. Kumaran, and S. Suwas. "Effect of Aluminum Addition on the Evolution of Microstructure, Crystallographic Texture and Mechanical Properties of Single Phase Hexagonal Close Packed Mg-Li Alloys." Journal of Materials Engi".
- [19] Wei, Guobing, Xiaodong Peng, Amir Hadadzadeh, Yahya Mahmoodkhani, Weidong Xie, Yan Yang, and Mary A. Wells. "Constitutive modeling of Mg–9Li–3Al–2Sr–2Y at elevated temperatures." Mechanics of Materials 89 (2015): 241-253."..
- [20] Pekguleryuz, M. O. "Current developments in wrought magnesium alloys." In Advances in wrought magnesium alloys, pp. 3-62. Woodhead Publishing, 2012."..
- [21] Bettles, Colleen, and Matthew Barnett, eds. Advances in wrought magnesium alloys: fundamentals of processing, properties and applications. Elsevier, 2012."..
- [22] D.Zöllner, Grain Growth, Reference Module in Materials Science and Materials Engineering, 2016.
- [23] Yan, Ying, Wan-Peng Deng, Zhan-Feng Gao, Jing Zhu, Zhong-Jun Wang, and Xiao-Wu Li. "Coupled influence of temperature and strain rate on tensile deformation characteristics of Hot-Extruded AZ31 magnesium alloy." Acta Metallurgica Sinica (English Letters) 2.
- [24] Chavoshi, Saeed Zare, and Shuzhi Xu. "Nanoindentation/scratching at finite temperatures: Insights from atomistic-based modeling." Progress in Materials Science (2018).".
- [25] Ramamurty, Upadrasta, and Jae-il Jang. "Nanoindentation for probing the mechanical behavior of molecular crystals—a review of the technique and how to use it." CrystEngComm 16, no. 1 (2014): 12-23."..
- [26] Zhang, Mengqi, Jinshan Li, Bin Tang, Hongchao Kou, and Jiangkun Fan. "Mechanical characterization and strain-rate sensitivity measurement of Ti-7333 alloy based on nanoindentation and crystal plasticity modeling." Progress in Natural Science: Material".
- [27] Churyumov, A. Yu, and V. V. Teleshov. "Quantitative description of the flow-stress dependence of aluminum alloys at the stage of steady flow upon hot deformation on the Zener–Hollomon parameter." Physics of Metals and Metallography 118, no. 9 (2017):".
- [28] Berkovich Tip nanoindenter tip," Wikipidea, 2016.
- [29] A. Singh, "Hot Working," 2012.

- [30] D. H. Herring, "An Overview of Fundamental Material Properties," *Industrial Heating*, 2017.
- [31] Laser Processing of Metals," *Constitutive Modeling & Computational Materials Science*, 2015.
- [32] Heating on at required temperature - dwell at temperature - cooling," Wilfred Hill, 2016.
- [33] Miles, M. P., T. W. Nelson, C. Gunter, F. C. Liu, L. Fournier, and T. Mathis. "Predicting recrystallized grain size in friction stir processed 304L stainless steel." *Journal of materials science & technology* 35, no. 4 (2019): 491-498.".
- [34] Souza, R. C., E. S. Silva, A. M. Jorge Jr, J. M. Cabrera, and O. Balancin. "Dynamic recovery and dynamic recrystallization competition on a Nb-and N-bearing austenitic stainless steel biomaterial: Influence of strain rate and temperature." *Materials Scien*".
- [35] Recovery (metallurgy)," Wikipidea, 2018.
- [36] R. Brown, "Future of Magnesium Developments in 21st Century," in *Materials Science & Technology Conference*, Pittsburgh, PA, USA, 2008.
- [37] G. Wardlow, "A Changing World with Different Rules – New Opportunities for Magnesium Alloys?," in *64th Annual World Magnesium Conference*, Vancouver, BC, Canada, 2007.
- [38] O. Pashkova, I. Ostrovsky and Y. Henn, "Present State and Future of Magnesium Application in Aerospace Industry," in *New Challenges in Aeronautics*, Moscow, 2007.
- [39] C. D. Lee, "Dependence of tensile properties of AM60 magnesium alloy on microporosity and grain size," *Materials Science and Engineering: A*, Vols. 454-455, pp. 575-580, 2007.
- [40] N. Dziubińska, A. Gontarz, M. Dziubiński and M. Barszcz, "The Forming of Magnesium Alloy Forgings for Aircraft and Automotive Applications," *Advances in Science and Technology Research Journal* 10, pp. 158-168, 2016.
- [41] International Magnesium Association, *Magnesium's Tough Strength Endures Abuse to Protect Portable Electronic Devices*, Wauconda, IL, USA: International Magnesium Association, 2008.
- [42] N. Li, P. Tsung-Yu, R. Cooper, D. Houston, Z. Feng and M. Santella, "Friction stir welding of magnesium AM60 alloy," *Magnesium Technology*, pp. 19-23, 2004.
- [43] K. Gall, G. Biallas, H. Maier, P. Gullett, M. Horstemeyer, D. McDowell and J. Fan, "In-situ observations of high cycle fatigue mechanisms in cast AM60B magnesium in vacuum and water vapor environments," *International Journal of Fatigue*, vol. 26, no. 1, pp. 59-70, 2004.
- [44] Oliver, Warren C., and Georges M. Pharr. "Measurement of hardness and elastic modulus by instrumented indentation: Advances in understanding and refinements to methodology." *Journal of materials research* 19, no. 1 (2004): 3-20.".
- [45] Dr. Mohammad Suliman Abuhaiba, PE; Dislocations & Strengthening Mechanisms; Chapter 7;

11/23/2013".

- [46] Zhang, Xin-Ming, Jian-Mei Chen, Yun-lai Deng, Yang Xiao, and Hao Jiang. "Deformation behavior of Mg-Gd-Y-Zr heat resistant magnesium alloy during hot-compression." Chinese Journal of Nonferrous Metals 15, no. 12 (2005): 1925-1932.".
- [47] Drozd, Zdeněk, Zuzanka Trojanová, and Stanislav Kúdela. "Deformation behaviour of Mg-Li-Al alloys." Journal of Alloys and Compounds 378, no. 1-2 (2004): 192-195.".
- [48] Trojanová, Zuzanka, Peter Palček, Pavel Lukáč, and Zdeněk Drozd. "Influence of solute atoms on deformation behaviour of selected magnesium alloys." In Magnesium Alloys-Properties in Solid and Liquid States. InTech, 2014.".
- [49] Mark Flowers; Sebastian Kossek, "Nanoscinece Instruments"; Mechanical Testing.".
- [50] Dierke, H., F. Krawehl, Stéphanie Graff, Samuel Forest, J. Šachl, and H. Neuhäuser. "Portevin-Le Chatelier effect in Al-Mg alloys: Influence of obstacles-experiments and modelling." Computational Materials Science 39, no. 1 (2007): 106-112.".
- [51] Wang, Cong, Yongbo Xu, and Enhou Han. "Portevin-Le Chatelier effect of LA41 magnesium alloys." Frontiers of Materials Science in China 1, no. 1 (2007): 105-108.".
- [52] Gopinath, K., A. K. Gogia, S. V. Kamat, and U. Ramamurty. "Dynamic strain ageing in Ni-base superalloy 720Li." Acta Materialia 57, no. 4 (2009): 1243-1253.".
- [53] Wei, Guobing, Xiaodong Peng, Amir Hadadzadeh, Yahya Mahmoodkhani, Weidong Xie, Yan Yang, and Mary A. Wells. "Constitutive modeling of Mg-9Li-3Al-2Sr-2Y at elevated temperatures." Mechanics of Materials 89 (2015): 241-253.".
- [54] Aboufadl, Hisham, Johannes Deges, P. Choi, and Dierk Raabe. "Dynamic strain aging studied at the atomic scale." Acta Materialia 86 (2015): 34-42.".
- [55] Wang, Cong, Yongbo Xu, and Enhou Han. "Serrated flow and abnormal strain rate sensitivity of a magnesium-lithium alloy." Materials letters 60, no. 24 (2006): 2941-2944.".
- [56] "Bross S, Hähner P, Steck E A. Mesoscopic simulation of dislocation motion in dynamic strain ageing alloys. Comput Mater Sci,2003, 26: 46-55".
- [57] A. C. Fischer-Cripps, ""Nanoindentation." (2009). Page-147.".
- [58] Yang, Yan, Xiaodong Peng, Fengjuan Ren, Haiming Wen, Junfei Su, and Weidong Xie. "Constitutive modeling and hot deformation behavior of duplex structured Mg-Li-Al-Sr alloy." Journal of Materials Science & Technology 32, no. 12 (2016): 1289-1296.".
- [59] Wei, Guo-bing, Xiao-dong Peng, Fa-ping Hu, Amir Hadadzadeh, Y. A. N. G. Yan, Wei-dong Xie, and Mary A. Wells. "Deformation behavior and constitutive model for dual-phase Mg-Li alloy at elevated temperatures." Transactions of Nonferrous Metals Society o".

- [60] Sivakesavam, O., and Y. V. R. K. Prasad. "Characteristics of superplasticity domain in the processing map for hot working of as-cast Mg–11.5 Li–1.5 Al alloy." *Materials Science and Engineering: A* 323, no. 1-2 (2002): 270-277.".
- [61] How to Select the Correct Indenter Tip," Agilent Technologies., 2009.
- [62] Moxson, Vladimir S., and Eugene Ivanov. "Bulletproof lightweight metal matrix macrocomposites with controlled structure and manufacture the same." U.S. Patent 6,635,357, issued October 21, 2003.".
- [63] Magnesium nano-composites: energy-saving materials of future; Meysam Haghshenas, Manoj Gupta; Emerging Materials and Nanotechnology; June 25-26, 2018 Vancouver, British Columbia, Canada.".
- [64] Wei, Guobing, Xiaodong Peng, Amir Hadadzadeh, Yahya Mahmoodkhani, Weidong Xie, Yan Yang, and Mary A. Wells. "Constitutive modeling of Mg–9Li–3Al–2Sr–2Y at elevated temperatures." *Mechanics of Materials* 89 (2015): 241-253.".
- [65] Somekawa, Hidetoshi, and Christopher A. Schuh. "Effect of solid solution elements on nanoindentation hardness, rate dependence, and incipient plasticity in fine grained magnesium alloys." *Acta Materialia* 59, no. 20 (2011): 7554-7563.".
- [66] Plasticity vs. microstructural characteristics of metals part 1".
- [67] Nanoindenter, Wikipidea, 2016.
- [68] Ladani, L., E. Harvey, S. F. Choudhury, and C. R. Taylor. "Effect of varying test parameters on elastic-plastic properties extracted by nanoindentation tests." *Experimental Mechanics* 53, no. 8 (2013): 1299-1309.".
- [69] Ramamurty, Upadrasta, and Jae-il Jang. "Nanoindentation for probing the mechanical behavior of molecular crystals—a review of the technique and how to use it." *CrystEngComm* 16, no. 1 (2014): 12-23.".
- [70] ""Magnesium and Magnesium Alloys," in *Metals Handbook*, Desk ed.; 2nd ed., ASM International, 1998, pp. 599-574.".
- [71] Nanoindentation – Sample Preparation, Mounting and Positioning, by Fischer-Cripps Laboratories - Lesson 3.
- [72] ASM International, Chapter 14 - fatigue. Elements of Metallurgy and Engineering Alloys, 2008.
- [73] P. Sharifi, "Structure-Property Relationships of Magnesium Alloys," Electronic Thesis and Dissertation Repository. 816, 2012.
- [74] M. K. Kulekci, "Magnesium and its alloys applications in automotive industry," *Int J Adv Manuf Technol*, vol. 39, pp. 851-865, 2008.

- [75] J. Weiler, J. Wood, R. Klassen, R. Berkmortel and G. Wangb, "Variability of skin thickness in an AM60B magnesium alloy die-casting," *Materials Science and Engineering: A*, vol. 419, no. 1-2, pp. 297-305, 2006.
- [76] Li, Y. P., E. Onodera, H. Matsumoto, and A. Chiba. "Correcting the stress-strain curve in hot compression process to high strain level." *Metallurgical and Materials Transactions A* 40, no. 4 (2009): 982-990..
- [77] Park, Gyu Hyeon, Jeong Tae Kim, Hae Jin Park, Young Seok Kim, Hae Joon Jeong, Naesung Lee, Yongho Seo et al. "Development of lightweight MgLiAl alloys with high specific strength." *Journal of Alloys and Compounds* 680 (2016): 116-120..
- [78] Somekawa, Hidetoshi, and Christopher A. Schuh. "Effect of solid solution elements on nanoindentation hardness, rate dependence, and incipient plasticity in fine grained magnesium alloys." *Acta Materialia* 59, no. 20 (2011): 7554-7563..
- [79] Plasticity vs. microstructural characteristics of metals part 1 <http://www.imim.pl/PHD/www.imim>.
- [80] Tang, Yan, Weitao Jia, Xuan Liu, Qichi Le, and Jianzhong Cui. "Precipitation evolution during annealing of Mg-Li alloys." *Materials Science and Engineering: A* 689 (2017): 332-344..
- [81] Zhou, Yucheng, Zhaoyun Chen, Jinghan Ji, and Zhijie Sun. "Dynamic nano precipitation behavior of as-cast Mg-4Li-4Zn-Y alloy during high temperature deformation." *Materials Science and Engineering: A* 707 (2017): 110-117..
- [82] Oliver, Warren C., and Georges M. Pharr. "Measurement of hardness and elastic modulus by instrumented indentation: Advances in understanding and refinements to methodology." *Journal of materials research* 19, no. 1 (2004): 3-20..
- [83] Corby, C., C. H. Cáceres, and P. Lukáč. "Serrated flow in magnesium alloy AZ91." *Materials Science and Engineering: A* 387 (2004): 22-24..
- [84] Zhang, Mengqi, Jinshan Li, Bin Tang, Hongchao Kou, and Jiangkun Fan. "Mechanical characterization and strain-rate sensitivity measurement of Ti-7333 alloy based on nanoindentation and crystal plasticity modeling." *Progress in Natural Science: Material*.
- [85] Churyumov, A. Yu, and V. V. Teleshov. "Quantitative description of the flow-stress dependence of aluminum alloys at the stage of steady flow upon hot deformation on the Zener-Hollomon parameter." *Physics of Metals and Metallography* 118, no. 9 (2017):..
- [86] Jin, Tao, Xiaoyan Niu, Gesheng Xiao, Zhihua Wang, Zhiwei Zhou, Guozheng Yuan, and Xuefeng Shu. "Effects of experimental variables on PMMA nano-indentation measurements." *Polymer Testing* 41 (2015): 1-6..
- [87] Wei, Guobing, Yahya Mahmoodkhani, Xiaodong Peng, Amir Hadadzadeh, Tiancai Xu, Junwei Liu, Weidong Xie, and Mary A. Wells. "Microstructure evolution and simulation study of a duplex Mg-Li

- alloy during Double Change Channel Angular Pressing." Materials &," pp. 266-275, 2016.
- [88] Mechanism of plastic deformation, SRM University, 1996.".
- [89] Kumar, Vinod, Rajiv Shekhar, R. Balasubramaniam, and Kantesh Balani. "Microstructure evolution and texture development in thermomechanically processed Mg–Li–Al based alloys." Materials Science and Engineering: A 547 (2012): 38-50.".
- [90] Magnesium nano-composites: energy-saving materials of future; Meysam Haghshenas, Manoj Gupta; Emerging Materials and Nanotechnology; June 25-26, 2018 Vancouver, British Columbia, Canada.".
- [91] Wei, Guo-bing, Xiao-dong Peng, Bao Zhang, Amir Hadadzadeh, Tian-cai Xu, and Wei-dong Xie. "Influence of I-phase and W-phase on microstructure and mechanical properties of Mg–8Li–3Zn alloy." Transactions of Nonferrous Metals Society of China 25, no. 3 (".
- [92] Singh, P. Bhagat, R. K. Sabat, S. Kumaran, and S. Suwas. "Effect of Aluminum Addition on the Evolution of Microstructure, Crystallographic Texture and Mechanical Properties of Single Phase Hexagonal Close Packed Mg-Li Alloys." Journal of Materials Engi".